

INVESTIGATION OF ACTIVE MICROPARTICLE MOTION AT STRUCTURED  
OIL-AQUEOUS INTERFACES AND MICROCARGO RELEASE VIA  
INTERFACIAL SHEAR

A THESIS SUBMITTED TO  
THE GRADUATE SCHOOL OF NATURAL AND APPLIED SCIENCES  
OF  
MIDDLE EAST TECHNICAL UNIVERSITY

BY

RAMAZAN UMUT DİNÇ

IN PARTIAL FULFILLMENT OF THE REQUIREMENTS  
FOR  
THE DEGREE OF MASTER OF SCIENCE  
IN  
CHEMICAL ENGINEERING

AUGUST 2022



Approval of the thesis:

**INVESTIGATION OF ACTIVE MICROPARTICLE MOTION AT  
STRUCTURED OIL-AQUEOUS INTERFACES AND MICROCARGO  
RELEASE VIA INTERFACIAL SHEAR**

submitted by **RAMAZAN UMUT DINÇ** in partial fulfillment of the requirements for  
the degree of **Master of Science in Chemical Engineering Department, Middle  
East Technical University** by,

Prof. Dr. Halil Kalıpçılar  
Dean, Graduate School of **Natural and Applied Sciences**

\_\_\_\_\_

Prof. Dr. Pınar Çalık  
Head of Department, **Chemical Engineering**

\_\_\_\_\_

Assoc. Prof. Dr. Emre Büküşoğlu  
Supervisor, **Chemical Engineering, METU**

\_\_\_\_\_

**Examining Committee Members:**

Prof. Dr. Nihal Aydoğan  
Chemical Engineering, Hacettepe University

\_\_\_\_\_

Assoc. Prof. Dr. Emre Büküşoğlu  
Chemical Engineering, METU

\_\_\_\_\_

Assoc. Prof. Dr. Pınar Zeynep Çulfaz Emecen  
Chemical Engineering, METU

\_\_\_\_\_

Assoc. Prof. Dr. Erhan Bat  
Chemical Engineering, METU

\_\_\_\_\_

Assoc. Prof. Dr. Simge Çınar Aygün  
Metallurgical and Materials Engineering, METU

\_\_\_\_\_

Date:19.08.2022

**I hereby declare that all information in this document has been obtained and presented in accordance with academic rules and ethical conduct. I also declare that, as required by these rules and conduct, I have fully cited and referenced all material and results that are not original to this work.**

Name, Surname: Ramazan Umut Dinç

Signature :

## ABSTRACT

### INVESTIGATION OF ACTIVE MICROPARTICLE MOTION AT STRUCTURED OIL-AQUEOUS INTERFACES AND MICROCARGO RELEASE VIA INTERFACIAL SHEAR

Dinç, Ramazan Umut

M.S., Department of Chemical Engineering

Supervisor: Assoc. Prof. Dr. Emre Büküşoğlu

August 2022, 125 pages

Microcargo release systems have been reported including liposome vesicles, microcapsules, and micro/nanospheres. Liquid crystal (LC) based systems offer an alternative to these release systems since they are easily fabricated and easy to use. Recently, a new method using an LC-based system for microcargo delivery has been reported that releases microcargo via the applied shear by the motile bacteria near LC/Aqueous interface. In our study, we investigated two potential systems to release microcargo on-demand by the application of interfacial shear applied with active particles. In the first part of the study, we used Janus particles formed by anisotropic coating of  $\text{TiO}_2$  particles with gold, that possess diffusiophoretic motion upon UV light exposure. We characterised Au-coated  $\text{TiO}_2$  Janus particles and their active motion in different Newtonian media. After these characterisations, we found that the active motions of these Janus particles to cease significantly when positioned at the LC/Aqueous interface because of the existing ionic medium. With calculations, we found that the electric double layer thickness at LC/Aqueous interface is comparable with the size of our Janus particles at zero salt concentration. In the second part of the study, we used paramagnetic iron oxide particles to form magnetic microstirrer assemblies at

the LC/Aqueous interface upon magnetic field exposure that applies shear to release microcargo within the water-in-LC emulsion. After characterising the paramagnetic particles, we performed release studies using aqueous emulsion droplets loaded with methylene blue (MB) formed in nematic LC. In this system, the external stimuli that induced the internal flow were the shear forces caused by the rotational motion of the microstirrers at the interface. We analysed the effects of the rotational speed of the magnetic flux director and the interfacial concentration of the paramagnetic particles on the release rate of the microcargo. Our experiments at different rotation speeds revealed that the release rate of MB decreases from 100 ng/min to 25 ng/min as the rotation speed decreases in one hour of microcargo release. In addition, we found an intermediate interfacial concentration of the paramagnetic microparticles for the maximum release rate is around 20000 particles/mm<sup>2</sup>. We also showed the microscopic evidence that the rotation of the microstirrers changed the nematic director of LC locally on the interface.

Keywords: Liquid Crystal, Active Particle, Microcargo Release, Electric Double Layer

## ÖZ

### **YAPILANDIRILMIŞ YAĞ-SU ARAYÜZEYLERİNDE AKTİF MİKROPARÇACIK HAREKETLERİNİN İNCELENMESİ VE ARAYÜZEY KESME YOLUYLA MİKROKARGO SALIMI**

Dinç, Ramazan Umut

Yüksek Lisans, Kimya Mühendisliği Bölümü

Tez Yöneticisi: Doç. Dr. Emre Büküşoğlu

Ağustos 2022 , 125 sayfa

Lipozom vezikülleri, mikrokapsüller ve mikro/nanoküreler dahil olmak üzere mikrokargo salma sistemleri literatürde rapor edilmiştir. Sıvı kristal (LC) bazlı sistemler, kolay üretilebilmeleri ve kullanımları sebebiyle salım sistemlerine bir alternatif sunmaktadır. Son zamanlarda, mikrokargo salımı için LC tabanlı bir sistem kullanan yeni bir yöntemde, LC/Su ara yüzüne yakın, hareketli bakteriler tarafından uygulanan kesme yoluyla mikrokargo salımı yapılabildiği rapor edilmiştir. Bu çalışmada, aktif parçacıklar ile uygulanan ara yüzey kesme uygulaması ile talep üzerine mikrokargo salımı için iki potansiyel sistemi araştırıldı. Çalışmanın ilk bölümünde,  $TiO_2$  partiküllerinin altınla anizotropik kaplanmasıyla oluşturulan ve UV ışığına maruz kaldığında difüzyonoretik hareket gösteren Janus partikülleri kullanıldı. Au kaplı  $TiO_2$  Janus parçacıklarının ve bunların farklı Newtonsal ortamlarında aktif hareketleri tanımlandı. Bu karakterizasyonlardan sonra, bu Janus parçacıklarının aktif hareketlerinin, mevcut iyonik ortam nedeniyle LC/Su ara yüzüne yerleştirildiğinde önemli ölçüde durduğu bulundu. Hesaplamalarla, LC/Su ara yüzeyindeki elektriksel çift tabaka ka-

lınlığının, sıfır tuz konsantrasyonundaki Janus partiküllerimizin boyutuyla karşılaştırılabilir olduğu belirlendi. Çalışmanın ikinci bölümünde, LC içinde su emülsiyonu içindeki mikrokargoyu salmak üzere manyetik alana maruz bırakıldığında LC/Su ara yüzeyinde kesme ile mikrokargo salımı yapabilen manyetik mikro karıştırıcı yapılar oluşturmak için paramanyetik demir oksit parçacıkları kullanıldı. Paramanyetik partiküllerin karakterizasyonu sonrasında, nematik LC içerisinde oluşturulan metilen mavisi (MB) yüklü sulu emülsiyon damlacıklarını kullanarak salım çalışmaları yapıldı. Bu çalışmalarda, iç akışı indükleyen dış uyaranlar, ara yüzeydeki mikro karıştırıcıların dönme hareketinin neden olduğu kesme kuvvetleriydi. Manyetik akı direktörünün dönme hızının ve paramanyetik parçacıkların ara yüzey konsantrasyonunun mikrokargonun salım hızı üzerindeki etkileri analiz edildi. Farklı dönüş hızlarındaki deneyler, bir saatlik mikrokargo salımında dönüş hızı azaldıkça MB'nin salım hızının 100 ng/dk'dan 25 ng/dk'ya düştüğünü ortaya koydu. Ek olarak, maksimum salım hızı için paramanyetik partiküllerin ara yüzey konsantrasyonunun yaklaşık 20000 partikül/mm<sup>2</sup> olduğunu bulundu. Ayrıca, mikro karıştırıcıların rotasyonunun, arayüzde yerel olarak LC'nin nematik direktörünü değiştirdiğini gösteren mikroskobik kanıtları da gösterildi.

Anahtar Kelimeler: Sıvı Kristal, Aktif Parçacık, Mikrokargo Salımı, Elektriksel Çift Tabaka

To My Beloved Family

## ACKNOWLEDGMENTS

First and foremost, I would like to express my greatest gratitude to my advisor Assoc. Prof. Dr. Emre Büküşođlu for their support, guidance and tremendous amount of patience throughout this study. They are one of the few architects of my adventure through research and academia, where I could learn and contribute to the future while nurturing my curiosity.

I would like to thank to Soft and Functional Materials Laboratory Group members; Deniz Işınsu Avşar, Özge Batır, Aslı Karausta, Selin Şengül, Elif Kurt, Ceren Kocaman, Elif Erçelik, Ali Akman, Dr. Pınar Beyazkılıç Ayas and Dr. Selda Sezer for all their support through the darkest nights and the brightest celebrations. It was a privilege and honour to be in such a group that feels like home.

I also would like to show my gratitude to my dearest friends, Güner Dilşad Er, Ahmet Semih Kafkas, Emre Onat Keser and Silay Önder for their unconditional friendship, support and share over 8 years.

No one but my family members deserves my deepest gratitude; Aysel, Münir and Kağan Murat Dinç. Thanks to their unconditional love, support and kindness, I have been always found a way to overcome my deep dark days and find the motivation to pursue my dreams. I could not do this without you.

Lastly, a special thanks to Irem Zeynep Yolcuođlu, for her standing beside me, love, encouragement, patience, and emotional support for the last year and every day.

## TABLE OF CONTENTS

ABSTRACT . . . . .	v
ÖZ . . . . .	vii
ACKNOWLEDGMENTS . . . . .	x
TABLE OF CONTENTS . . . . .	xi
LIST OF TABLES . . . . .	xv
LIST OF FIGURES . . . . .	xvi
LIST OF ABBREVIATIONS . . . . .	xxvi
CHAPTERS	
1 INTRODUCTION . . . . .	1
1.1 Motivation of This Study . . . . .	1
1.2 Liquid Crystals . . . . .	2
1.2.1 Three Key Concepts of Liquid Crystals . . . . .	5
1.3 Objectives of This Study . . . . .	8
2 LITERATURE SURVEY . . . . .	11
2.1 Microcargo delivery methods . . . . .	11
2.1.1 Microparticles, microspheres & microcapsules . . . . .	11
Shape and structure of microcarriers: . . . . .	11
Structure of microspheres and microcapsules: . . . . .	13

2.1.1.1	Microcargo delivery with microcarriers . . . . .	14
	Passive delivery of microcargo: . . . . .	14
	Active/Smart delivery of microcargo: . . . . .	15
2.1.2	Liposome vesicles . . . . .	16
	Design of liposome vesicles: . . . . .	17
	Liposome structure: . . . . .	17
	Selection of lipid and properties: . . . . .	17
	Phase transition temperature: . . . . .	19
2.1.2.1	Liposome vesicle production and microcargo loading methods . . . . .	19
	Conventional methods: . . . . .	20
	Thin film hydration: . . . . .	20
	Reverse phase evaporation: . . . . .	20
	Solvent injection: . . . . .	20
	Detergent removal: . . . . .	21
	Novel methods: . . . . .	21
	Literature example of thermo-responsive liposome vesicle : . . .	23
	Literature example of light-responsive liposome vesicle: . . . .	24
	Literature example of pH-responsive liposome vesicle: . . . . .	25
	Literature example of magneto-responsive liposome vesicle : . .	26
2.1.3	Active microparticles . . . . .	28
	Literature example of microcargo release with active particle using difussiophoresis: . . . . .	28

	Literature example of microcargo release with active particle using electrophoresis: . . . . .	29
	Literature example of microcargo release with active particle using ultrasonic waves: . . . . .	30
	Literature example of microcargo release with active particle magnetophoresis: . . . . .	32
2.2	Microcargo release with liquid crystals . . . . .	33
2.2.1	Aqueous-Liquid crystal interfaces . . . . .	33
2.2.2	Colloidal interactions in liquid crystals . . . . .	35
2.2.3	Interfacial behaviour of colloids and molecular adsorbates on liquid crystals . . . . .	38
	Literature example of microcargo release from liquid crystal emulsions via mechanical shear : . . . . .	39
	Literature example of microcargo release from liquid crystal emulsions via polyelectrolytes : . . . . .	41
3	MATERIALS & METHODS . . . . .	43
3.1	Materials . . . . .	43
3.2	Synthesis of TiO <sub>2</sub> microparticle . . . . .	44
3.3	Synthesis paramagnetic iron oxide microparticle . . . . .	45
3.4	Size & surface characterisation of microparticles via SEM imaging . . . . .	45
3.5	Monolayer coverage of TiO <sub>2</sub> microparticles on glass substrate for noble metal loading . . . . .	46
3.6	Noble metal loading on TiO <sub>2</sub> microparticle hemisphere, Janus particle functionalisation . . . . .	46
3.6.1	Au coating of TiO <sub>2</sub> hemispheres via ion sputtering . . . . .	46
3.6.2	Au coating of TiO <sub>2</sub> hemispheres via thermal coating . . . . .	47
3.7	Preparation of sandwich cell for mean square displacement (MSD) analysis . . . . .	47

3.8	DMOAP, PVA, and PI coating of glass sandwich cells . . . . .	48
3.9	Real time microparticle tracking via optical microscopy & mean square displacement (MSD) analysis . . . . .	49
3.10	Preparation of water-in-liquid crystal emulsion for microcargo release experiments . . . . .	49
3.11	Particle tracking at LC/Aqueous interface experimental setup . . . . .	50
3.12	Preparation samples for microcargo release experiments . . . . .	51
3.13	Measurements of UV-Vis absorbance for microcargo release . . . . .	52
4	RESULTS & DISCUSSION . . . . .	53
4.1	Release studies with self-propelled Au@TiO <sub>2</sub> Janus particles . . . . .	53
4.2	Microcargo Release via Interfacial Microstirrers . . . . .	78
5	CONCLUSION . . . . .	89
	REFERENCES . . . . .	91
APPENDICES		
A	NET FORCE ACTING ON MICRODROPLETS IN LC DOMAIN, 1 MM SALT CONCENTRATION . . . . .	103
B	CALCULATIONS FOR THE OUT OF FOCUS BEHAVIOUR OF THE JANUS PARTICLES . . . . .	105
B.1	Kinetic energy calculation for out of focus behavior of Janus particles	105
B.2	Minimum velocity to suspend a 1 $\mu\text{m}$ Janus particle in aqueous media	105
C	ELECTROSTATIC REPULSIVE DISTANCE BETWEEN LC & AQUEOUS MEDIA . . . . .	107
D	REAL-TIME PARTICLE TRACKING WITH FIJI AND INTEGRATED PLUGINS FOR PARTICLE TRAJECTORY . . . . .	109
E	MATLAB CODES FOR MSD ANALYSES . . . . .	117

## LIST OF TABLES

### TABLES

Table 2.1	Main characteristics of the novel methods for liposome production. Reprinted with permission [1]. Copyright International Journal of Pharmaceutics 2021 . . . . .	22
Table 4.1	Surface charge densities of 5CB in various aqueous NaCl solutions .	75
Table 4.2	Calculation of Debye-Hückel parameter, Debye length and EDL of 5CB & AuCr@TiO <sub>2</sub> in various aqueous NaCl solutions . . . . .	78

## LIST OF FIGURES

### FIGURES

- Figure 1.1 a-d) Thermotropic behaviour of LC to release substance within itself, scale bar is 1 cm. e) Schematic illustration of microcargo release from liquid crystal domain via shear stress by E.Coli bacteria. f-h) Real time images of the system, scale bar 10  $\mu\text{m}$ . Reprinted with permission, [2].Copyright 2018 Nature . . . . . 2
- Figure 1.2 a) Three phases of thermotropic liquid crystals, b) A rod-like shaped liquid crystal mesogen: 5CB. c) An example of chiral dopant (S-811) that forms cholesteric LC phase when added to a nematic LC. d) Schematic of cholesteric LC phase. e) Double-twist cylinders of cholesteric LCs that form at high temperatures and concentrations of chiral dopant. f) The cylinders in g, self-assemble into cubic lattices characteristic of blue-phase LCs. Reprinted with permission, [3].Copyright 2016 Annual Reviews . . . . . 4
- Figure 1.3 Three Key Concepts of Thermotropic Liquid Crystals. a) The surface director of the liquid crystal (LC) and the easy axis. b) The three basic modes of deformation in LC; splay, twist, bend respectively with Franks-Oseen free energy density equation. c) Three types of topological defects resulting from the competition between surface anchoring and elasticity of LC; from left to right, a point defect with radially converging director field, cross-sections of line defects, i.e. disclinations. The line defects were oriented orthogonally to the figure. Reprinted with permission, [3].Copyright 2016 Annual Reviews . . . . . 6

Figure 1.4	a) Off demand representation of the release system, the elastic force is acting in favour of keeping the microcargo in LC domain. b) On demand, the net force is acting in favour of releasing the microcargo in LC domain via generated mechanical shear by the active microparticles at the interface. . . . .	7
Figure 2.1	Illustrations of different microparticle/microcapsule structures. a) Single core-shell, b) Multiwall-single core, c) Multiple core, d) Matrix, e) Coated polynuclear core, f) Coated matrix particle, g) Patch microparticle, h) Dual compartment microcapsule, i) Colloidosome, j) Giant liposome, k) Irregular-shaped microparticle, l) Torus-shaped microparticle, m) Bullet-shaped microparticle, n) Microtablet, o) Cube-shaped microparticle. Reprinted with permission [4]. Copyright Scientia Pharmaceutica 2019 . . . . .	12
Figure 2.2	a) Microspheres of calcium alginate with homogeneous concent. b) Microcapsule made of Water/Oil/Water emulsion in core with calcium alginate shell. c) Janus particle form of calcium alginate derived microcarrier. Reprinted with permission [4]. Copyright Scientia Pharmaceutica 2019 . . . . .	13
Figure 2.3	a) Passive release phenomena of microcarriers. b) Passive release phenomena when there is a polymer shell. Reprinted with permission [4]. Copyright Scientia Pharmaceutica 2019 . . . . .	15
Figure 2.4	Types of stimuli for active/smart microcargo delivery systems. Reprinted with permission [4]. Copyright Scientia Pharmaceutica 2019 . . . . .	16
Figure 2.5	Schematic representation of a liposome vesicle and possible microcargo carrying options. Reprinted with permission [1]. Copyright International Journal of Pharmaceutics 2021 . . . . .	17

Figure 2.6	Liposome vesicle types. From left to right; small unilamellar vesicle (SUV), large unilamellar vesicle (LUV), multilamellar vesicle (MLV), multivesicular Vesicle (MMV). Reprinted with permission [1]. Copyright International Journal of Pharmaceutics 2021. . . . .	18
Figure 2.7	The schematic representation of thermoresponsive liposome vesicle. Reprinted with permission [5]. Copyright International Journal of Pharmaceutics 2021 . . . . .	24
Figure 2.8	The schematic representation of mechanism of lightresponsive liposome vesicle. Reprinted with permission [6]. Copyright Biochimica et Biophysica Acta 2011 . . . . .	25
Figure 2.9	Direct injection of short peptides into mice for CTL activation, left. Use of pH-responsive hyperbranch polymer modified liposome vesicle for CTL activation. Reprinted with permission [7]. Copyright molecules 2016 . . . . .	26
Figure 2.10	Schematic representation of alternating magnetic field actuated magneto-responsive liposome vesicle. Reprinted with permission [8]. Copyright Journal of Colloid and Interface Science 2019 . . . . .	27
Figure 2.11	a) Schematic representation of layer-by-layer production process. b) The schematic of the working principle of the active microparticle. c) Real micrographs of the particle in pH = 1.3 acidic media. d) Layers of the microparticle. e-f) SEM image and EDX analysis of the particle respectively; pink is for Mg and green is for TiO <sub>2</sub> . h-k) Optical and fluorescence images of dye loaded active microparticle. i- is for PLGA layer, j- is for chitosan layer, and k- is for both layers respectively. Reprinted with permission [9]. Copyright Nature Communications 2017 . . . . .	29

Figure 2.12	a) Schematic representation of the designed system working under applied electric field. b) Schematic representation of the nanowire assembly on top of magnetic anchor. c) Micrographs of rotating nanowire at different time intervals, scale bar is 10 $\mu\text{m}$ . d) Release rate of Nile blue with respect to rotating speed of nanowires. Reprinted with permission [10]. Copyright Nature Communications 2014 . . . . .	30
Figure 2.13	a) Red blood cell based magnetic nanoparticle loaded microparticle. b) Red Blood Cell based magnetic nanoparticle, doxorubicin and quantum dots loaded microparticle under ultrasonic wave actuation with applied magnetic field. Scale bars are 20 $\mu\text{m}$ for both image. c) The velocities of microparticles under different transducer voltages. d) The viability study of Human Umbilical Vein Endothelial Cells at the vicinity of the microparticles and free quantum dots, doxorubicin and the mixture of two. Reprinted with permission [11]. Copyright The Royal Society of Chemistry 2015 . . . . .	31
Figure 2.14	a) The schematic representation of working principle of magnetically driven mesoporous silica micromotors carrying 6-carboxyfluorescein as drug. b) The real-time fluorescence spectrum collected in the 6-carboxyfluorescein releasing process. c) Plot of fluorescence at 518 nm against the exposure time in different frequency magnetic fields. Reprinted with permission [12]. Copyright ACS Applied Materials and Interfaces 2015 . . . . .	32
Figure 2.15	Cross-polarized microscopy micrographs of aqueous-liquid crystal interface at different DTAB bulk concentrations for 5-,20-, & 40- $\mu\text{m}$ liquid crystal film respectively. Reprinted with permission, [13]. Copyright 2009 Langmuir . . . . .	34
Figure 2.16	a) Colloidal particle in nematic LC phase with $R \leq K/W_a$ . b-c) Colloidal particle in nematic LC phase with Saturn Ring and hyperbolic hedgehog respectively, when $R \geq K/W_a$ . Reprinted with permission, [14].Copyright 2014 Soft Matter . . . . .	36

Figure 2.17 a) Tangential surface anchoring of LC around spherical particle. b) Homeotropic surface anchoring of LC around spherical particle with hyperbolic hedgehog defect above. c) Special case of homeotropic anchoring, a particle with homeotropic anchoring with Saturn defect loop around it. a- Reprinted with permission, [3].Copyright 2016 Annual Reviews. b-,c- Reprinted with permission, [15].Copyright 2006 Science 37

Figure 2.18 a) Colloidal particle with hyperbolic hedgehog defect. b) Chain formations of colloids along rubbing direction due to hyperbolic hedgehog defects. c) Same colloidal particle in part a, with Saturn ring disclination around equator. d) Kinked chain formations perpendicular to rubbing direction due to Saturn ring disclinations. Reprinted with permission, [15].Copyright 2006 Science . . . . . 38

Figure 2.19 a,b) Silica microparticle sedimented on LC/Aqueous interface with homeotropic anchoring near a topological defect. The interface has planar anchoring. c) Self-assembled dendritic structures on the LC/Aqueous interface formed by attractive interaction between silica microparticles. d,e) Topological defect relocated below silica microparticle. f) Homeotropic surface anchoring at LC/Aqueous interface due to presence of SDS. g) Microparticle patterns as a function of SDS concentration at the LC/Aqueous interface. Reprinted with permission, [16].Copyright 2010 PNAS . . . . . 39

Figure 2.20 a-d) Cross-polarized optical response of LC films in 40  $\mu\text{m}$  TEM grid with chemically treated substrate and the overlying aqueous phase. Scale bar is 200  $\mu\text{m}$  a,b) Initially homeotropic anchoring at the LC/Aqueous interface, before and after applied interfacial stress. c,d) Initially planar anchoring at LC/Aqueous interface, before and after applied interfacial stress. e,f) Calculated  $\mathbf{F}_{EDL}$  (red lines) and  $\mathbf{F}_E$  (blue lines) and  $\mathbf{F}_{Net}$  (black lines) for an aqueous microdroplet ( $R = 1.5 \mu\text{m}$ ). Planar and homeotropic orientations were represented with solid and dashed lines respectively. g,h) Photographs of the ejection of the microdroplets from water-in-LC emulsion, before and after stirring the overlying the aqueous phase with magnetic bar. Scale bar is 1 cm. Reprinted with permission, [2].Copyright 2018 Nature . . . . . 40

Figure 2.21 a) Aqueous microcargo droplet entrapped in liquid crystal domain. b) The positions of aqueous microcargo droplets. c) Release of aqueous microdroplets from LC media upon adsorption of surfactant PDDA. Reprinted with permission, [17].Copyright 2022 Langmuir . . . 41

Figure 3.1 Molecules of E7 liquid crystal mixture. . . . . 44

Figure 3.2 Sandwich glass cell preparation steps. a) Placing the cover glass onto spacers. b) Fixing the sandwich cell with paper clips and dropping epoxy to the corners of the cell. c) Removing of the paper clips after epoxy curing. d) Filling the sandwich cell with fluid and sealing the cell edges with epoxy. . . . . 48

Figure 3.3 Particle tracking at LC/Aqueous interface sample preparation. a) LC filling of TEM grid. b) Complete filling of TEM grid and PDMS mould placing . . . . . 51

Figure 3.4	Sample preparation steps for microcargo release through interfacial shear experiments. a) PDMS well is at the bottom of UV-Vis cuvette and the cuvette is filled with aqueous media. b) Water-in-LC emulsion is introduced to the PDMS well via micropipette. c) Force sedimentation of paramagnetic particles via neodymium magnet, magnet is positioned below the sample having the poles parallel to the interface. Dark Red curves indicate the magnetic flux. d) Force sedimentation after a time interval. e) The cleaning of the aqueous media from salt and/or released microcargo in part b via cross-flow micropumping. f) The sealed sample ready for microcargo release. . . . .	52
Figure 4.1	Sketch of liquid crystal based microcargo release method replacing motile bacteria with micromotor (active microparticle) . . . . .	53
Figure 4.2	Schematic of three forces acting on the aqueous droplet near the LC/Aqueous interface. . . . .	54
Figure 4.3	Net force acting on different sizes of microdroplets at various distances. NaCl salt concentration is set to 0.01 mM for calculation purposes. R represents the radius of water droplet carrying microcargo while h represent the distance to the interface. . . . .	56
Figure 4.4	XRD Spectrum of TiO <sub>2</sub> Microparticles . . . . .	57
Figure 4.5	TiO <sub>2</sub> core particle characterisation. a) SEM images of anatase TiO <sub>2</sub> , 5 μm scale bar. b) SEM image processing result for average diameter of TiO <sub>2</sub> particles. c) histogram for TiO <sub>2</sub> particle diameter. . . . .	58
Figure 4.6	AuPd@TiO <sub>2</sub> Janus particles – a) AuPd@TiO <sub>2</sub> Particle Cluster b) Single AuPd@TiO <sub>2</sub> Particle - SEM image with backscatter mode (right) respectively. c) EDX analysis of a single AuCr@TiO <sub>2</sub> Janus particle. Red is for Ti and light brown is for Au respectively. d-e) Single AuCr@TiO <sub>2</sub> Janus Particle, Left – SEM image, Right – Backscatter mode. Scale bars are 1 μm for particles and 200 nm for coloured EDX analyses. . . . .	59

Figure 4.7	a) Brownian Motion Trajectory of a SiO <sub>2</sub> Particle. 2 μm scale bar. b) The mean square displacement (MSD) of the same particle over time. c) Viscosity measurements of different Newtonian fluids with respect to their true viscosities. d) Mean square displacement ratios of perpendicular dimensions indicating the isotropic motion. . . . .	62
Figure 4.8	a) Particle trajectory over the same time interval, Brownian and active motion of the same AuCr@TiO <sub>2</sub> Janus particle, scale bar is 10 μm. b) The MSD vs Δt analysis of the Brownian and active motion of the same particle. . . . .	63
Figure 4.9	Velocities of AuCr@TiO <sub>2</sub> Janus particles under different fuel concentrations. . . . .	64
Figure 4.10	a-d) Microscopy images of a AuCr@TiO <sub>2</sub> Janus Particle having 3D motion. b,c) Exiting from and re-entering to focus plane respectively. e-f) Out of focus motion sketch of the same micrographs. Red dashed lines represent the focus plane thickness of the microscopy. . . .	65
Figure 4.11	Active velocities of AuCr@TiO <sub>2</sub> JPs at different NaCl concentrations . . . . .	67
Figure 4.12	a) Apparent viscosity histogram around AuCr@TiO <sub>2</sub> JPs above LC/Aqueous interface in x-direction. b) Apparent viscosity histogram around AuCr@TiO <sub>2</sub> JPs above LC/Aqueous interface in y-direction . . .	68
Figure 4.13	Zeta potential measurements for 5CB Liquid Crystal and AuCr@TiO <sub>2</sub> JPs in various NaCl concentrations . . . . .	69
Figure 4.14	a) Schematic representation of designed system for the experiment with a passive motion trajectory of a AuCr@TiO <sub>2</sub> Janus Particle at LC/Aqueous interface, 4 μm scale bar. b) MSD analysis of the same particle in part a; indicating anisotropic interaction of the particle at the interface. . . . .	70

Figure 4.15	Apparent viscosity histograms around AuCr@TiO <sub>2</sub> JPs at LC/Aqueous interface in 300 mM NaCl aqueous solution. a) Along x-direction b) Along y-direction . . . . .	71
Figure 4.16	MSD data of the AuCr@TiO <sub>2</sub> Janus particles under UV illumination. a) Passive particle. b) y-directed. c) x- and y-directed. d) x-directed. The scale bars are 5 μm for each trajectory image. Nematic director of the LC is directed along x-direction as shown with two headed red arrow. . . . .	73
Figure 4.17	Active & passive motions of the same microparticles under a) Visible & b) UV light respectively. XD: x-directed, XD & YD : No specific direction, YD: y-directed, P: Passive. . . . .	74
Figure 4.18	COMSOL 1D simulation results for electric potential between 5CB & Aqueous media . . . . .	77
Figure 4.19	Sketch of liquid crystal based microcargo release method replacing motile bacteria with paramagnetic microparticle based microstirrers. . . . .	79
Figure 4.20	a) Average particle shape & surface morphology of iron oxide particles. b) Big particles merged each other. Scale bars are 2 μm. . . . .	80
Figure 4.21	a-b) Bright field micrographs of interfacial microstirrers under applied magnetic field. c) Polarized micrograph of the same region when the interfacial microstirrers were idle. d) Polarized micrograph of the same region in part c with orientation change of magnetic field resulting in local nematic director change in the sample, appeared as bright regions. e-f) Same configurations in part c and d respectively with additional retarder lens positioned 45° with respect to the polarized filters. Red arrow shows the applied magnetic flux direction. The scale bars are 50 μm for all parts. . . . .	81
Figure 4.22	VSM analysis of superparamagnetic iron oxide microparticles. The curves show no hysteresis attests to no lag of the magnetic excitation. . . . .	82

Figure 4.23	Representative sketch of working mechanism of microcargo release method based on liquid crystal and paramagnetic microstirrers . . .	83
Figure 4.24	MB release via interfacial microstirrers on LC/Aqueous interface at different RPMs. . . . .	84
Figure 4.25	Magnetic particles at 250 RPM on the olive oil/Aqueous interface forming interfacial microstirrers at t=0, t= 9 and t= 18 min. a,b,c) 10,000 Particle/mm <sup>2</sup> . d,e,f) 40,000 Particle/mm <sup>2</sup> . The scale bars are 1 mm for each image. . . . .	86
Figure 4.26	MB release via paramagnetic microstirrers on LC/Aqueous interface at different area concentrations. . . . .	87
Figure A.1	Net force acting on different sizes of microdroplets at various distances. NaCl salt concentration is set to 1 mM. R represents the radius of water droplet carrying microcargo while h represent the distance to the interface. . . . .	103
Figure C.1	Equilibrium distance between 5CB flat surface & AuCr@TiO <sub>2</sub> JPs as a function of NaCl concentration . . . . .	107
Figure D.1	FiJi program, scale settings and signal corrections . . . . .	110
Figure D.2	FiJi TrackMate plugin . . . . .	111
Figure D.3	TrackMate spot finding . . . . .	112
Figure D.4	Initial thresholding and spot filtering. . . . .	112
Figure D.5	TrackMate trajectory builder . . . . .	113
Figure D.6	TrackMate trajectory filtering and data trimming . . . . .	114
Figure D.7	TrackMate trajectory spot data save . . . . .	115

## LIST OF ABBREVIATIONS

2D	2 Dimensional
3D	3 Dimensional
5CB	4-cyano-4'-pentylbiphenyl, a type of liquid crystal
7CB	4-cyano-4'-heptyl-biphenyl, a type of liquid crystal
8OCB	4-cyano-4'-oxyoctyl-biphenyl, a type of liquid crystal
5CT	4-cyano-4''-pentyl-p-terphenyl, a type of liquid crystal
ASES	Aerosol Solvent Extraction Systems
CTAB	Hexadecyltrimethylammonium Bromide / Cetrimonium bromide
DTAB	Dodecyltrimethylammonium Bromide
DMF	Dimethylformamide
E. Coli	<i>Escherichia coli</i>
EDL	Electric Double Layer
E7	Mixture of 5CB, 7CB, 8OCB and 5CT
GAS	Gas Anti-Solvent
GUV	Giant Unilamellar Vesicle
JP	Janus Particle
LC	Liquid Crystal
LUV	Large Unilamellar Vesicle
MSD	Mean Squared Displacement
MB	Methylene Blue
mM	milli Molar
MLV	Multilamellar Vesicle
MMV	Multivesiclular Vesicle

NR	Natural Red
PIM	Paramagnetic Ironoxide Microparticle
PC	Phosphatidylcholine
PE	Phosphatidylethanolamine
PEG	Polyethylene Glycol
PDDA	Poly(diallyldimethylammonium chloride)
PI	Polyimide
POM	Polarized Optical Microscope
RESS	Rapid Expansion of Supercritical Solution
RPM	Revolutions per Minute
SEM	Scanning Electron Microscopy
SDS	Sodium Dodecyl Sulfate
SAS	Supercritical Anti-Solvent
SCRPE	Supercritical Reverse-Phase Evaporation
SCD	Surface Charge Density
SUV	Small Unilamellar Vesicle
ULV	Unilamellar Vesicle
UP	Ultra Pure Water
VSM	Vibrating Sample Magnetometer



## CHAPTER 1

### INTRODUCTION

#### 1.1 Motivation of This Study

In recent years, new methods have been introduced to the literature to release microcargo in a more controlled way by using microcapsules, microspheres and microparticles [4]. Among these studies, the oil-based assemblies had gotten attention due to their high load capacity and biocompatibility. [1] However, some of the production methods of these systems require special equipment for fabrication and are too sophisticated and expensive to be employed in useful scales. For example, microsphere production for drug delivery systems generally requires nozzle production, which makes mass production expensive due to equipment costs. Besides that, the oil-based microcargo delivery systems generally lack thermal stability and have leakage of microcargo issues. Therefore, an alternative method that is simple to prepare, easily attainable and affordable for commercial use should be introduced to the literature. For this purpose, using structured oil/water emulsions to create microcargo vessels is a great choice. Kim et al. reported that using nematic liquid crystals, a type of structured oil, can be an alternative for microcargo-carrying vessels. [2] Moreover, as illustrated in **Figure 1.1-a,-b,-c,-d** they showed that with the help of the thermal energy of the thumb, the liquid crystal could eject the aqueous droplets within itself. In addition to this mechanism, it is possible to release microcargo within the liquid crystal domain via mechanical shear stress generated by swimming *Escherichia coli* (E. Coli) bacteria near the aqueous interface, shown in **Figure 1.1-e**. When there is no bacteria or bacterial movement near the interface, the liquid crystal domain holds the microcargo, **Figure 1.1-f,-h**. However, when the motile bacteria move near the interface, the bacteria movement enables the ejection of the microcargo, eventually

ceasing the bacterial movement.

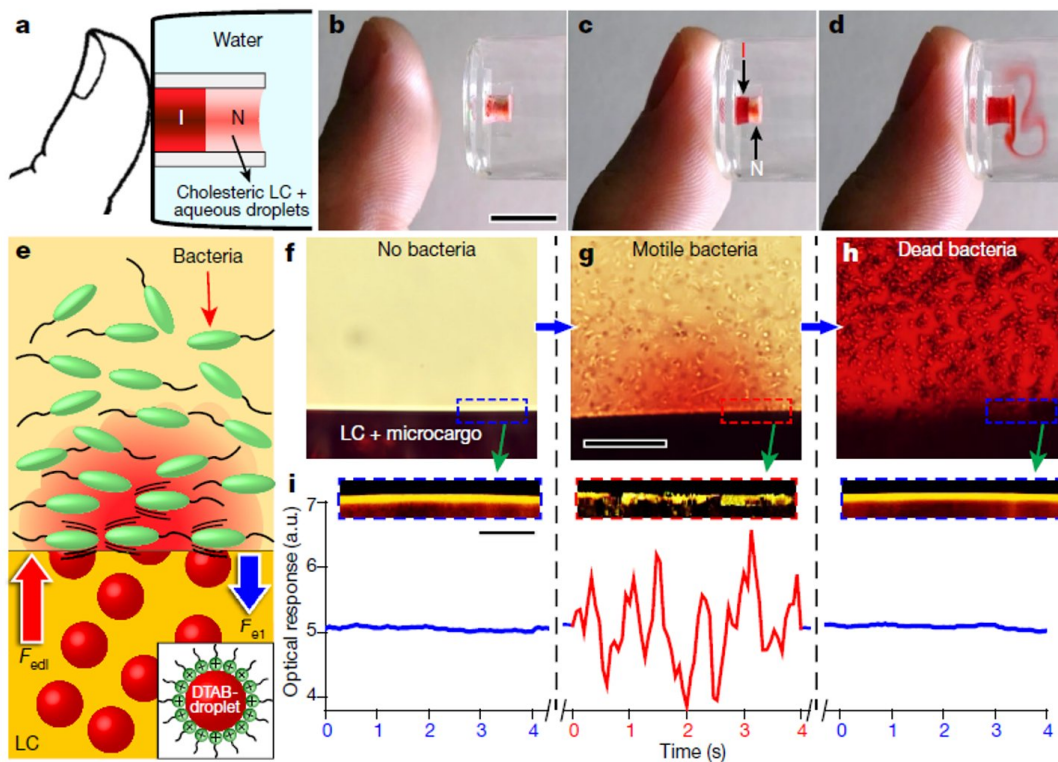


Figure 1.1: a-d) Thermotropic behaviour of LC to release substance within itself, scale bar is 1 cm. e) Schematic illustration of microcargo release from liquid crystal domain via shear stress by E.Coli bacteria. f-h) Real time images of the system, scale bar 10  $\mu\text{m}$ . Reprinted with permission, [2]. Copyright 2018 Nature

## 1.2 Liquid Crystals

Liquid crystals (LCs) are condensed fluid phases that are thermodynamically stable at a temperature range between crystalline solid and isotropic liquid phases. As the temperature decreases for LCs, the long-range order increases as crystalline solids, renouncing mobility. On the other hand, as the temperature increases, the mobility of the LCs increases; however, the long-range order of the matter vanishes, **Figure 1.2-a**. There are two main types of liquid crystals, thermotropic and lyotropic, respectively. Briefly, the system's temperature can determine the phase behaviour alone for thermotropic liquid crystals; on the other hand, lyotropic liquid crystal systems require the addition of a solvent to form a liquid crystal phase since these systems consist of more

than one component. Liquid crystals consist of molecules, referred to as mesogens, with many unique properties derived from their long-range ordering [18]. Between crystalline solid and isotropic liquid phase, the nematic phase exists. The nematic phase is the LC phase in which the mesogens are aligned in the same direction but do not exhibit long-range positional order on average. Thermotropic liquid crystals exhibit an average orientation, which is often stated as nematic director, in the nematic LC phase that is preserved over distances that are several orders of magnitude greater than the mesogen dimensions [3]. One of the rod-like liquid crystal mesogen that exhibit nematic phase at room temperature, 5CB (4 -Pentyl-4-biphenylcarbonitrile), is shown in **Figure 1.2-b**. Besides 5CB, one of the simplest and relatively long-studied LCs, there are many exotic LC phases that have been discovered, classified as twist-bend or heliconical nematic phases [19]. Even though the nematic and twist-bend LCs phases arise from the properties and organisations of a single molecule, having mixtures of molecules of different types of mesogens or mixtures of mesogens and non-mesogen molecules gives a variety of intriguing LC phases. One famous example is the addition of a chiral molecule **Figure 1.2-c** to a nematic LC phase. At sufficiently high concentrations, the chiral dopant in the mixture gives the nematic LC phase a twist that is orthogonal to the nematic director near nematic-isotropic transition temperature, **Figure 1.2-d**, which is referred to as cholesteric LC. Due to this twisted structure, self-assembled periodic 3D cylindrical structures could be formed by these cholesteric LC phases, **Figure 1.2-e,f**, which is often referred to as blue phase for historical reasons [20].

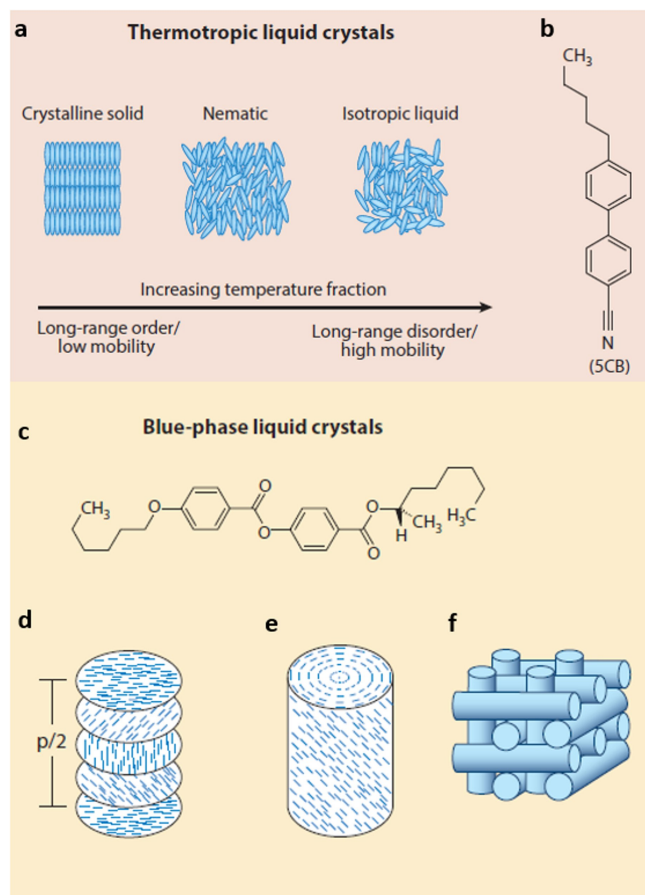


Figure 1.2: a) Three phases of thermotropic liquid crystals, b) A rod-like shaped liquid crystal mesogen: 5CB. c) An example of chiral dopant (S-811) that forms cholesteric LC phase when added to a nematic LC. d) Schematic of cholesteric LC phase. e) Double-twist cylinders of cholesteric LCs that form at high temperatures and concentrations of chiral dopant. f) The cylinders in g, self-assemble into cubic lattices characteristic of blue-phase LCs. Reprinted with permission, [3]. Copyright 2016 Annual Reviews

The examples described above show that there is wide chemical diversity of LC. Nevertheless, having complete differences in chemistry, LC phases exhibit unanimous characteristics due to their ability to reorganise and communicate information across mesogens with long-range order and mobility. Due to these features, they are excellent candidates for active material-based systems.

### 1.2.1 Three Key Concepts of Liquid Crystals

In order to understand systems containing liquid crystals, three key concepts of liquid crystals should be mentioned. These concepts underlie the colloidal and interfacial phenomena between LCs. These concepts are the surface anchoring of LCs, the elasticity of LCs and lastly, the formation of topological defects in LCs.

The surface anchoring term refers to the surface-induced ordering of LCs due to the intermolecular interactions between mesogens and contacting interfaces. When there is no external field, the lowest free energy state orientation of the nematic director is called the easy axis, shown in **Figure 1.3-a** [21]. Any disturbance to the orientation of LC, such as applying external field, chemical gradient etc., that results in the deviation from the easy axis (shown as "Surface Director" in **Figure 1.3-a**) leads to an increase in the free energy of interface described by the following equation [22]

$$\mathbf{F}_s = \mathbf{F}_0 + \frac{1}{2} \mathbf{W}_a \sin^2 (\theta_s - \theta_e) \quad (1.1)$$

Where  $\mathbf{F}_s$  is the interfacial free energy,  $\mathbf{F}_0$  is the free energy of the interface on the easy axis,  $\mathbf{W}_a$  is the anchoring energy, and  $\theta_s$  and  $\theta_e$  are the angles defining the orientations of the surface director and the easy axis, respectively.

The long-range orientational ordering of LC mesogens arises due to the elasticity of LCs. There are three fundamental modes of strain in LCs, dubbed as twist, bend and splay, respectively, shown in **Figure 1.3-b**. However, all LCs do not need to possess all types of these strains. One of the simplest descriptions of these elastic strains of LCs is the so-called Frank-Oseen equation for the free energy density [23]

$$\mathbf{F}_e = \frac{1}{2} \mathbf{K}_1 (\nabla \cdot \underline{n})^2 + \frac{1}{2} \mathbf{K}_2 (\underline{n} \cdot \nabla \times \underline{n})^2 + \frac{1}{2} \mathbf{K}_3 \left[ \underline{n} \times (\nabla \times \underline{n}) \right]^2 \quad (1.2)$$

Where  $\mathbf{K}_1$ ,  $\mathbf{K}_2$ , and  $\mathbf{K}_3$  are the splay, twist and bend elastic constants respectively, each having the typical order of  $10^{-11}$ N. [24]

The third fundamental concept of LCs is the topological defects in LC media, shown in **Figure 1.3-c**. The topological defects are caused by the competence between the

surface anchoring and elastic energy in LC when LC is confined in certain geometries. Since LC cannot preserve its surface-induced orientation (due to 3D boundaries) throughout a long continuous strain of the LCs, certain regions of LC are generated in which the strain rate is sufficiently high that the LC locally melts in those regions. These regions could be as small as 5 nm (shown in **Figure 1.3-c**); however, their effects are significant in LC systems compared to their size.

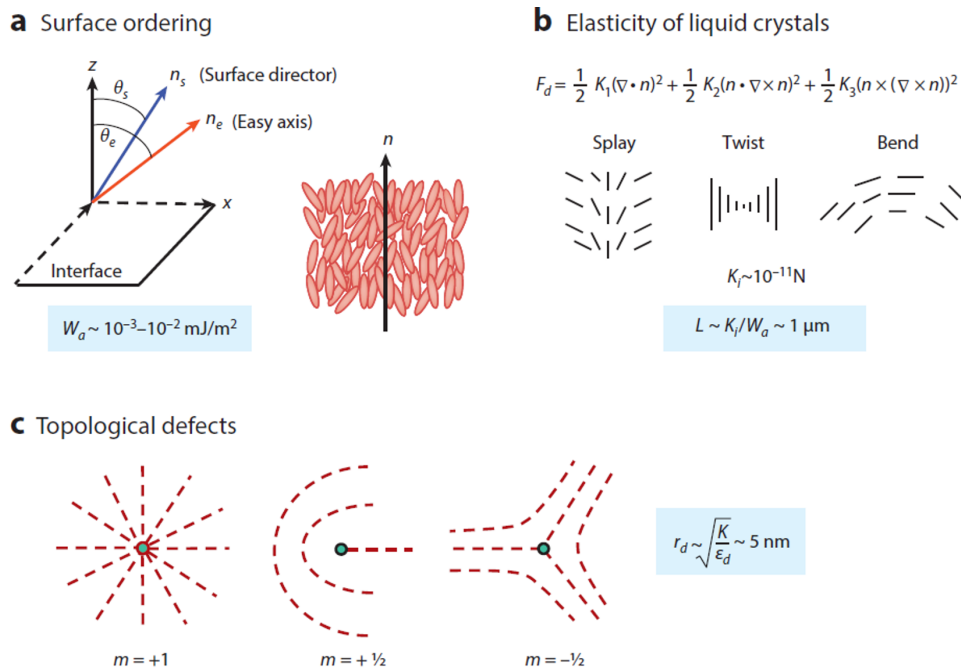


Figure 1.3: Three Key Concepts of Thermotropic Liquid Crystals. a) The surface director of the liquid crystal (LC) and the easy axis. b) The three basic modes of deformation in LC; splay, twist, bend respectively with Franks-Oseen free energy density equation. c) Three types of topological defects resulting from the competition between surface anchoring and elasticity of LC; from left to right, a point defect with radially converging director field, cross-sections of line defects, i.e. disclinations. The line defects were oriented orthogonally to the figure. Reprinted with permission, [3]. Copyright 2016 Annual Reviews

For our designed systems, the surface anchoring of liquid crystals is crucial since it is one of the key concepts that entraps the aqueous microcargo droplets containing CTAB into the liquid crystal domain [22]. Normally, 5CB [13] and E7 [25] LC mesogens tend to maintain planar anchoring with an aqueous environment without addition of surfactant, type of anchoring in which the mesogens are parallel to the water

molecules. However, with the addition of positively charged cetrimonium bromide (CTAB) surfactant, the mesogens tend to have homeotropic anchoring [26], in which the mesogens are perpendicular to the aqueous environment, in order to decrease the free energy of the interface. In addition to the surface anchoring, the ability to contain elastic strains in LCs is a complementary design parameter for our systems. Since the surface anchoring with the microcargo carrying aqueous droplets in the liquid crystals and the surface anchoring with the aqueous domain are different from each other, there is an energy barrier for the microcargo carrying aqueous droplets to overcome in order to be released into the aqueous domain. With this phenomenon, the liquid crystal phase can engulf the microcargo carrying aqueous droplets and not present their release without a demand.

We sought to design a release system that can be controlled by a few parameters and works on demand. Firstly, the systems should not release any cargo without demand as shown in **Figure 1.4-a**. Secondly, for these systems, we planned to synthesize microparticles to replace the bacteria [2] for mechanical shear stress generation at the LC/Aqueous interface, which could be activated upon demand as shown in **Figure 1.4-b**. The microparticles must also have rapid response and be fabricated easily. Therefore, we have selected two active particle candidates to achieve this objective.

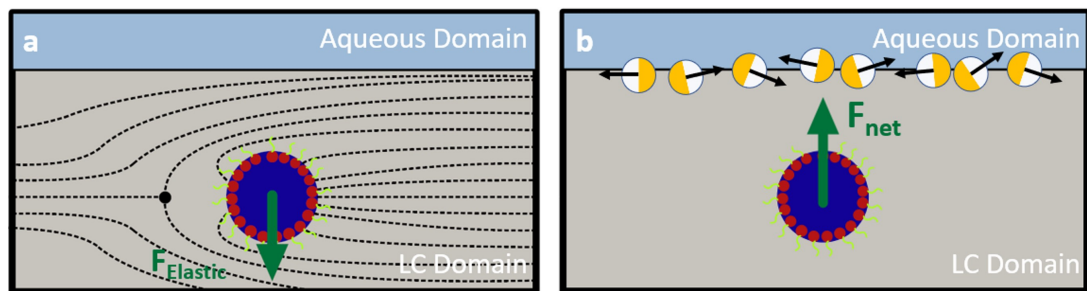


Figure 1.4: a) Off demand representation of the release system, the elastic force is acting in favour of keeping the microcargo in LC domain. b) On demand, the net force is acting in favour of releasing the microcargo in LC domain via generated mechanical shear by the active microparticles at the interface.

The first one, anatase  $TiO_2$ -based Janus particles [27], makes an anisotropic motion upon UV exposure. We designed microcargo release system based on LC, replacing the moving bacteria with these Janus particles. As the anatase  $TiO_2$  Janus particle is

exposed to UV light, it moves anisotropically. This anisotropic movement generates a flow at the LC/Aqueous interface. This flow might enable the microcargo-loaded aqueous droplets to be released to the aqueous domain.

The second one, paramagnetic iron oxide microparticles [28], can be moved on the interface while changing the magnetic flux orientation. Using paramagnetic iron oxide microparticles was a different method for microcargo release than mimicking bacterial movement. These particles were designed to form microstirrers on the interface and generate flow in a different fashion. These microstirrers were intended to be aligned with the magnetic flux director as it changes its orientation. When the paramagnetic microparticles move on the interface, they generate mechanical shear stress. This shear stress enables the microcargo-loaded aqueous droplets to escape to the aqueous domain via the generated internal flow within the LC phase.

### 1.3 Objectives of This Study

In order to design a microcargo release system based on the structured oil-water emulsion and mechanical shear generation via external stimuli, we need to achieve several steps summarized below. These subtitles also summarize the objectives of this thesis.

- **Synthesis and characterisation of active microparticles :** We need to synthesize active microparticles. The microparticles must be fabricated easily and suitable for scale-up for applications. These microparticles' actuation must be rapid and robust without any time lag for on-demand purposes. Furthermore, the particles should maintain significant activation over time.
- **Characterisation of water-in-LC emulsion and LC/Aqueous interface :** In order to understand the phenomena between the LC and contained microcargo carrying aqueous droplets, the characteristics of emulsions should be addressed. Moreover, since active microparticle movement at the interface strongly depends on the surrounding's physical and/or chemical properties, we need to characterise the interface conditions for our designed system.
- **Interfacial position of active microparticles :** In order to actuate the mechan-

ical shear stress, the active microparticles must be localized onto the LC/Aqueous interface, and their distribution should be characterized.

- **Activation characterisation of microparticles at LC/Aqueous interface :** After positioning the particles at the interface, the degree of activation characterisation of these particles must be done to prove that the particles meet the condition for enough mechanical shear generation.
- **Characterisation of the microcargo release :** After all the system parameters are set, the characterisation of the release mechanism has to be done in order to achieve controlled on-demand release criteria.



## CHAPTER 2

### LITERATURE SURVEY

#### 2.1 Microcargo delivery methods

In the past decade, new methods for microcargo delivery systems have been introduced to the literature. Generally, these methods were developed for drug delivery systems. For any microcargo release methods, it was desired to have on-demand release with control. Moreover, for in vivo applications, the developed systems must have high biocompatibility.

##### 2.1.1 Microparticles, microspheres & microcapsules

The use of microparticles, microspheres and microcapsules, referred to as microcarriers, offers a wide study field for microcargo release. Due to their structural and functional diversity, microcarriers have many advantages [29]. Depending on the drug delivery method, they can be in the form of capsules, tablets, sachets, gels, creams, pastes, solutions, suspensions and parenterals [4]. Microsphere formations can carry different types of microcargo, either dissolved or suspended [30]. On the other hand, microcapsules act like a reservoir for the microcargo with a membrane shell surrounding the core [31].

**Shape and structure of microcarriers:** One advantage of these microcarriers is their relatively bigger size compared to nanocarriers. The reason is that these microcarriers have sizes ranging from 1  $\mu\text{m}$  to 1000  $\mu\text{m}$ , which cannot be transported by the lymphatic system just like nanocarriers [32]. Therefore, the effect of microcarri-

ers can be localized. Depending on the application, these microcarriers' construction and structure may change. The shape of the microparticles can be spherical, or they may be in other shapes, **Figure 2.1**. They may deliver cargo in homogeneous matrix, shown in **Figure 2.1-a,-b,-g**, or in heterogeneous way, shown in **Figure 2.1-c,-d,-e,-f,-h**. Some of these microparticle assemblies are classified as Janus particles which have a certain shape and phase anisotropy, **Figure 2.1-h**. While some of them are classified as patchy particles, **Figure 2.1-g,i** which are spherical geometries with different shaped patches on the spherical surface [4]. The spherical shape is generally preferred since the further processing of the shape is easier compared to complex shapes.

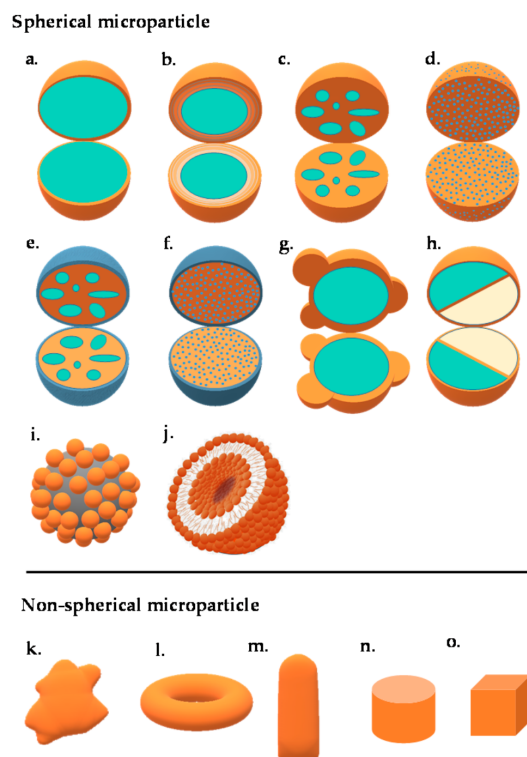


Figure 2.1: Illustrations of different microparticle/microcapsule structures. a) Single core-shell, b) Multiwall-single core, c) Multiple core, d) Matrix, e) Coated polynuclear core, f) Coated matrix particle, g) Patch microparticle, h) Dual compartment microcapsule, i) Colloidosome, j) Giant liposome, k) Irregular-shaped microparticle, l) Torus-shaped microparticle, m) Bullet-shaped microparticle, n) Microtablet, o) Cube-shaped microparticle. Reprinted with permission [4]. Copyright Scientia Pharmaceutica 2019

**Structure of microspheres and microcapsules:** The main difference between microspheres and microcapsules is their way of construction. Microspheres are generally composed of matrix systems that the microcargo is homogeneously dissolved or suspended. On the other side, microcapsules are heterogeneous particles having a membrane shell surrounding the core reservoir. In **Figure 2.2**, microsphere, microcapsule and "Janus Particle" forms of calcium alginate microparticles are shown.

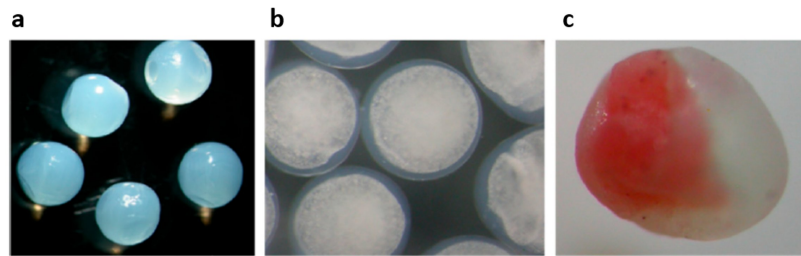


Figure 2.2: a) Microspheres of calcium alginate with homogeneous concent. b) Microcapsule made of Water/Oil/Water emulsion in core with calcium alginate shell. c) Janus particle form of calcium alginate derived microcarrier. Reprinted with permission [4]. Copyright Scientia Pharmaceutica 2019

Many parameters can affect the drug delivery ability of microcarriers. The surface charge of these microcarriers has great significance in terms of aggregation and interaction with their surroundings. Any aggregation may decrease the efficiency of the administration of the microcarrier content. Moreover, the aggregation of the microcarriers may block the normal flow of blood in the body resulting in complications. Besides surface charge, the porosity of the microcarrier can also affect microcargo delivery ability [33].

Recently, the use of anisotropic microspheres and microcapsules got attention due to their special properties. For example, Janus particles, **Figure 2.1-h**, can be synthesised to contain both hydrophilic and hydrophobic matrices at the same time. This structure simultaneously delivers different compounds, allowing a wide range of use in imaging and sensing applications [34]. Use of patchy particles, **Figure 2.1-g,-i**, is another alternative for microcargo delivery. These particles can form clusters allowing them to build supercolloidal architectures that can withstand drying forces or be able to swell several times their original volume reversibly in a swelling agent [35]. Another widely studied microcarrier assembly is liposomes. Liposomes are con-

structed by one or more amphiphilic phospholipid bilayers. Due to their versatility, they have been used as drug carriers in vivo applications. Moreover, since their phospholipid bilayer can mimic the cell membrane, they can interact with cells via several mechanisms such as interaction with the cell surface components, fusion with the membrane, endocytosis via phagocytic cells, or swap by bilayer components. [4] This allows liposome vesicles to be functionalised for a wide range of therapeutic applications.

### **2.1.1.1 Microcargo delivery with microcarriers**

The delivery of microcargo in the microcarriers can be divided into two; passive and active delivery.

**Passive delivery of microcargo:** Various phenomena and mechanisms can co-occur in conventional passive delivery systems. Microcarriers can use dissolution/diffusion, osmotic pressure, or erosion for passive delivery, **Figure 2.3-a**. Depending on the application, even though these mechanisms take place side by side, one or the other provides a greater role during the release [36]. When there is a polymer matrix, the passive delivery of the microcargo can be done through the pores of the polymer network, shown in **Figure 2.3-b**.

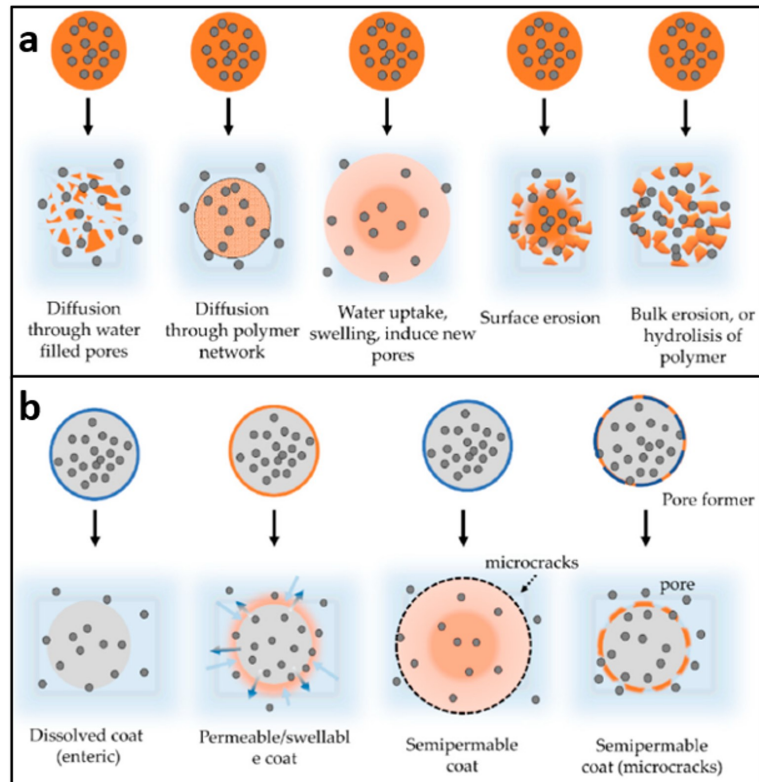


Figure 2.3: a) Passive release phenomena of microcarriers. b) Passive release phenomena when there is a polymer shell. Reprinted with permission [4]. Copyright Scientia Pharmaceutica 2019

**Active/Smart delivery of microcargo:** The active/smart delivery of microcargo is triggered by an external stimulus. Depending on the application, more than one stimulus can be integrated into active microcargo delivery systems for sequenced release. The stimulus may be internal or external and can be classified as physical and chemical, as shown in **Figure 2.4**

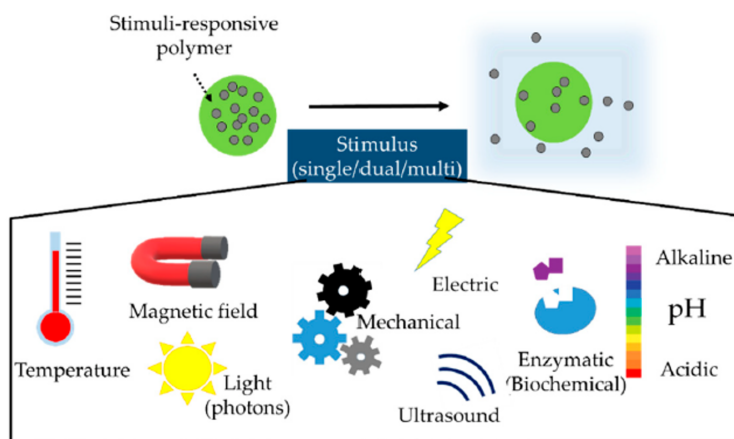


Figure 2.4: Types of stimuli for active/smart microcargo delivery systems. Reprinted with permission [4]. Copyright Scientia Pharmaceutica 2019

Due to their biocompatibility and wide range of options for functionalisation, liposome-based microcargo delivery methods have been studied deeply over the years. Their main advantage is that due to their phospholipid bilayer structure, they can mimic the cell membrane and hence be suitable for in vivo microcargo/drug delivery systems. Moreover, since their lipid bilayers can be functionalised with various ligands, they are great candidates for active/smart microcargo delivery systems.

### 2.1.2 Liposome vesicles

Liposome vesicles were discovered in 1960 by haematologist Dr. Alec D. Bangham et al. [37]. They are defined as the colloidal spherical structures formed by the self-assembled amphiphilic lipid molecules in aqueous solutions. These liposomal membranes can be composed of one or more lipid bilayers, so-called lamellas. These lamellar structures can form vesicles via self-organisation by turning their polar groups around an internal aqueous core and outer aqueous phase [38]. Due to their amphiphilic structure, liposome vesicles can carry hydrophilic microcargo in their aqueous core. They also carry hydrophobic microcargo inside their bilayers, or they can carry amphiphilic microcargo on their bilayers as shown in **Figure 2.5**.

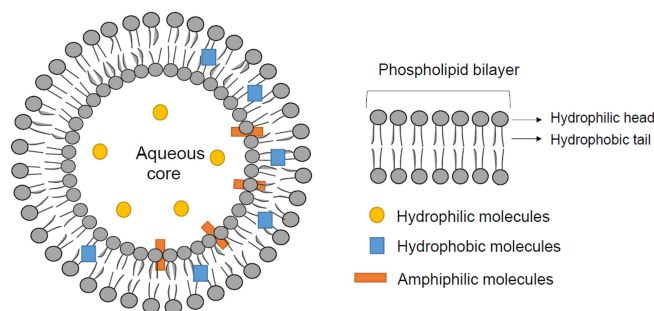


Figure 2.5: Schematic representation of a liposome vesicle and possible microcargo carrying options. Reprinted with permission [1]. Copyright International Journal of Pharmaceutics 2021

**Design of liposome vesicles:** The design of a liposome vesicle for microcargo delivery is a crucial step for the determination of the safety, stability and efficiency of the application [39]. Besides that, the microcargo carrying ability of the liposome vesicles can be affected by the number and rigidity of lipid bilayers, size, surface charge, lipid organisation and chemical surface modification of the liposome vesicles [40].

**Liposome structure:** Liposome vesicles can be classified based on their size and the number of lipid bilayers, **Figure 2.6**. When there is only one bilayer, the liposome vesicles are classified as unilamellar vesicles (ULV). In contrast, when there is more than one bilayer, they are classified as multilamellar vesicles (MLV) and multivesicular (MMV). Unilamellar vesicles can also be subcategorized by their size into three. Small unilamellar vesicles (SUV) are typically around 20-100 nm in size; whereas large unilamellar vesicles (LUV) and giant unilamellar vesicles (GUV) are greater than 100 nm and 1000 nm respectively [41].

**Selection of lipid and properties:** For the construction of liposome vesicles, glycerophospholipids are used. These molecules are amphiphilic lipids composed of a glycerol part bound to a phosphate group and two fatty acid chains that may be saturated or unsaturated [42]. Glycerophospholipids can be either natural or synthetic. In the literature, since they are abundant in plants and animals, the most used natural

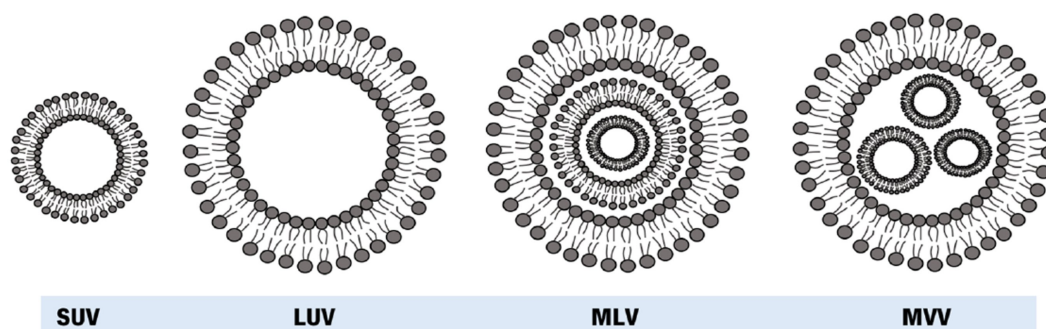


Figure 2.6: Liposome vesicle types. From left to right; small unilamellar vesicle (SUV), large unilamellar vesicle (LUV), multilamellar vesicle (MLV), multivesicular Vesicle (MMV). Reprinted with permission [1]. Copyright International Journal of Pharmaceutics 2021.

phospholipids to produce liposome vesicles are phosphatidylcholine (PC) and phosphatidylethanolamine (PE). [43] Synthetic phospholipids, on the other hand, are also derived from natural phospholipids by changing the head groups, aliphatic chains and alcohols of natural phospholipids.

Due to their amphiphilic structure, glycerophospholipids can form stable bilayers in aqueous media. Polar head groups, and phosphate groups, are attracted to each other by hydrophilic interaction and water molecules are also connected to polar head groups by hydrogen bonding. At the same time, the hydrocarbon chains are attracted to each other by van der Waals forces. Moreover, since hydrocarbon chains are hydrophobic, water molecules force glycerophospholipids to form self-assembled closed bilayers of liposome vesicles [44]. Depending on the charge of the phosphate group, these liposome vesicles could be neutral, positively or negatively charged.

The selection of the parts of the glycerophospholipids can affect the stability of the liposome vesicles formed in the aqueous environment. The longer hydrocarbon chains, low degrees of unsaturation or addition of ether linkages can promote better stability [39]. In recent years, different molecules have been used to increase the stability of liposome vesicles based on glycerophospholipids. The most common molecules are cholesterol, propylene glycol, polyethylene glycol (PEG) and chitosan. The additional molecule can have different prolonged effects on healthy tissue and cells,

even affecting the immune system [45]. Cholesterol can induce dense packing between the hydrophobic tails of the lipid bilayer of liposome vesicles due to their hydrophobic character, promoting better stability by reducing the fluidity and permeability [46]. Propylene glycol can improve liposome vesicles' flexibility for skin delivery drugs [47]. On the other hand, for in vivo applications, the blood circulation half-life is a critical design point. One of the major disadvantages of using conventional liposome vesicles is the clearance of these vesicles from the bloodstream in minutes by the reticuloendothelial system and ending up in the tissues or organs such as the liver and spleen [48]. The use of PEG molecules on the outer surface of liposome vesicles can improve the blood circulation half-life from a few minutes to several hours [49]. Polymers such as chitosan can increase liposome vesicles' stability by providing a protective shell on the surface for microcargo delivery [50].

**Phase transition temperature:** Another design parameter for liposome vesicles is the phase transition temperature of the liposome vesicle. The phase transition temperature refers to the point where the lipid bilayers of liposome vesicles transit from gel state to liquid crystalline state. [51] The transition temperature can be modified by controlling the degree of saturation of the hydrocarbon chains, saturation degree, the ionic interaction of the suspension medium and the characteristic of the polar head group of the glycerophospholipids in the bilayers [52]. The transition temperature decides whether the liposome vesicle is more permeable in a specific site depending on the temperature since, in its gel state, the lipid bilayers tend to be denser while representing low fluidity. In contrast, the liposome vesicle molecules are highly mobile with increased permeability when the temperature is higher than the phase transition point. When the temperature is around phase transition temperature, the permeability of the liposome vesicles highly increases due to the coexistence of gel and liquid crystalline state domains with highly permeable interfacial regions [53].

### **2.1.2.1 Liposome vesicle production and microcargo loading methods**

Since liposome vesicles have been around for almost five decades, there are conventional methods and some new novel methods for the production and microcargo

loading of the liposome vesicles in the literature. The selected/designed production method greatly affects the final product in terms of size, lamellarity, and encapsulation efficiency [54].

**Conventional methods:** Over the years, the most common conventional liposome vesicle production methods have been thin-film hydration, reverse phase evaporation, solvent injection, and detergent removal [55] [56]. Generally, these methods consist of 4 steps; dissolution of lipids in an organic solvent, removal of organic solvent, further purification and isolation of liposome vesicles and lastly, the analysis of the final product.

**Thin film hydration:** Primarily known as the Bangham method, the thin film hydration method was firstly described by Bangham in 1967 [57]. In this method, lipids are generally dissolved in a strong organic solvent such as chloroform. The organic solvent is evaporated to form a lipid at the bottom of the flask. The lipid film is then hydrated using an aqueous solvent, and liposome vesicles are formed by shaking. The final liposome vesicles differ depending on the aqueous solvent conditions and shaking intensity.

**Reverse phase evaporation:** Just as in the thin-film hydration method, the lipids are firstly dissolved in an organic solvent, and then the solvent is evaporated. After the evaporation of the solvent, the resulting film at the bottom of the flask is firstly introduced to another solvent to be re-dissolved, such as diethyl-ether and/or isopropyl ether. After that, an aqueous phase is introduced to form an oil-in-water emulsion [54]. The mixture is then ultrasonicated to form homogeneous inverted liposome vesicles. Lastly, the organic solvents evaporated under reduced pressure, which resulted in a liposome vesicle containing suspension [58].

**Solvent injection:** In this method, the lipids dissolved in an organic solvent are injected into an aqueous solution to form liposome vesicles. Generally, as the organic solvent, ethanol has been selected due to its repeatability, quick production, easy scale-up, and not causing lipid degradation [59].

**Detergent removal:** The detergent removal method is another alternative to produce liposome vesicles. This method makes the phospholipids soluble in aqueous media with detergent at critical micelle concentrations. The detergent in the media is then removed by various methods such as column chromatography and dialysis with an aqueous media forcing the phospholipids to self-assemble into liposome vesicles [54].

**Novel methods:** The conventional liposome vesicle production methods need new approaches mostly due to a lack of scale-up ability for industrial production [54]. Some of these novel methods are improvements of the conventional methods. For example, Wagner et al. have used cross-flow injection [60], and Charcosset et al. have used membrane contractor technology [61] to improve the ethanol injection method. Moreover, ultrasonication of lipid layers after direct hydration is also introduced to the literature to increase the number yield of liposome vesicle production [62]. Since the mentioned methods use an organic solvent, using supercritical fluids in the production of liposome vesicles has also been studied widely to eliminate organic solvent use. Supercritical fluid offers a cheap and environmentally friendly alternative with more possible scale-up production [63]. Karn et al. reported the most used supercritical fluid methods as injection and decompression, rapid expansion of supercritical solution (RESS), gas antisolvent (GAS), supercritical antisolvent (SAS), aerosol solvent extraction systems (ASES), and supercritical reverse-phase evaporation (SCRPE) [56]. Recently, other methods for liposome vesicle production were also introduced to the literature, such as dual asymmetric centrifugation and the use of microfluidic devices [55], [64]. Guimaraes et al. outlined these novel methods' major positive and negative sides in the table below [1].

Table 2.1: Main characteristics of the novel methods for liposome production. Reprinted with permission [1]. Copyright International Journal of Pharmaceutics 2021

Method	Main Characteristics
Cross-flow injection (Wagner)	(+) Simple, scalable, continuous and sterile process. (-) Residual organic solvents can creates stability
Membrane contractor	(+) Simple, rapid, scalable and continuous process; homogenous liposomes with higher encapsulation efficiency for lipophilic drugs. (-) Less studied for hydrophilic drugs; high-cost material.
Cross-flow filtration	(+) Rapid, scalable, sterile process; homogeneous liposomes with high stability; facility to removal of detergent. (-) Understudy method.
Injection and decompression	(+) Sterile process; homogeneous liposomes by changing the nozzle diameter; narrow liposome size distribution; small organic solvent consumption. (-) Complex equipment with low yield; needs of high temperature and pressure; more adequate for hydrophobic drugs; nozzle can stay clogged.
RESS	(+) Simple fast and solvent-free process; liposomes with controllable size. (-) Low yield and encapsulation efficiency.
GAS	(+) Suitable for a wide range of drugs; liposomes with variable size; and moderate stability; solvent-free and uncontaminated process. (-) Require organic solvent and needs gas and solvent separation; batch process.
SAS	(+) Simple, scalable; solvent-free and uncontaminated process; homogeneous, small and stable liposomes; low use of organic solvent and moderate pressure and temperature. (-) Require organic solvents and needs gas and solvent separation; difficult to optimize conditions.
ASES	(+) Rapid, scalable and single step process; more adequate for dry liposomes; low organic residues. (-) Heterogeneous and large liposomes; uses a nozzle; understudy method.
SCRPE	(+) Simple, rapid and one-step process with scalable potential; no need for nozzles; reduced or no use of solvent; stable liposomes. (-) Understudy method; require high pressure; high cost material.
Dual asymmetric centrifugation	(+) Simple, rapid and reproducible process; homogeneous and small liposomes; high encapsulation efficiency for water soluble drugs. (-) Used only for small volumes; only laboratory-scale, not adequate for scale-up production, high pressure with agitation; understudy method.
Microfluidics	(+) Scalable process and used for biological samples; liposomes with controllable size. (-) Issues for thermolabile compounds; complex equipment; not adequate for scale-up production; difficult to clean after liposome production.

The synthesised liposome vesicles could be developed one step further to be used in stimuli-responsive microcargo delivery methods. For this purpose, generally, two distinct properties are desired for these smart delivery systems. Firstly, the liposome vesicle should be able to interact with its surroundings with active targeting. The active targeting can be achieved with the functionalisation of the liposome vesicle with ligands [65]. On the other hand, the stimuli-responsive delivery could be achieved with different kinds of external stimuli such as thermal, light, change in pH, or applied magnetic field.

**Literature example of thermo-responsive liposome vesicle :** Since the surface of liposome vesicles could be functionalised with ligands for active targeting, they are generally used for on-site treatment of cancer variants. Recently, Dayyih et al. investigated a method based on thermoresponsive liposome vesicle for encapsulating and delivering hypericin, an alternative type of substance for cancer treatment to chemotherapy [5]. Due to its hydrophobic structure, hypericin has not been used widely for treatment [66]. However, hypericin is a great candidate for photodynamic therapy, which is a selective and self-regulated therapy alternative for destroying cancer cells while not harming the adjacent cells. The reason is that hypericin could react with molecular oxygen when stimulated, leading to the formation of singlet oxygen or reactive oxygen species in cancer cells, eventually leading to necrosis, apoptosis, and autophagy-associated cell death [67].

For the delivery of hypericin to the cancer cells, Dayyih et al. loaded hypericin between the bilayer of PEGlated liposome vesicle, **Figure 2.7**. The release mechanism is based on the thermal disintegration of the liposome vesicle by reaching its phase transition temperature. They reported that the first change in phase transition temperature was 37.5°C and a maximum of 41.1°C [5]. When the intact liposome vesicle reaches its maximum phase transition temperature, it cannot retain its bilayer structure and hence release the hypericin within itself, **Figure 2.3**.

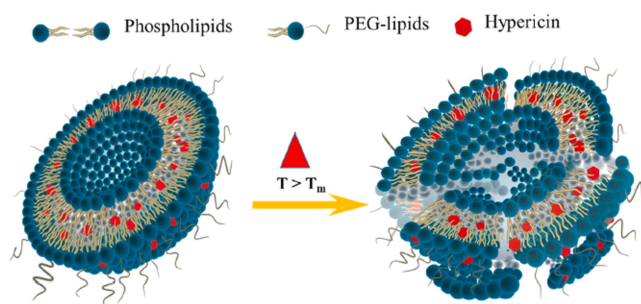


Figure 2.7: The schematic representation of thermoresponsive liposome vesicle. Reprinted with permission [5]. Copyright International Journal of Pharmaceutics 2021

**Literature example of light-responsive liposome vesicle:** Light responsive liposome vesicles offer an excellent alternative for stimuli-responsive drug delivery in vivo applications. For this concept, Yavlovich et al. designed a liposome vesicle composed of dipalmitoyl phosphatidylcholine and diacetylene phospholipid to deliver Doxorubicin. Doxorubicin is a type of chemotherapy drug which can be stimulated via 514 nm laser. In this study, rather than stimulating the lipid bilayer, Yavlovich et al. used the photoactivation of Doxorubicin for the photodestabilisation of diacetylene phospholipid in the liposome vesicle for the leakage of the drug to the environment [6]. They reported that, although the release mechanism was uncertain and unparallel to their previous studies, they did observe the release of Doxorubicin. Therefore, they concluded that the release mechanism in their work is strongly coupled with the photoactive load in the liposome vesicle rather than the photo-polymerisation of diacetylene phospholipid. From **Figure 2.8**, it can be observed that the liposome vesicles start releasing the drug to the environment upon laser activation near the cancer cell. Afterwards, the Doxorubicin could enter the cancer cell via passive diffusion and eventually kill it, **Figure 2.8**.

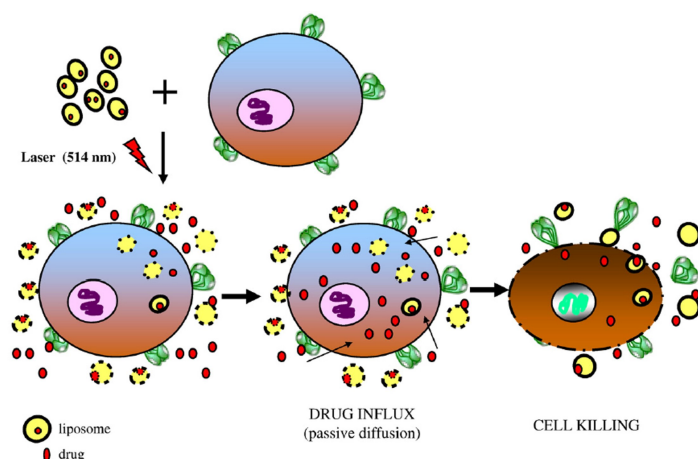


Figure 2.8: The schematic representation of mechanism of light-responsive liposome vesicle. Reprinted with permission [6]. Copyright Biochimica et Biophysica Acta 2011

**Literature example of pH-responsive liposome vesicle:** In recent years, rather than direct injection, encapsulation and release of drugs/microcargo got attention for therapeutic application. For the targeted release, the encapsulated microcargo must be activated upon external stimuli on site. pH-responsive liposome vesicles offer an alternative way of transporting microcargo with pH-active ligands. Yoshizaki et al. had taken one step further from using conventional liposome vesicles. In their work, they have modified their liposome vesicle bilayers with pH-sensitive hyperbranched polymer, 3-methyl-glutaryl-ated hyperbranched poly(glycidol) [7]. They reported that Cytotoxic T lymphocytes (CTLs), a type of white blood cell, can kill tumour cells directly. Therefore, the induction of these cells is crucial for immunotherapy. However, the direct injection of short peptide solutions derived from ovalbumin to induce CTLs is an inefficient way of activating these white blood cells, **Figure 2.9**. Thus, they have used hyperbranched polymer modified liposome vesicles to deliver the short peptide solutions. The upside of this mechanism is that the liposome vesicles can enter the dendritic cells whose cytosol is weakly acidic around  $\text{pH} = 5$ . Yoshizaki et al. reported that their liposome vesicles retain their form at  $\text{pH} = 7.4$  and release their cargo at  $\text{pH} = 5$ . Since the dendritic cells can enter lymphoid tissue and the short peptides can be released in these dendritic cells, the CTLs can be activated more. This greater activation results in a stronger therapeutic effect, **Figure 2.9**.

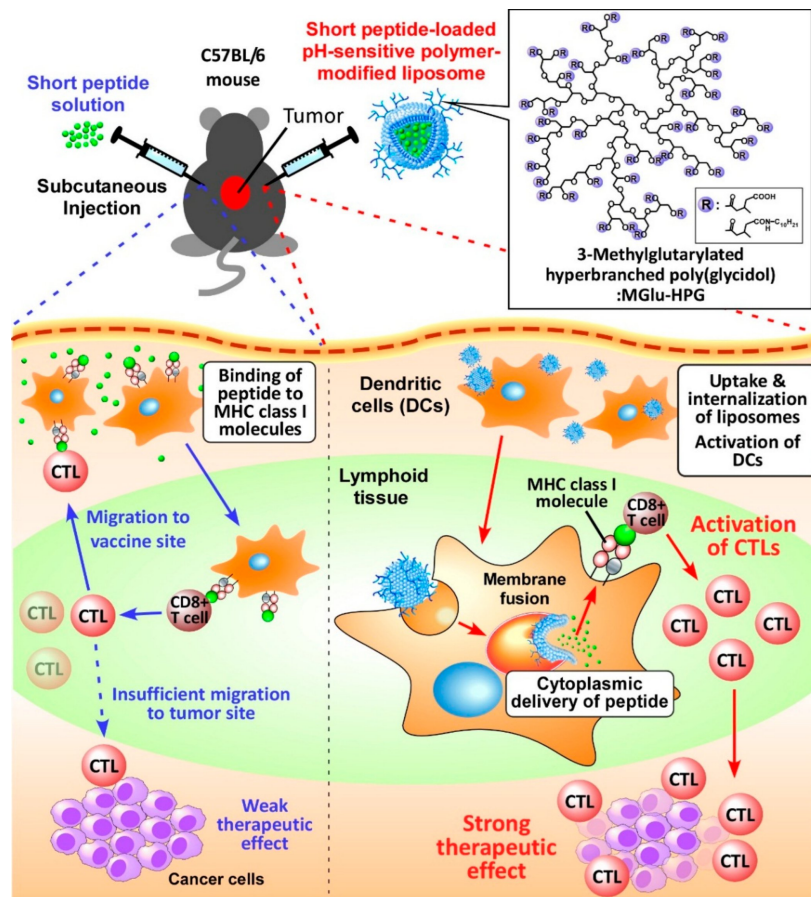


Figure 2.9: Direct injection of short peptides into mice for CTL activation, left. Use of pH-responsive hyperbranch polymer modified liposome vesicle for CTL activation. Reprinted with permission [7]. Copyright molecules 2016

**Literature example of magneto-responsive liposome vesicle :** A relatively new way of using liposome vesicles for responsive release combines them with magnetic properties. In this way, the liposome vesicles can be stimulated via magnetic fields. Vlaslova et al. designed a magnetic liposome vesicle that can release microcargo via low frequency alternating magnetic field. [8]. They used magnetic iron oxide nanoparticles to dope different kinds of liposome vesicles. The nanoparticles were surface functionalised to be hydrophobic in order to dope them into the lipid bilayer of liposomes, **Figure 2.10**. In their work, unlike the thermoresponsive liposome vesicles, applying the magnetic field at low frequencies did not increase the liposome vesicle's temperature. Therefore, they concluded that the disintegration of the lipid bilayer of the vesicle was not caused by the rise of the temperature above the phase

transition temperature. In fact, the disintegration of the lipid bilayer was caused by the collective movement of magnetic nanoparticles in the lipid bilayer, as shown in **Figure 2.10**. With the proposed mechanism, they successfully are able to release calcein microcargo into the environment.

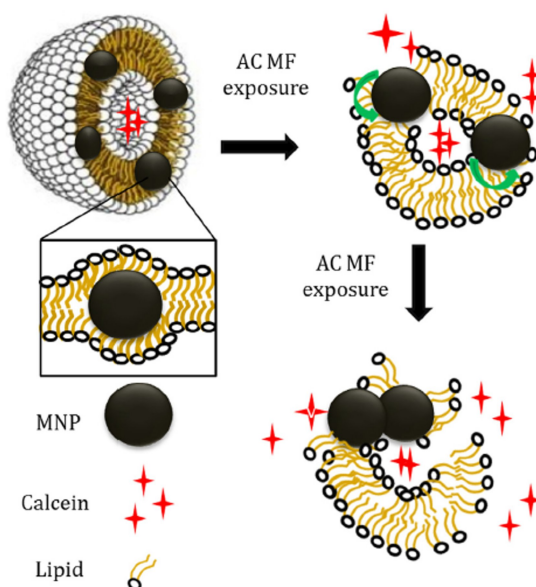


Figure 2.10: Schematic representation of alternating magnetic field actuated magnetoresponsive liposome vesicle. Reprinted with permission [8]. Copyright Journal of Colloid and Interface Science 2019

Even though liposome vesicles offer various application fields for active microcargo delivery, they are restricted in some ways. Most of the production methods in **Table 2.1** are not suitable for industrial-scale production for three main reasons. The first reason is that these production methods may require sophisticated equipment, which requires great equipment investment at the industrial scale. Second reason is that these ways of producing liposome vesicles are not suitable for industrial scale and are underdeveloped. Third reason is that even the industrial scale production was achieved, most liposome vesicles have stability issues, resulting in microcargo leakage off demand. Therefore, it is desired to have an alternative way of highly controllable on-demand release systems. For this purpose, active microparticles are used to have microcargo release on demand. These particles are excellent candidates for this topic since they are easily fabricated, the microcargo loading mechanisms are simple, and the microparticles can be stimulated in various ways.

### 2.1.3 Active microparticles

One other way to deliver and release microcargo is to use active microparticles. These microparticles can be in different shapes and sizes. The microcargo can be loaded with various methods such as physical adsorption, electrostatic interaction, and layer-by-layer coating. The delivery of the active microparticles is generally done with the use of magnetic fields. Besides magnetic fields, disease-related chemical gradients can also be used to steer the active microparticles to a predetermined destination [68]. The activation methods are generally referred to as follows. Magnetophoresis is the use of an external applied magnetic field to stimulate movement. Electrophoresis is the use of an applied electric field to stimulate movement. Diffusiophoresis is the use of chemical gradients to move in a media. The particle motion could also be triggered by creating a pressure gradient around the particle via ultrasonic waves. The on-demand activation of the microparticle can vary depending on the application, microparticle type, environmental conditions, requirements etc.

**Literature example of microcargo release with active particle using difussio-phoresis:** De Avila et al. used an active microparticle that uses magnesium as fuel in the stomach's acidic environment. They synthesized their active particle with a layer-by-layer deposition approach shown in **Figure 2.11-a**. Their motivation was to effectively eliminate the bacterial infection in the stomach with these active particles. The inner core of the particle was made of Mg, which reacts with HCl and produces  $H_2$  gases as product, **Figure 2.11-b**. With this reaction, De Avila et al. made the microparticle move anisotropically in the stomach's acidic fluid while delivering the drug CLR, loaded in polylactic-co-glycolic acid (PLGA), **Figure 2.11-g**. The Mg core was coated with  $TiO_2$ . This coating ensures the anisotropic movement since the only contact point for the gastric fluid, and the Mg core was the surface that was in contact with the glass slide in the production of the particles. On top of  $TiO_2$  layer, a third layer of CLR+PLGA was coated. Lastly, they covered the particle with chitosan polymer layer to deliver the microparticles to the stomach more efficiently. They reported that this polymer layer ensures efficient electrostatic adhesion of the active microparticle to the mucosal layer on the stomach wall while protecting the CLR-loaded PLGA layer. With this method, they report a successful reduction of

infection [9].

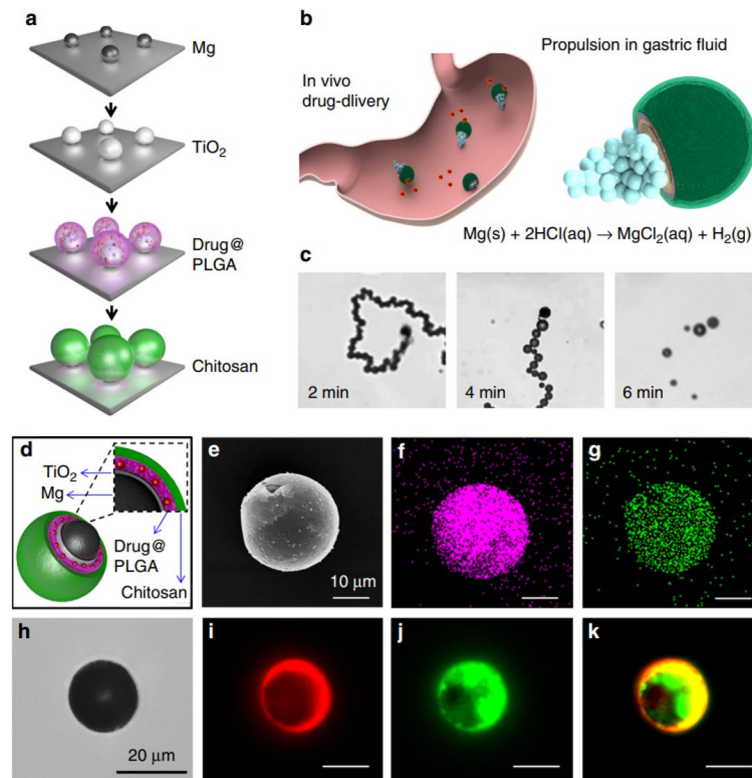


Figure 2.11: a) Schematic representation of layer-by-layer production process. b) The schematic of the working principle of the active microparticle. c) Real micrographs of the particle in pH = 1.3 acidic media. d) Layers of the microparticle. e-f) SEM image and EDX analysis of the particle respectively; pink is for Mg and green is for TiO<sub>2</sub>. h-k) Optical and fluorescence images of dye loaded active microparticle. i- is for PLGA layer, j- is for chitosan layer, and k- is for both layers respectively. Reprinted with permission [9]. Copyright Nature Communications 2017

**Literature example of microcargo release with active particle using electrophoresis:** Even though the diffusiophoretic motion of active microparticles offers a wide range of application areas, they are limited by their reaction's efficiency. Furthermore, these microparticles need certain media to be used as microcargo carriers. Therefore, there are alternatives to these particles in which the external stimuli cause physical phenomena rather than chemical reactions. One of these alternatives is using electrical fields to move the microparticles. Kim et al. synthesized multisegmented Au/Ni/Au nanowires ranging from 0.8  $\mu\text{m}$  to 10  $\mu\text{m}$  in length, acting as rotors. In

order to anchor these microrotors into designated positions, they have used patterned nanomagnets ranging from  $0.2 \mu\text{m}$  to  $2 \mu\text{m}$  in diameter, **Figure 2.12-b**. For the initiation of the movement, they have used quadruple microelectrodes acting as stators as shown in **Figure 2.12-a** [10]. In order to dope the microcargo, the multisegmented nanowires were coated with mesoporous  $\text{SiO}_2$  and the microcargo, Nile blue, was loaded with physical deposition. They reported that they could precisely control the release rate by adjusting these nanowire assemblies' rotation speed, **Figure 2.12-c,-d**.

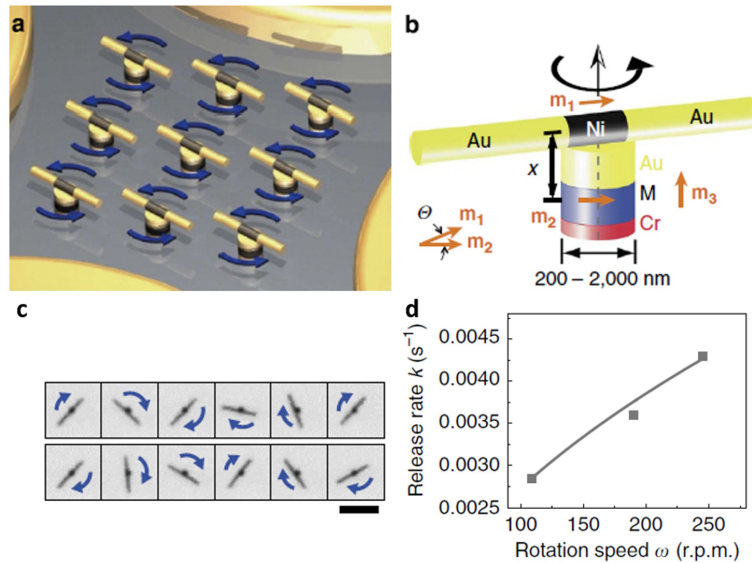


Figure 2.12: a) Schematic representation of the designed system working under applied electric field. b) Schematic representation of the nanowire assembly on top of magnetic anchor. c) Micrographs of rotating nanowire at different time intervals, scale bar is  $10 \mu\text{m}$ . d) Release rate of Nile blue with respect to rotating speed of nanowires. Reprinted with permission [10]. Copyright Nature Communications 2014

**Literature example of microcargo release with active particle using ultrasonic waves:**

Another promising way of delivering microcargo is to use ultrasonic waves to move the microparticles since the ultrasonic waves can penetrate human tissue. Any microparticle that can be actuated with ultrasonic waves is an alternative for therapeutic applications. Wu et al. designed a red blood cell-based microparticle that can move upon ultrasonic wave actuation [11]. For testing the drug-carrying characteristics, they doped the microparticle with an anticancer drug, doxorubicin. The micromotor is also functionalised with magnetic nanoparticles. The existence

of these magnetic nanoparticles allows the steering of the drug-loaded microparticle under ultrasonic wave actuation as shown in **Figure 2.13-a,-b**. They reported that it is possible to control the velocity of the microparticles by adjusting the transducer voltage for the ultrasonic wave generation, **Figure 2.13-c**. Wu et al. tested the microparticle's drug carrying capacity by comparing it to a free drug case. The reason is that therapeutic drugs such as doxorubicin can also damage the healthy cells along with killing cancer tissue. Therefore, the targeted release of these drugs is crucial. Wu et al. reported that they observed three folds increase in the viability of the cells when the doxorubicin was carried with microparticle as compared to the free doxorubicin case, **Figure 2.13-d**.

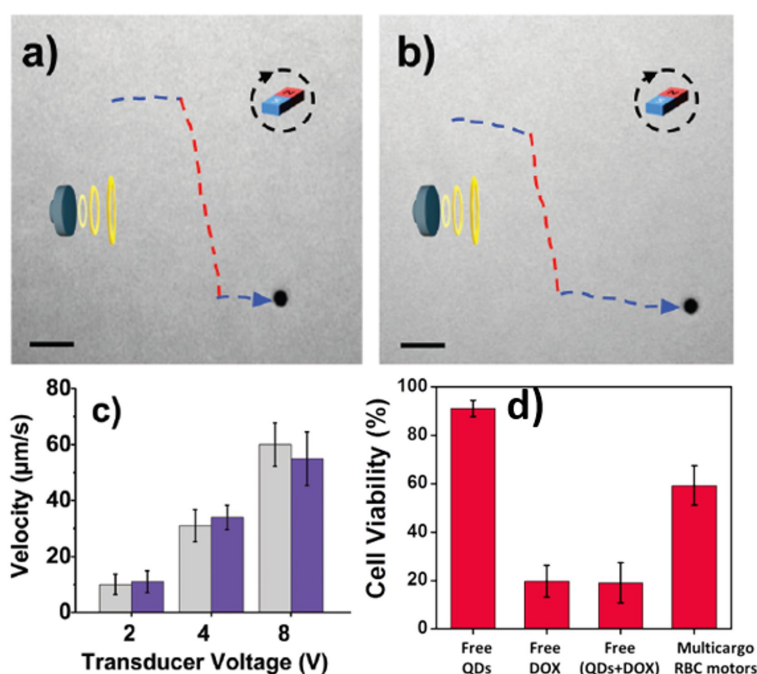


Figure 2.13: a) Red blood cell based magnetic nanoparticle loaded microparticle. b) Red Blood Cell based magnetic nanoparticle, doxorubicin and quantum dots loaded microparticle under ultrasonic wave actuation with applied magnetic field. Scale bars are  $20 \mu\text{m}$  for both image. c) The velocities of microparticles under different transducer voltages. d) The viability study of Human Umbilical Vein Endothelial Cells at the vicinity of the microparticles and free quantum dots, doxorubicin and the mixture of two. Reprinted with permission [11]. Copyright The Royal Society of Chemistry 2015

### Literature example of microcargo release with active particle magnetophoresis:

Magnetic fields can also be used to trigger the release of microcargo besides the guidance of the microparticle to the dedicated designation. The movement of the microparticle can be done with the help of the irregular-shaped design of the particle to mimic the swimming behaviour of microorganisms. Liu et al. synthesized a worm-like microparticle to actuate the microparticle and release the microcargo with the help of a magnetic field. The main frame of these microparticles is the assembly of mesoporous silica nanotubes. These nanotubes are designed to both adsorb the  $\text{CoFe}_2\text{O}_4$  magnetic nanoparticles and 6-carboxyfluorescein as the drug onto themselves, shown in **Figure 2.14-a**. Even the 6-carboxyfluoresceins molecules are released by free diffusion, the release rate can be controlled by adjusting the alternating magnetic field frequency, shown in **Figure 2.14-b,-c**.

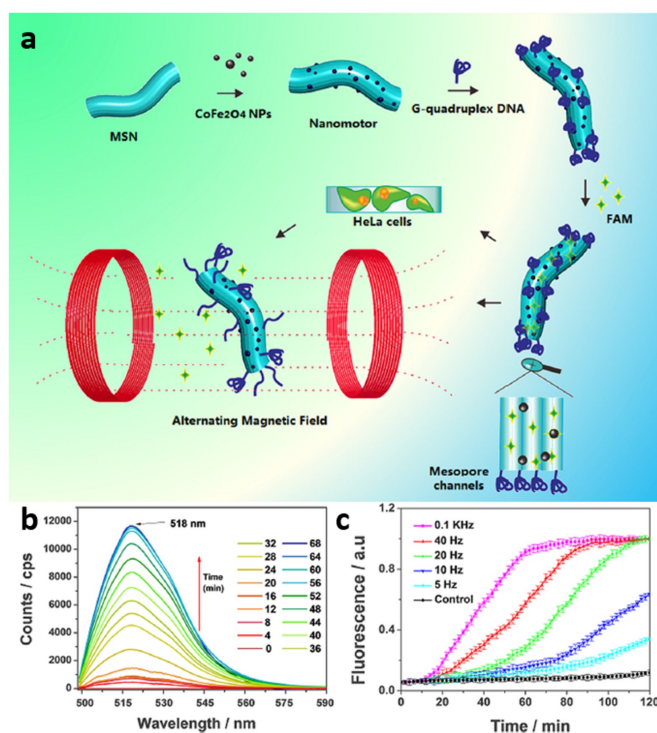


Figure 2.14: a) The schematic representation of working principle of magnetically driven mesoporous silica micromotors carrying 6-carboxyfluorescein as drug. b) The real-time fluorescence spectrum collected in the 6-carboxyfluorescein releasing process. c) Plot of fluorescence at 518 nm against the exposure time in different frequency magnetic fields. Reprinted with permission [12]. Copyright ACS Applied Materials and Interfaces 2015

The microcargo release via active microparticles is an excellent alternative to the current microcargo release since these particles can be actuated with external stimuli and targeted for specific locations. However, some of these activation methods are not suitable for a wide range of applications. For example, the diffusiophoretic motion of these particles using  $H_2O_2$  fuel is not desired in vivo applications since the high concentration of  $H_2O_2$  potentially damages the cells. Moreover, the direct drug loading of these microparticles limits the amount of microcargo release. Therefore, we intended to design a system that takes advantage of the encapsulation efficiency of oil structures as liposomes beside the controllable on-demand actuation of microparticles.

## **2.2 Microcargo release with liquid crystals**

There are many studies that use liquid crystal assemblies to fabricate stimuli-responsive microcargo release systems. [69], [70], [71], [72], [73]. In order to further comprehend the included mechanism for microcargo release, the interactions between liquid crystal and other substances should be investigated.

### **2.2.1 Aqueous-Liquid crystal interfaces**

Even though the liquid crystal-based systems are designed with chemically functionalized solids, recent studies of liquid crystal systems designed with free interfaces have been reported. [22] [74] [75] [76] [77] Among these studies, the aqueous-liquid crystal interface has several characteristic differences from solid-liquid crystal interfaces. Firstly, unlike solid interfaces, aqueous interfaces are soft and deformable, which makes the interface more dynamic. Secondly, any adsorbate can be transported to the aqueous-liquid crystal interface through the aqueous domain. These molecules adsorbed on the interface are going to be highly mobile compared to solid interfaces. The last point is critical since this high mobility at the interface allows the LC to reorganize itself in response to any elastic stresses rapidly.

When there are no adsorbates, the average nematic LC orientation is typically planar but azimuthally degenerate, e.g. on the same plane as the interface plane but not

always on the same direction. On the other hand, when an amphiphilic adsorbate is introduced to the LC/aqueous interface, these adsorbates are located between liquid crystal mesogens and water molecules while interacting with both closely. Hence, due to the steric interaction between LC mesogens and amphiphilic adsorbates, the nematic LC orientation deviates from planar anchoring [26]. As a result, one can get cross-polarized optical feedback from this versatile interaction. For example, Gupta and Abbott used a positively charged surfactant, dodecyltrimethylammonium bromide (DTAB), to trigger continuous optical feedback meaning a continuous tilting of the LCs at the aqueous-liquid crystal interface [13]. From **Figure 2.15** it can be observed that as the DTAB concentration goes from  $0 \mu\text{M}$  to  $50 \mu\text{M}$ , the appearance of the liquid crystal goes from colourful, which indicates planar anchoring with azimuthal degeneration, to black which indicates homeotropic anchoring, since the LC mesogens are perpendicular to the orthogonal polarized filters located at the bottom and the top of the sample. It is also noticeable that in **Figure 2.15** as the liquid crystal amount increases, as the depth of the sample increases from  $5 \mu\text{m}$  to  $40 \mu\text{m}$ , more DTAB was needed to convert whole LC layer from planar anchoring to homeotropic anchoring.

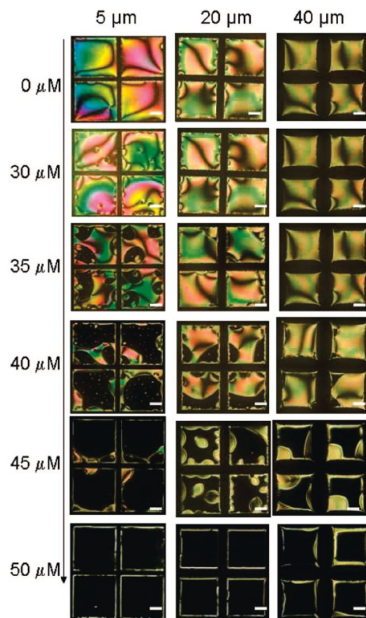


Figure 2.15: Cross-polarized microscopy micrographs of aqueous-liquid crystal interface at different DTAB bulk concentrations for 5-,20-, & 40- $\mu\text{m}$  liquid crystal film respectively. Reprinted with permission, [13]. Copyright 2009 Langmuir

From this study, one can deduct that in the absence of any surfactant, the liquid crystal mesogens at the aqueous interface maintain planar anchoring, which was crucial for our designed systems to work since this planar anchoring has an essential role in keeping the aqueous microcargo loaded droplets in LC domain with creating an elastic energy barrier. On the other hand, one can also deduct from **Figure 2.15** that with the presence of a positively charged surfactant, such as DTAB, the LC anchoring turns entirely to homeotropic after  $50 \mu\text{M}$  for all three liquid crystal thicknesses. This information is vital for our designed system since the aqueous microcargo droplets must also be loaded with a surfactant above the threshold value for homeotropic anchoring. This way, there would be a disagreement between the LC mesogens around the aqueous microcargo droplets and at the aqueous interface. Therefore the microcargo droplets could remain in the LC domain without external stimuli, shown in **Figure 1.4**

The physical interaction at LC/Aqueous interface with optical feedback is not restricted to surfactant molecules. Wang et al. reported that with the help of selective binding, they could confirm the existence of cocaine in urine samples by investigating the optical feedback of a liquid crystal-based system. In their design, they have used an aptamer on the liquid crystal/aqueous interface to have homeotropic anchoring.

### 2.2.2 Colloidal interactions in liquid crystals

The ratio of  $\lambda_{dGK} = K/W_a$  is the average elastic constant to the anchoring coefficient has dimensions of length, and it is called de Gennes-Kleman length. This ratio is typically around  $0.1 \mu\text{m}$  to  $10 \mu\text{m}$  for  $K = 10 \text{ pN}$  and  $W_a \sim 10^{-6}$  to  $10^{-3} \text{ J/m}^2$  [14]. Notice that the ratio size is in a few micrometers and leads to interesting features regarding colloidal interactions in LCs. When colloids or microparticles are in liquid crystals, the liquid crystal mesogens in the vicinity of these colloids typically deviate from their average nematic orientation set by the far-field nematic director. The reason for this deviation could be explained by the two key concepts of liquid crystals; surface anchoring and elasticity of liquid crystals, respectively. When a colloidal particle is introduced to the nematic LC phase, there should be a balance between surface anchoring force due to newly introduced surface of the colloid and elastic energy dis-

tortion force due to the existence of the colloid. The surface anchoring energy and the elastic energy of the distortions could be estimated with  $\sim W_a R^2$  and  $\sim KR$ , respectively, where  $R$  is the particle radius. Assume a colloidal particle with radius,  $R$ , having perpendicular surface anchoring on its surface. Two possibilities occur when this colloidal particle is introduced to the nematic LC phase. If  $R \leq K/W_a$ , the particle does not disturb the nematic director mostly, shown in **Figure 2.16-a**. However, if  $R \geq K/W_a$  the particle distort nematic director in its vicinity, **Figure 2.16-b,-c**.

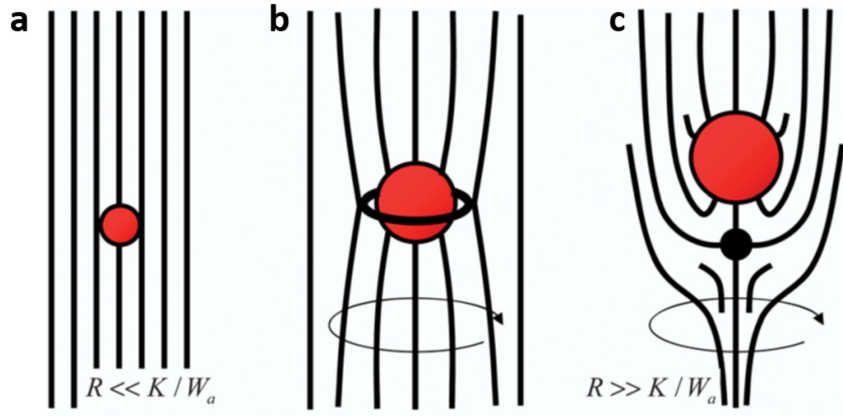


Figure 2.16: a) Colloidal particle in nematic LC phase with  $R \leq K/W_a$ . b-c) Colloidal particle in nematic LC phase with Saturn Ring and hyperbolic hedgehog respectively, when  $R \geq K/W_a$ . Reprinted with permission, [14].Copyright 2014 Soft Matter

In **Figure 2.17** two common and one specific condition LC nematic director profiles around microparticles were presented for  $R \geq K/W_a$ . Tangential anchoring, just like planar anchoring, produces quadrupolar distortions in LC with two diametrically opposed surface defects, so-called boojums [78] shown in **Figure 2.17-a**. **Figure 2.17-b** represents the homeotropic surface anchoring with dipolar symmetry, so-called hyperbolic hedgehog point defect. The homeotropic anchoring in **Figure 2.17-c** is usually unstable and the disclination line turns into a point defect to from **Figure 2.17-d** [79].

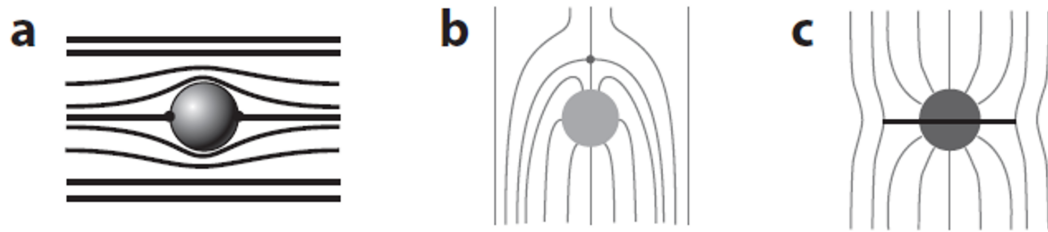


Figure 2.17: a) Tangential surface anchoring of LC around spherical particle. b) Homeotropic surface anchoring of LC around spherical particle with hyperbolic hedgehog defect above. c) Special case of homeotropic anchoring, a particle with homeotropic anchoring with Saturn defect loop around it. a- Reprinted with permission, [3].Copyright 2016 Annual Reviews. b-,c- Reprinted with permission, [15].Copyright 2006 Science

The topological defects around these colloidal particles play a crucial role in designing self-assembled systems. Musevic et al. used the topological defect concept in nematic LCs by introducing colloidal particles. They constructed 2D self-assembled structures in nematic LC phases [15]. They used silica microparticles,  $d = 2.32 \pm 0.02 \mu\text{m}$ , having homeotropic surface anchoring. These particles are positioned in LC-filled sandwich cells via laser tweezers. The cells' glass surfaces were chemically treated, so that parallel surface anchoring occurs in the rubbing direction. When the thickness of the cells were greater than  $3.5 \pm 0.1 \mu\text{m}$ , the resulting elastic distortion around the particles generates a repulsive force between the walls of the cell and the colloid, stabilizing the colloids in the middle of the nematic layer. In **Figure 2.18-a** one can observe a colloidal particle with dipolar hyperbolic hedgehog defect located along rubbing direction. They reported that these particles spontaneously assembled into chains oriented along rubbing direction, **Figure 2.18-b**. When the cell thickness was smaller than the critical value reported above, the dipolar fields around the particles were affected by the cell walls. The symmetry of the distortion around the particles becomes a quadrupolar Saturn ring, shown in **Figure 2.18-c**. Interestingly, these particles spontaneously assembled into kinked chains oriented perpendicular to the rubbing direction. They also reported that the binding energies of additional colloid were  $\sim 800 k_B T$  and  $4500 k_B T$  along the chain direction for quadrupolar and dipolar defects, respectively. This result also emphasizes the effect of topological de-

fects in LC-based systems even though the defect sizes are around a few nanometers.

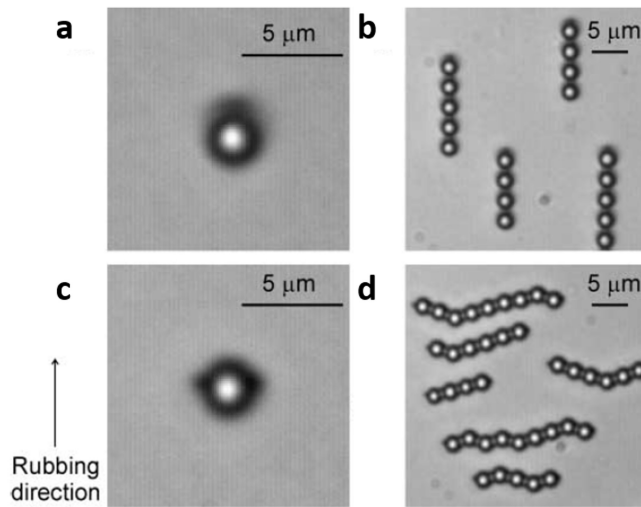


Figure 2.18: a) Colloidal particle with hyperbolic hedgehog defect. b) Chain formations of colloids along rubbing direction due to hyperbolic hedgehog defects. c) Same colloidal particle in part a, with Saturn ring disclination around equator. d) Kinked chain formations perpendicular to rubbing direction due to Saturn ring disclinations. Reprinted with permission, [15]. Copyright 2006 Science

### 2.2.3 Interfacial behaviour of colloids and molecular adsorbates on liquid crystals

Just as chemically functionalized solid surfaces can determine the surface ordering of LC, the change in surface ordering in LC can control the organization of interfacial adsorbates. The latter case is a promising principle for designing responsive materials that can be actively controlled.

A great example for a responsive material design based on colloid interactions on LC/Aqueous interface can be given from the study [16] shown in **Figure 2.19**. The nematic LC they have used, 5CB, adapts planar anchoring having a parallel flat interface to water, **Figure 2.19-a**. When they introduced silica microparticles,  $d = 2.3 \mu\text{m}$ , having homeotropic anchoring on their surface, the particles far enough from other particles sedimented near point defects, shown in **Figure 2.19-a,-b**. When the particles were close enough, the attractive force between particles created dendritic struc-

tures due to the presence of attractive dipolar interaction between particles, shown in **Figure 2.19-c**. Interestingly, when sodium dodecylsulfate (SDS) was introduced to the system, the attractive dipolar interaction between the particle pairs was changed to repulsive due to the rotation of the topological dipole of the LC by SDS. The point defect near the particle was relocated below the particle as the SDS concentration increases, shown in **Figure 2.19-d,-e**. Meanwhile, the magnitude of the repulsive interaction between the particles also increases, resulting in the change in the microparticle assembly patterns from chain-like structures to hexagonal arrays, **Figure 2.19-g**. The study provides proof of concept for the design of chemo-responsive arrays of colloids at the LC/Aqueous interface.

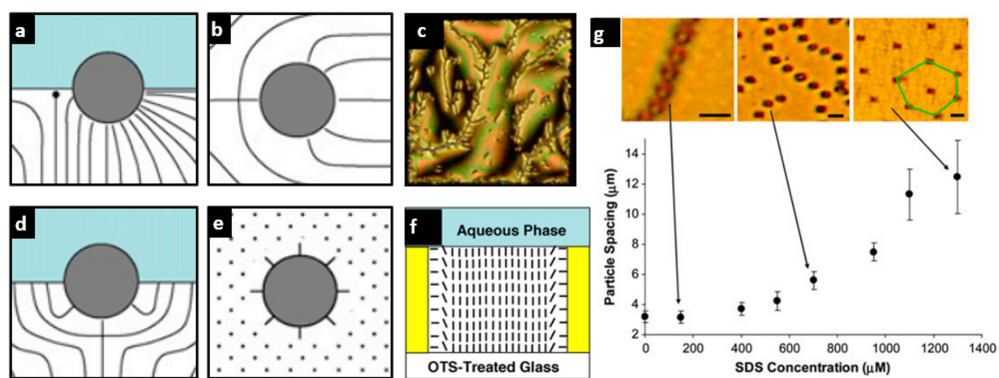


Figure 2.19: a,b) Silica microparticle sedimented on LC/Aqueous interface with homeotropic anchoring near a topological defect. The interface has planar anchoring. c) Self-assembled dendritic structures on the LC/Aqueous interface formed by attractive interaction between silica microparticles. d,e) Topological defect relocated below silica microparticle. f) Homeotropic surface anchoring at LC/Aqueous interface due to presence of SDS. g) Microparticle patterns as a function of SDS concentration at the LC/Aqueous interface. Reprinted with permission, [16]. Copyright 2010 PNAS

**Literature example of microcargo release from liquid crystal emulsions via mechanical shear :** Water-in-LC emulsions can be constructed with the help of simple surfactant molecules. Kim et al. reported that they could eject the aqueous microdroplets with red tracer from the water-in-LC emulsion by interfacial stress [2]. The aqueous microdroplets were trapped in the LC with 2mM DTAB surfactant. They observed that with the application of the interfacial shear, LCs could be reoriented

as shown in **Figure 2.20-a-d**. They reported that when there is no external applied shear, the microdroplets in the emulsion should stay in the emulsion at equilibrium. However, when they introduced approximately  $10 \text{ N/m}^{-2}$  via a magnetic stirrer located near their emulsion, the interfacial stress caused by the aqueous environment triggered the ejection of the droplets as shown in **Figure 2.20-g,h**. They supported their experimental observation with theoretical calculations about the change in the net force balance with the introduction of interfacial stress, **Figure 2.20-e,-f**.

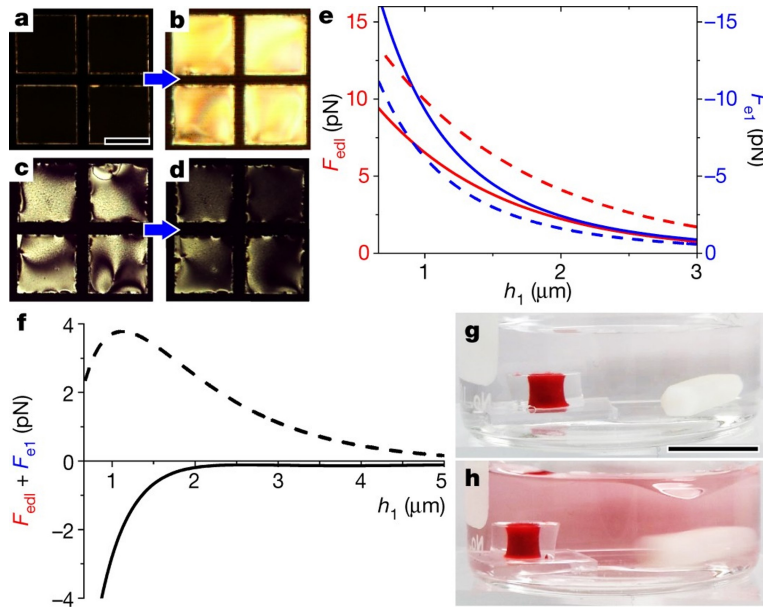


Figure 2.20: a-d) Cross-polarized optical response of LC films in  $40 \mu\text{m}$  TEM grid with chemically treated substrate and the overlying aqueous phase. Scale bar is  $200 \mu\text{m}$  a,b) Initially homeotropic anchoring at the LC/Aqueous interface, before and after applied interfacial stress. c,d) Initially planar anchoring at LC/Aqueous interface, before and after applied interfacial stress. e,f) Calculated  $\mathbf{F}_{EDL}$  (red lines) and  $\mathbf{F}_E$  (blue lines) and  $\mathbf{F}_{Net}$  (black lines) for an aqueous microdroplet ( $R = 1.5 \mu\text{m}$ ). Planar and homeotropic orientations were represented with solid and dashed lines respectively. g,h) Photographs of the ejection of the microdroplets from water-in-LC emulsion, before and after stirring the overlying the aqueous phase with magnetic bar. Scale bar is 1 cm. Reprinted with permission, [2]. Copyright 2018 Nature

**Literature example of microcargo release from liquid crystal emulsions via polyelectrolytes :** The electrostatic interaction between LC and aqueous phases can be tuned to construct microcargo release systems. Tsuei et al. used this concept to construct a liquid crystal-based microcargo release system with the help of interfacial polyelectrolytes [17]. The constructed water-in-liquid crystal emulsion entraps the aqueous microcargo droplets in the absence of external stimuli, **Figure 2.21-a**. When adsorption of poly(diallyldimethylammonium chloride) (PDDA) to the interface takes place, the surface anchoring of the liquid crystal changes resulting in the change in the direction of the net force acting on the aqueous droplets in liquid crystal and eventually resulting in microcargo release, **Figure 2.21-c**.

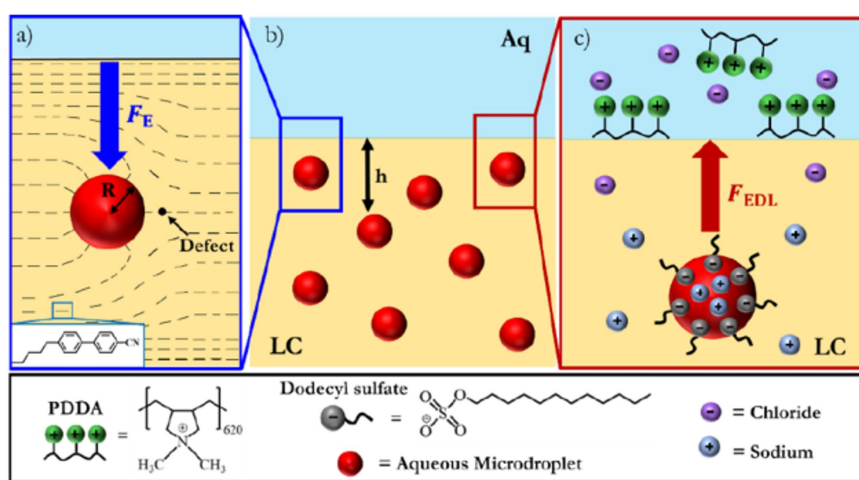


Figure 2.21: a) Aqueous microcargo droplet entrapped in liquid crystal domain. b) The positions of aqueous microcargo droplets. c) Release of aqueous microdroplets from LC media upon adsorption of surfactant PDDA. Reprinted with permission, [17]. Copyright 2022 Langmuir

Liquid crystal assemblies offer great versatility due to their encapsulation efficiency, a broad range of surface modifications for targeted applications and stimuli-responsive characteristics for microcargo release applications. We planned to combine the external stimuli property of active microparticles with water-in-liquid crystal emulsions to construct a microcargo release system that works with contact-free external stimuli with rapid response and ease of fabrication.



## CHAPTER 3

### MATERIALS & METHODS

#### 3.1 Materials

4-cyano-4'-pentylbiphenyl(5CB) and E7 were purchased from HCCH Jiangsu Hecheng Chemical Materials Co. **Figure 3.1**, Ltd. Dimethyloctadecyl[3-(trimethoxysilyl)propyl] ammonium chloride (DMOAP), polyvinyl alcohol (PVA), N,N-Dimethylformamide (DMF), sodium dodecylsulphate (SDS), cetyltrimethyl ammoniumbromide (CTAB), trisodium citrate, titanium(IV) butoxide, SYLGARD® 184 Polydimethylsiloxane (PDMS) were obtained from Sigma-Aldrich. Iron(III) chloride hexahydrate, Absolute ethyl alcohol(99.99%) were purchased from ISOLAB Laborgeräte GmbH. Glass slides and cover slips were obtained from Marienfeld (Germany). Ethylene glycol was purchased from Merck. 995 fineness gold was purchased from goldsmith. Approximately 20  $\mu\text{m}$  thick PVC cling film and fast curing epoxy were purchased commercially.

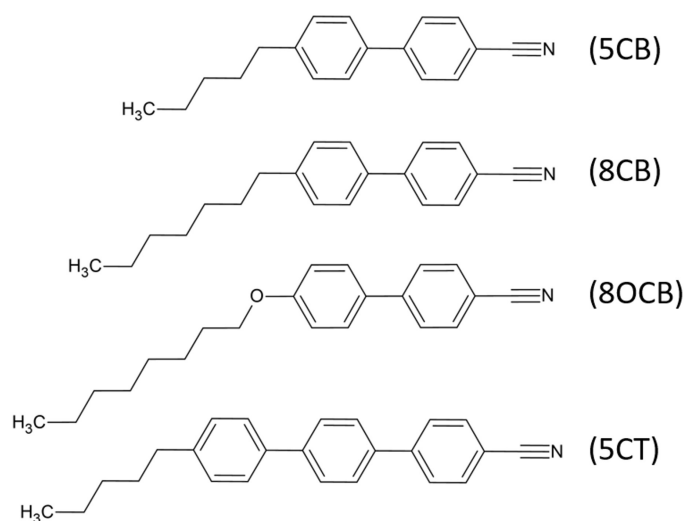


Figure 3.1: Molecules of E7 liquid crystal mixture.

### 3.2 Synthesis of TiO<sub>2</sub> microparticle

We have synthesized our TiO<sub>2</sub> microparticles via solvent evaporation/extraction method. Titanium butoxide, Ti(BuO)<sub>4</sub>, was chosen as the titanium precursor for this procedure [27]. For a typical synthesis, we have set the precursor – ethanol ratio to 1 : 40. We firstly take 40 mL of absolute ethanol (99.9v%) into a glass flask. While the magnetic stirrer was operating around 500 RPM, we slowly added 1 mL of Ti(BuO)<sub>4</sub> to the ethanol and seal the flask with parafilm. After 10 min of stirring, the flask was taken to a N<sub>2</sub> environment and incubated for 3 hours at room temperature in dark. In the first 5 minutes of incubation, the white precipitate formation should be observed. Later, the white precipitate was sedimented with centrifugation, at 10000 rpm for 10 min. After each sedimentation, the sediment washed with absolute ethanol and ultra-pure water (18.2 MΩ·cm) three times subsequently. Between each centrifugation step, the white precipitate was vortexed at 3000 rpm for 1 min and ultrasonicated at least 20 min until the homogeneous appearance was achieved. Lastly, the precipitate was taken to a quartz cell and dried at 60°C in a furnace at atmospheric pressure overnight. In order to achieve anatase crystal structure, which was chosen due to lower energy requirements compared to rutile structure [80], we calcinated the sample at 400°C and atmospheric pressure for 2 h with ramp up temperature, ΔT, of 2°C/min.

### 3.3 Synthesis paramagnetic iron oxide microparticle

We have selected a synthesis that can be scaled up easily. [28] In a typical synthesis, firstly we added 60 mL ethylene glycol to a flask. Then, 3.25 g of  $FeCl_3 \cdot 6H_2O$  was added and the flask was stirred at 500 RPM until the appearance was homogeneous. Subsequently, 0.72 g trisodium citrate and 3.60 g sodium acetate were added to the mixture. The mixture continued to be stirred until homogeneous appearance was achieved. The mixture was then divided into two teflon autoclaves. The autoclaves were closed and tightened mechanically. The samples autoclaved at 200°C for 10 hours. After incubation, the samples were cooled to room temperature via cold water bath. The obtained product appeared to be black. The product was transferred to another flask. The magnetic particles were collected via magnet. The solution media of the flask contents was changed to absolute ethanol after collecting the particles with magnet three times and then it was changed to ultrapure water (UP) (18M $\Omega$ .cm) with the same procedure. The particles again were collected on a watch glass and dried at 30°C in oven. Since the atmosphere was not controlled, the particles oxidized further and got brown appearance.

### 3.4 Size & surface characterisation of microparticles via SEM imaging

After synthesis, 0.5 mg of particles were dispersed in 1 mL ultrapure water. The dispersion was achieved via ultrasonication for 30 minutes and vortex at 3000 RPM for 1 minute. Scanning electron microscopy (SEM) stubs were covered with commercial aluminium foil and the contact between foil and stubs were achieved via carbon tape. 4 droplets, 30  $\mu$ L each, of the prepared samples were dropped onto stubs. Natural sedimentation of particles were allowed and the water was evaporated at room temperature by free convection. SEM images of the samples were taken at different elevations to reveal the average diameter and the surface morphology of the syntheses. For noble metal functionalized particles, backscattering images were also taken to reveal the anisotropic doping of noble metal on the hemispheres. Additional EDX area analysis was done for noble metal loaded TiO<sub>2</sub> microparticles.

### **3.5 Monolayer coverage of TiO<sub>2</sub> microparticles on glass substrate for noble metal loading**

In order to coat one of the hemispheres of TiO<sub>2</sub> microparticles, monolayer coverage of the glass substrate has to be achieved. Therefore, we have examined the micrographs of aqueous TiO<sub>2</sub> solutions in order to find the optimum particle areal density. For monolayer coverage of the glass substrate, we have dropped 0.3 mg/mL TiO<sub>2</sub> aqueous solutions of TiO<sub>2</sub> to glass substrates and let the water evaporate by slow natural convection.

### **3.6 Noble metal loading on TiO<sub>2</sub> microparticle hemisphere, Janus particle functionalisation**

To have anisotropic motion, the TiO<sub>2</sub> microparticles were functionalised as Janus particles. The functionalisation was planned with Au coating. Firstly, we have dispersed the TiO<sub>2</sub> particles in aqueous media. The concentration of particles was set to 0.3 mg/mL to have monolayer on glass slides. Then, we used ultrasonic bath for 15 min to separate the TiO<sub>2</sub> aggregates. The dispersed particles were transferred onto a glass substrate and water is slowly evaporated to achieve monolayer of TiO<sub>2</sub> microparticles on the surface. We checked the prepared glass slide samples for coating with optical microscopy for monolayer coverage. Before loading of the Au cap, each glass substrate was UV-Ozone treated to clean the surfaces from organic content.

#### **3.6.1 Au coating of TiO<sub>2</sub> hemispheres via ion sputtering**

Au coating was done with directional ion-sputtering with Pd support. The Pd supported Au cap thickness was chosen as approximately 30 nm, 1-2 wt.%, to have electron-sink for the electrons that are generated by UV illumination of the bare TiO<sub>2</sub> side of the Janus particle's electron-hole pairs [81].

### 3.6.2 Au coating of TiO<sub>2</sub> hemispheres via thermal coating

We have used another noble metal loading method since the catalytic activity of these particles strongly coupled with the coating method [82]. Monolayer coverage of TiO<sub>2</sub> microparticles was achieved on glass slides as previously mentioned. The glass slide samples were ozone-UV treated before the thermal coating step in order to cleanse the particles & glass surface from any organic impurities. First, 10 nm Cr interlayer directionally coated on the half side of TiO<sub>2</sub> microparticles and 30 nm Au coating was directionally coated on the same hemisphere. The particles were dispersed in aqueous media via gentle ultrasonication and pipette pumping.

### 3.7 Preparation of sandwich cell for mean square displacement (MSD) analysis

For viscosity calculations, we have prepared glass slide sandwich cells as follows. On a glass slide, approximately 40 $\mu$ m spacers were placed on both sides as shown in **Figure 3.2-a**. On top of the spacers, we placed a glass coverslip and aligned the corners of the cell. We used two paper clamps to fix the cell, **Figure 3.2-b**. After fixing, we fix the corners of the cell with epoxy. When the epoxy droplets at the corners are cured, the paper clamps can be removed, **Figure 3.2-c**. We filled the sandwich cells with the media we aimed to calculate its viscosity, containing microparticles. Lastly, we sealed the edges of the sandwich cells with epoxy to make a closed system for mean square displacement calculations, **Figure 3.2-d**.

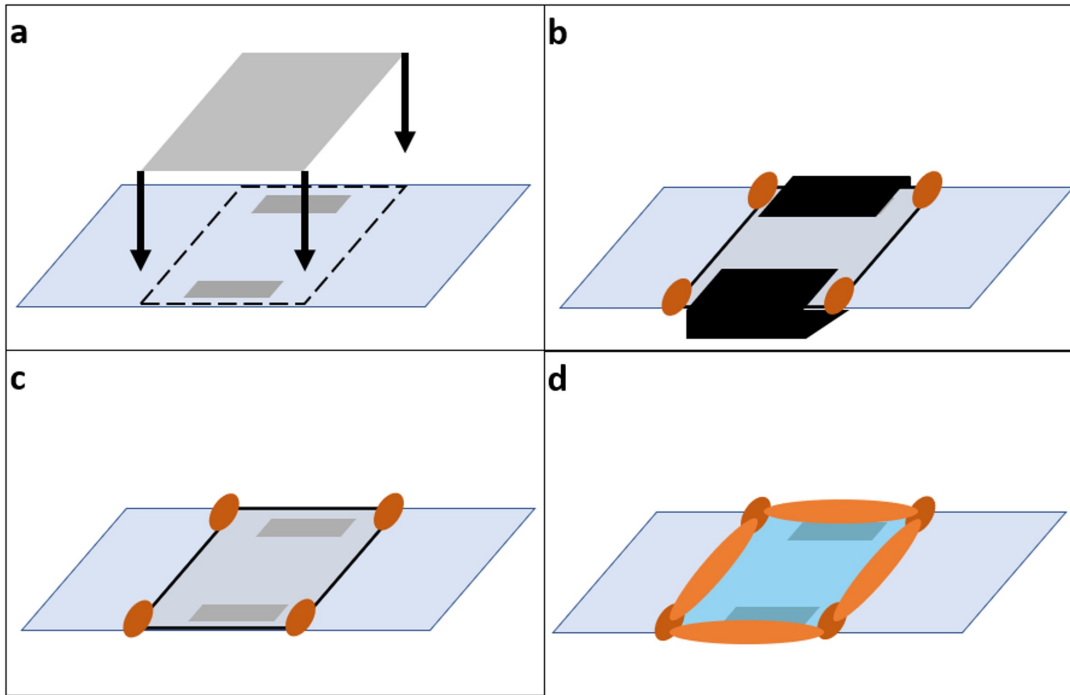


Figure 3.2: Sandwich glass cell preparation steps. a) Placing the cover glass onto spacers. b) Fixing the sandwich cell with paper clips and dropping epoxy to the corners of the cell. c) Removing of the paper clips after epoxy curing. d) Filling the sandwich cell with fluid and sealing the cell edges with epoxy.

### 3.8 DMOAP, PVA, and PI coating of glass sandwich cells

In order to align the liquid crystal nematic director in the sandwich cell, we used three surface modifications. Firstly, to have homeotropic anchoring on the glass surface, we coated the cell walls with DMOAP. The coating was done by immersing glass slides and coverslips into a 1v% aqueous DMOAP solution in a challet. The challet was ultrasonicated for 30 minutes at room temperature. We rinsed the glasses with ultrapure water and dried them with  $N_2$  to prepare the glasses for sandwich cell preparation. Secondly, we coated the sandwich cell walls with PVA or PI to have planar anchoring on the glass surface. The coatings for PVA and PI were done exactly by spin coating method. The glass slides were put on the spin coater and fixed in place with a gentle vacuum. On top of glass slides or cover glasses, a few drops of 5wt.% aqueous PVA solution were dropped. We spin the glasses at 1000 RPM for 120 sec with a 500 RPM start. After PVA coating we gently scratched the coated surface

a few times with microfiber cloth in one direction. The PVA-coated sandwich cells were constructed with two coated surfaces that were scratched in the same direction. For PI-coated sandwich cells 2wt.% PI in DMF solution was used. For PI coating, after spin coating, the glass substrates were heated to 230°C by a hot template for two and a half hours for PI curing.

### **3.9 Real time microparticle tracking via optical microscopy & mean square displacement (MSD) analysis**

We recorded the real time displacements of microparticles in various media for mean square displacement calculations. The prepared sandwich cells were placed under optical microscope. The transmission, polarized and polarized & retarded recordings of the particle motions were captured via integrated camera. The recording were taken at 640x480, 1280x960, or 2560x1920 pixel resolution and from 9 fps to 50 fps depending on the media. We processed the real time recordings in an open source computer program called FiJi [83]. The software included build in plugins for particle position tracking. We used two of the plugins called MOSAIC [84] & TrackMate [85] for microparticle position tracking. We analysed these positional trajectories and analysed the mean square displacements with custom MATLAB codes. The MATLAB codes can be found in **Appendix E**. As a rule of thumb, for each microparticle, at least 2500 position data was analysed to calculate mean square displacement at different time intervals to have statistical reliability. Each sandwich cell sample contained at least 25 alone microparticles. For each viscosity media, at least two independent sets of experiments were done, each set containing three independent samples.

### **3.10 Preparation of water-in-liquid crystal emulsion for microcargo release experiments**

The water-in-liquid crystal(LC) emulsions for the microcargo release experiments were prepared in three parts. In the first part, 20 mM of aqueous CTAB solution was prepared. The CTAB was dissolved in water via ultrasonication for 30 minutes between 25-35°C for complete dissolution. Meanwhile, 20 mg/mL aqueous methy-

lene blue (MB) solution was also prepared with ultrasonication. These two solutions were mixed together with a 1:9 ratio for CTAB and MB solutions, respectively. The final mixture should have 2 mM CTAB and 18 mg/mL MB, respectively. Afterwards, this aqueous mixture was introduced to the liquid crystal to have 2.5v.% water-in-LC emulsion. The water microdroplets in the emulsion were prepared as follows. Firstly, the emulsion was vortexed at 3000 RPM for 1 min. After the vortex, the emulsion was ultrasonicated for 10 min. Lastly, it was vortexed at 3000 RPM for 1 min. before it was introduced to the experimental setup.

### 3.11 Particle tracking at LC/Aqueous interface experimental setup

In a typical experimental setup, we placed a 20  $\mu\text{m}$  thick TEM grid on a surface modified glass substrate as shown in **Figure 3.3-a**. The liquid crystals had different surface anchoring depending on the surface modification of the glass substrate. In our experiments, we used DMOAP for homeotropic surface anchoring and PI for planar surface anchoring. The TEM grid was filled with LC. In order to achieve a flat surface, the excess amount of LC was taken from the TEM grid via 1  $\mu\text{L}$  microcapillary until a black appearance was achieved under the cross-polarized microscopy under air exposure. A few hundred  $\mu\text{m}$  thick PDMS film was put around the LC-filled TEM grid on the surface modified glass substrate as shown in **Figure 3.3-b**. The aqueous media was introduced on the LC-filled TEM grid carefully without disturbing the LC filling until PDMS mould borders, **Figure 3.3-c**. After that, the aqueous solution of AuCr@TiO<sub>2</sub> JPs directly dropped onto the TEM grid. The aqueous media might contain salt depending on the designed experiment. When the salt was present to eliminate the electrical double layer, after the sedimentation of particles, the salt solution was replaced with a pure aqueous environment via micropumps for at least three volumes of the experimental setup. When the experimental setup was constructed, a cover glass was put onto the sample to have a better view under polarized optical microscopy for recording purposes, as shown in **Figure 3.3-d**.

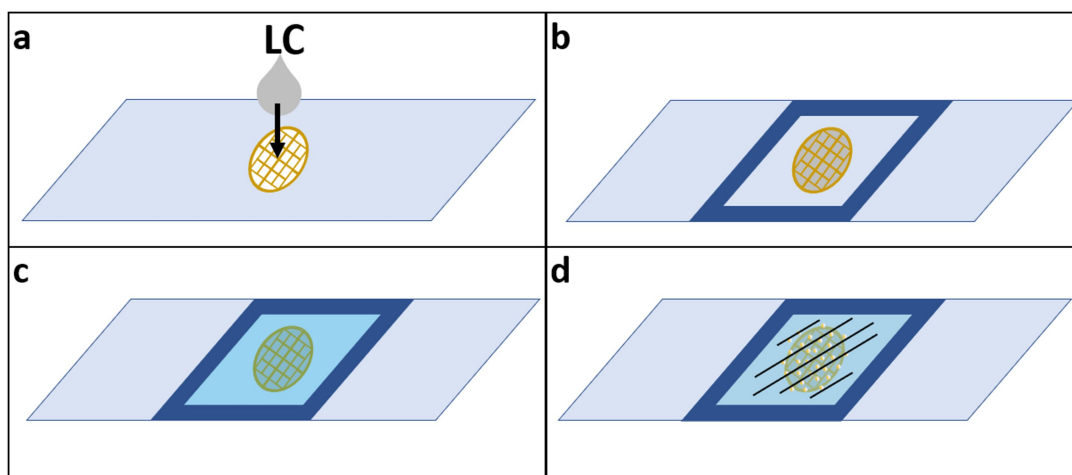


Figure 3.3: Particle tracking at LC/Aqueous interface sample preparation. a) LC filling of TEM grid. b) Complete filling of TEM grid and PDMS mould placing

### 3.12 Preparation samples for microcargo release experiments

The samples for the microcargo release through interfacial shear experiment were prepared as follows. A PDMS mould was placed at the bottom of a UV-Vis cuvette. Rest of the cuvette was filled with 3 mL 0.3 M NaCl aqueous solution as shown in **Figure 3.4-a**. Depending on the experiment, the paramagnetic particle concentration in the aqueous solution might differ from 10,000 particles/mm<sup>2</sup> to 40,000 particles/mm<sup>2</sup>. Subsequently, approximately 20  $\mu$ L 2.5v.% water-in-LC emulsion was introduced into the PDMS well via micropipette, **Figure 3.4-b**. The particles in the aqueous solution above the water-in-LC emulsion were force sedimented by a neodymium magnet while its magnetic poles were parallel to the LC/Aqueous interface, **Figure 3.4-c,-d**. After 30 minutes, the NaCl content and the small amount of released mass from the water-in-LC emulsion were cleaned via cross-flow micropumping, **Figure 3.4-e**. The UP water was introduced to the system from well above the LC/Aqueous interface while the intake was near the LC/Aqueous interface. In order to not disturb the LC/Aqueous interface, the flowrate of the cross-flow micropumping was set around 200  $\mu$ L/min. The micropumping was continued for at least three volumes of the initial aqueous solution volume. When the UV-Vis reading of the sample was equal to the initial reference state, the sample was closed, and the experiment was started, **Figure 3.4-f**.

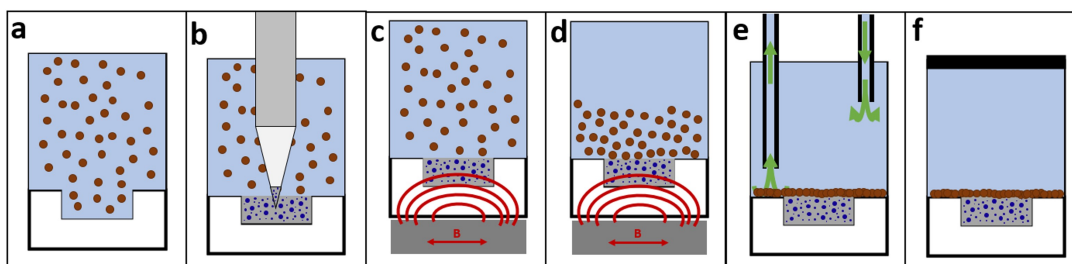


Figure 3.4: Sample preparation steps for microcargo release through interfacial shear experiments. a) PDMS well is at the bottom of UV-Vis cuvette and the cuvette is filled with aqueous media. b) Water-in-LC emulsion is introduced to the PDMS well via micropipette. c) Force sedimentation of paramagnetic particles via neodymium magnet, magnet is positioned below the sample having the poles parallel to the interface. Dark Red curves indicate the magnetic flux. d) Force sedimentation after a time interval. e) The cleaning of the aqueous media from salt and/or released microcargo in part b via cross-flow micropumping. f) The sealed sample ready for microcargo release.

### 3.13 Measurements of UV-Vis absorbance for microcargo release

In order to determine the rate of microcargo release, we used methylene blue (MB), rose bengal (RB) and natural red (NR) as microcargo since they have distinct absorbance peaks at 664 nm [86], 546 nm [87] and 504 nm in water, respectively. We constructed a calibration curve for each dye at different concentrations of aqueous solutions with respect to 664 nm, 546 nm and 504 nm absorbance values. We used these calibration curves to calculate the amount of released mass to the aqueous domain in our experiments. In each experiment, the reference state was taken as the pure aqueous environment before release.

## CHAPTER 4

### RESULTS & DISCUSSION

#### 4.1 Release studies with self-propelled Au@TiO<sub>2</sub> Janus particles

Kim et al. reported that in order to change the nematic director orientation at the interface for  $1 \text{ Nm}^{-2}$  interfacial shear,  $10 \text{ }\mu\text{m/s}$  directed velocity was sufficient [2]. In our first system, we planned to use active Au@TiO<sub>2</sub> Janus particles to generate mechanical shear on LC/Aqueous interface. When exposed to UV light, a chemical reaction takes place on the surface of these Janus particles. The chemical reaction uses the H<sub>2</sub>O<sub>2</sub> in the aqueous phase as fuel and produces a H<sup>+</sup> chemical gradient between the hemispheres of the Janus Particle. Therefore, these particles can make directed diffusiophoretic motion on the LC/Aqueous interface and hence may change the nematic director of liquid crystals on their path shown in **Figure 4.1**.

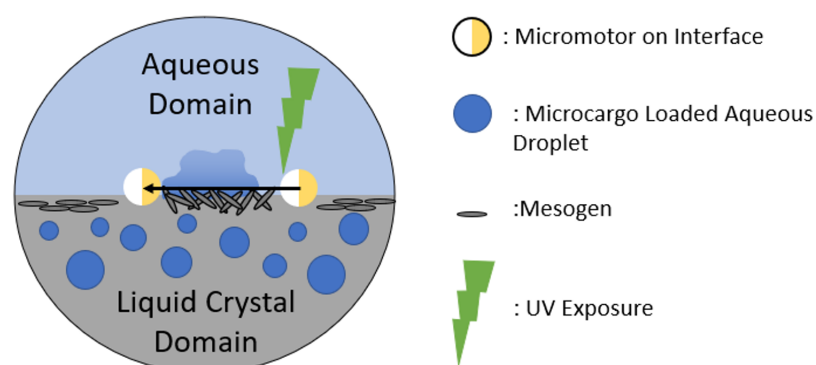


Figure 4.1: Sketch of liquid crystal based microcargo release method replacing motile bacteria with micromotor (active microparticle)

In order to understand the release mechanism of our designed system, we wanted to understand the forces acting on the microcargo-loaded droplets. When we can un-

derstand the forces, we can reveal release mechanism steps. Therefore, we calculated each force acting on these microcargio droplets while in liquid crystal domain near interface as shown in **Figure 4.2** where electric double layer and buoyancy forces acting in favour of release in +z-direction whereas the elastic repulsion force opposes in -z-direction. The cetrimonium bromide (CTAB) molecules on the aqueous methylene blue (MB) carrying droplet were overdrawn to emphasize the homeotropic anchoring. The h is defined as the distance from the interface in the LC domain.

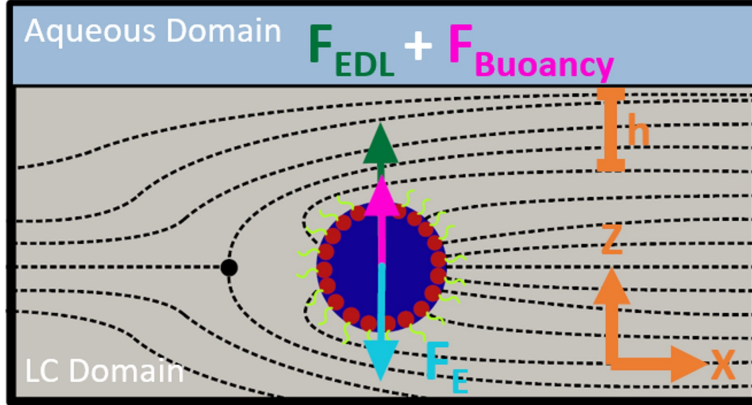


Figure 4.2: Schematic of three forces acting on the aqueous droplet near the LC/Aqueous interface.

In our original system, the LC/Aqueous interface was charged negatively. Besides the interface, the microcargio-loaded droplets contain CTAB, a positively charged surfactant. Therefore, the electric double layer at the interface should attract the microcargio holding droplets to itself. However, as the microdroplets approach to the interface, the elastic repulsion force was also increasing, which tends to force the droplets to remain in LC domain. Moreover, since E7 or 5CB LCs are denser than water,  $\rho_{5CB} = 1.010 \text{ g/cm}^{-1}$  [88], and  $\rho_{E7} = 1.057 \text{ g/cm}^{-1}$  [2], buoyancy force,  $\mathbf{F}_B$ , will act besides electric double layer force opposing elastic repulsion force. The elastic repulsion force,  $\mathbf{F}_E$  [89];

$$F_E \approx \pm A^2 B \pi K (R / (h + R)) \quad (4.1)$$

where  $A = 2.04$  for microdroplets whose radius,  $R$ , is greater than  $K/W$  with homeotropic anchoring [89]. For our case we take  $R$  as 1, 2.5, 5  $\mu\text{m}$  and  $K$  and  $W$  values are  $K_{E7}$

= 14.4 pN [90] and  $W \approx 1 \cdot 10^{-6} \text{ Jm}^{-1}$  [91], where  $B = 3/4$  and  $B = 1/2$  for planar and homeotropic anchoring respectively, at the boundaries of nematic LCs [18]. Lastly,  $h$  is the distance between aqueous microcargo droplet and LC/Aqueous interface.

The electric double layer force,  $\mathbf{F}_{EDL}$  can be expressed as [92];

$$F_{EDL} = -4\pi\varepsilon_{E7}\varepsilon_0 R\kappa(k_B T/e)^2 Y_p Y_i e^{-h\kappa} \quad (4.2)$$

where  $\varepsilon_{E7}$  and  $\varepsilon_0$  are the relative electric permittivity of E7 and electric permittivity of vacuum, respectively.  $R$ ,  $\kappa$ ,  $e$ ,  $k_B$  and  $T$  are the radius of microdroplets, Debye-Hückel parameter, elementary electric charge, Boltzmann constant and absolute temperature, respectively. The values for  $Y_p$  and  $Y_i$  can be calculated from the following equations;

$$Y_p = \frac{8 \tanh(D\zeta_p e/k_B T)}{1 + \sqrt{1 - (2R\kappa + 1/(R\kappa + 1)^2) \tanh^2(D\zeta_p e/k_B T)}} \quad (4.3)$$

$$Y_i = 4 \tanh\left(D\zeta_i e/k_B T\right) \quad (4.4)$$

where  $D$  is a numerical factor has been chosen as 1 just as surface potential is equal to zeta potential. However, even if it is a false claim, it does not invalidate the equation for  $\mathbf{F}_{EDL}$  in the region of  $h \gg 1/\kappa$  which is valid for our calculation.  $\zeta_i$  and  $\zeta_p$  are the LC/Aqueous interface and microdroplet zeta potentials, respectively.

The buoyancy force,  $\mathbf{F}_B$  can be written as;

$$F_B = \frac{4}{3}\pi R^3 g(\rho_{E7} - \rho_{aq}) \quad (4.5)$$

Lastly the net force acting on the microcargo loaded aqueous droplets can be found as;

$$F_{net} = F_{EDL} + F_B - F_E \quad (4.6)$$

We performed a net force analysis acting on different sizes of microdroplets at different distances from LC/Aqueous interface. For our calculations, the distance  $h = 0$  is the LC/Aqueous interface and  $h > 0$  is in the water-in-LC emulsion. Droplets smaller than  $5.0 \mu\text{m}$  radius are in close proximity to the LC/Aqueous interface which are less than  $5 \mu\text{m}$  when  $\mathbf{F}_{Net} = 0$ . However, droplets greater than  $5.0 \mu\text{m}$  radius are far away from the LC/Aqueous interface as shown in **Figure 4.3**. As shown in **Figure 4.3**, we can also deduce that the time required to release the bigger droplets would be greater since a greater distance has to be covered before reaching the LC/Aqueous interface. It should be noted that  $\mathbf{F}_{net}$  calculation depends on the salt concentration of the media. The results in **Figure 4.3** are at  $0.01 \text{ mM}$  salt concentration. However, when we increase the salt concentration to  $1.0 \text{ mM}$ , since the  $\mathbf{F}_{EDL}$  is decreased by the increased salt concentration, the droplets whose radius are greater than  $1 \mu\text{m}$  would be far away from the interface as the  $\mathbf{F}_E$  dominates as compared to  $0.01 \text{ mM}$  case. Moreover, we can also observe that the droplets whose radius around  $0.1 \mu\text{m}$  cannot be contained below the LC/Aqueous interface since  $\mathbf{F}_{Net} > 0$ . Therefore, the presence of salt in the aqueous medium would drastically decrease the release rate of the aqueous droplets in the LC domain. The results for  $1.0 \text{ mM}$  salt concentrated case are shown in **Appendix A**.

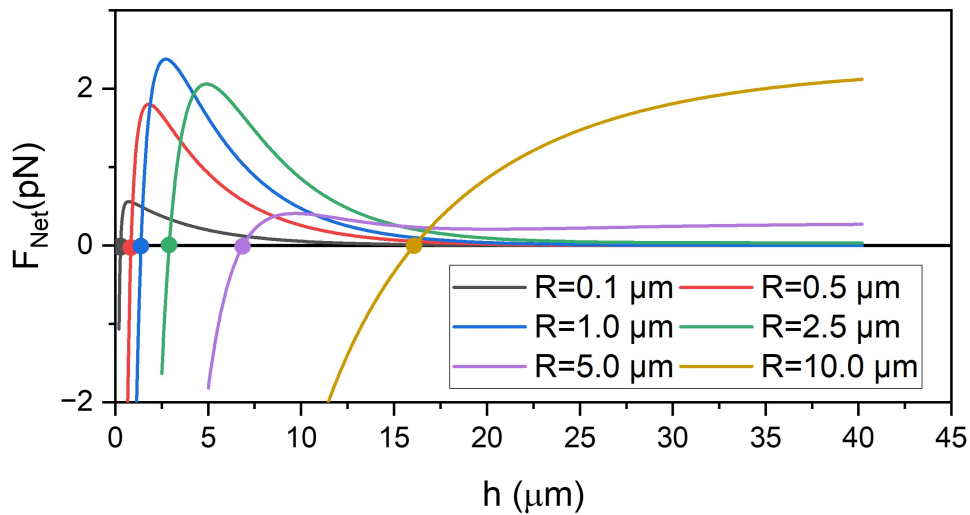


Figure 4.3: Net force acting on different sizes of microdroplets at various distances. NaCl salt concentration is set to  $0.01 \text{ mM}$  for calculation purposes.  $R$  represents the radius of water droplet carrying microcargo while  $h$  represent the distance to the interface.

In order to determine the crystal structure of the synthesized microparticles, we have carried out a phase analysis with X-ray diffraction. The XRD analysis of the calcinated microparticles showed strong diffraction peaks of 101, 121, 103, 004, 112, 200, 105, 211 and 204 planes at  $2\theta = 25.3^\circ, 30.9^\circ, 37.0^\circ, 38.0^\circ, 39.0^\circ, 48.1^\circ, 54.4^\circ, 55.1^\circ$  and  $63.1^\circ$  respectively as shown in **Figure 4.4**. The XRD results were consistent with the literature for anatase (ICDD 21-1272)  $\text{TiO}_2$  crystal structure [93] especially since we have two distinct peaks at  $25.3^\circ$  and  $48.1^\circ$  which are the indicative peaks for anatase crystal structure. We also observed one additional peak around  $30.9^\circ$  that might indicate an additional brookite phase [94]. Even though the existence of the brookite phase (ICDD 21-1360) might impact our design, since our particles have strong peaks for anatase phase we continued to use these microparticles in our experiments. We also noticed that there was broadening in our XRD analysis of the  $\text{TiO}_2$  samples which may indicate that existence of polymorphic structure in our synthesis. However, since we have observed activation in our  $\text{AuCr@TiO}_2$  Janus particles, we deduced that we have the crystal structure at the outer radius of the Janus particles which is required for the anisotropic motion of these particles.

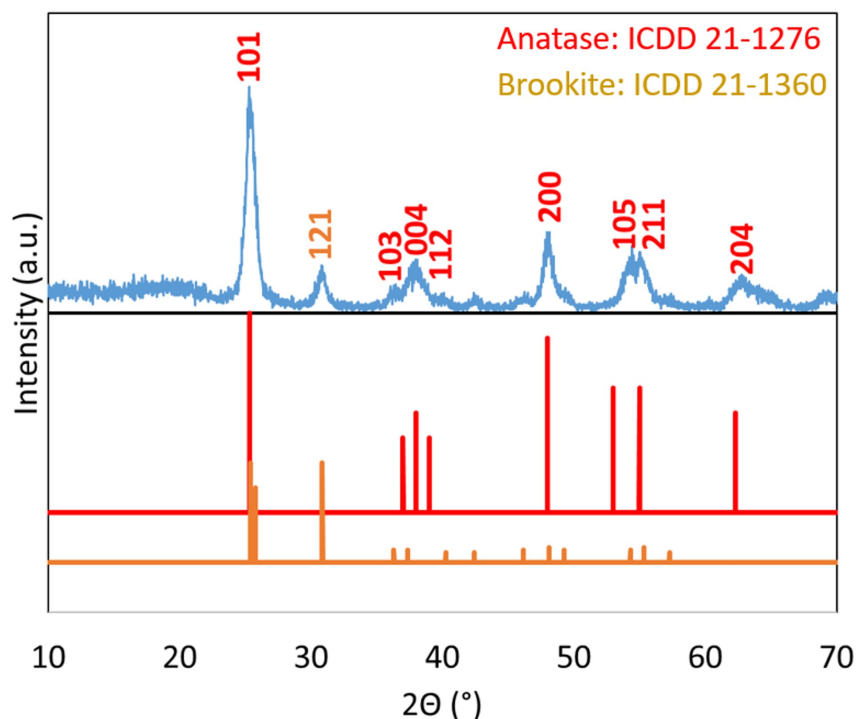


Figure 4.4: XRD Spectrum of  $\text{TiO}_2$  Microparticles

The characterisations of shape and diameter of the synthesis are crucial for our design. In our design, the spherical particles are required to be big enough to generate mechanical shear on the LC/aqueous interface. Therefore, in order to determine the average diameter and the shape of the synthesis, we have taken the scanning electron microscopy (SEM) images of the synthesised samples. As shown in **Figure 4.5-a**, we observed that the particles mostly have smooth surface & sphere-like round shapes. In addition to our observation, we have conducted an image processing analysis for the average diameter of the particles. For 375 separate particles, we found out that the average diameter of the microparticles was  $1.010 \pm 0.141 \mu\text{m}$ , **Figure 4.5-b** ranging from  $0.5 \mu\text{m}$  to  $1.5 \mu\text{m}$ , **Figure 4.5-c**. The Escherichia coli (E.Coli) bacteria in the study of Kim et al. [2] typically have sizes of  $1.0\text{-}2.0 \mu\text{m}$  in length and  $0.5 \mu\text{m}$  in diameter respectively [95]. Therefore, we concluded that the particles are big enough to generate mechanical shear.

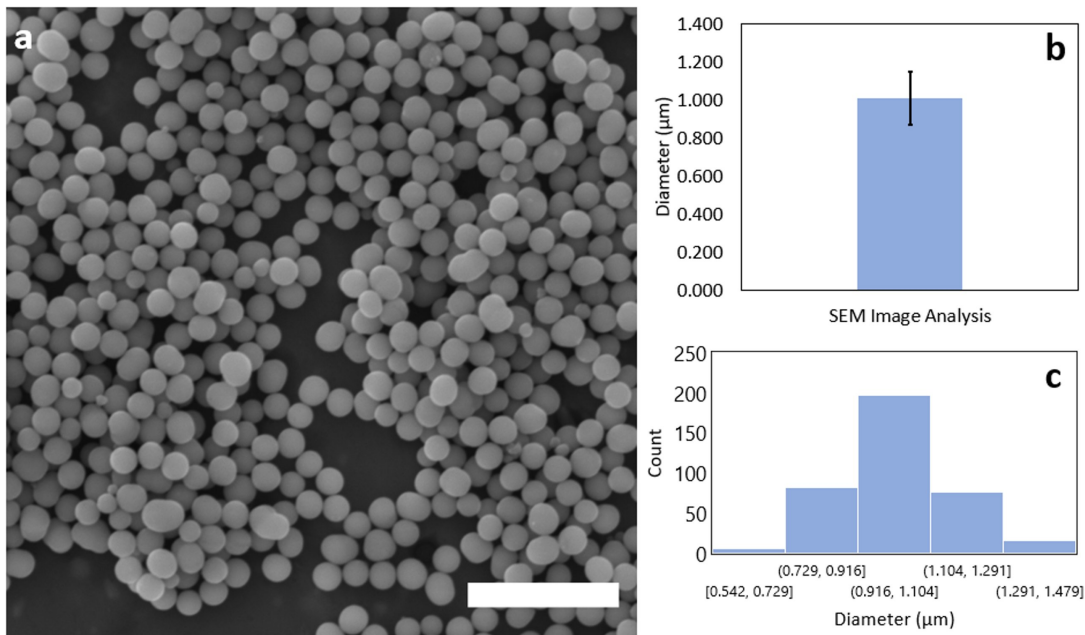


Figure 4.5: TiO<sub>2</sub> core particle characterisation. a) SEM images of anatase TiO<sub>2</sub>, 5 μm scale bar. b) SEM image processing result for average diameter of TiO<sub>2</sub> particles. c) histogram for TiO<sub>2</sub> particle diameter.

The anisotropic character of the particles was achieved with half-coating of the TiO<sub>2</sub> microparticles with Au cap. We have performed the coating of Au with two methods. In the first approach, we coated the particles with Au via directional ion-sputtering

with Pd support. Since the amount of Au on the TiO<sub>2</sub> microparticle affects the photocatalytic efficiency, we have chosen the Pd supported Au cap thickness as approximately 30 nm, 1-2 wt.% to have the maximum efficiency. [81]. The SEM images in the **Figure 4.6-a**, with backscattering mode on the right, of AuPd@TiO<sub>2</sub> Janus particles revealed that the directional coating of Au cap is achieved. A secondary image is shown in **Figure 4.6-b**, also reveals the two distinct hemispheres of an AuPd@TiO<sub>2</sub> Janus particle, where TiO<sub>2</sub> is shown as dark grey, and Au is shown as light grey.

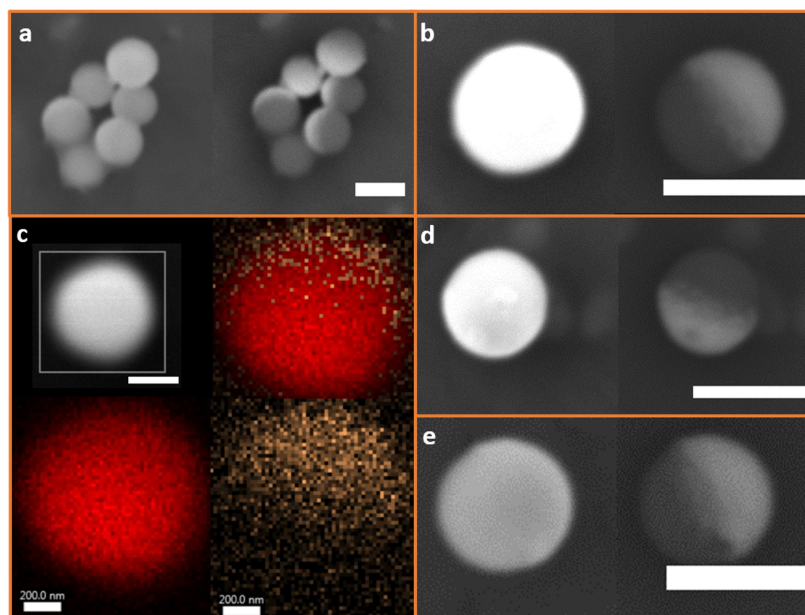


Figure 4.6: AuPd@TiO<sub>2</sub> Janus particles – a) AuPd@TiO<sub>2</sub> Particle Cluster b) Single AuPd@TiO<sub>2</sub> Particle - SEM image with backscatter mode (right) respectively. c) EDX analysis of a single AuCr@TiO<sub>2</sub> Janus particle. Red is for Ti and light brown is for Au respectively. d-e) Single AuCr@TiO<sub>2</sub> Janus Particle, Left – SEM image, Right – Backscatter mode. Scale bars are 1  $\mu$ m for particles and 200 nm for coloured EDX analyses.

Even though we have fabricated Janus particles, we observed that the activity of AuPd@TiO<sub>2</sub> Janus particles decreased over time even with the presence of higher concentration of H<sub>2</sub>O<sub>2</sub> fuel concentration. We suspected that the ultrasonication step for dispersion before each activation experiment might result in the loss of some part of the Au cap on the microparticles, resulting in low anisotropic activity under UV illumination. In order to resolve this issue, we have decided to apply an interlayer of Cr base before Au coating. In addition, we have also changed the coating process

since the Au@TiO<sub>2</sub> photocatalytic activity strongly depends on the coating method of Au on the TiO<sub>2</sub> surface [82]. We have chosen thermal coating for Janus particle functionalisation for the new coating method. The EDX analysis of AuCr@TiO<sub>2</sub> shown in **Figure 4.6-c** revealed that the TiO<sub>2</sub> core, coloured with red, was half-coated with Au, coloured with light brown. In addition to EDX results, the SEM images also support directional coating of Au as shown in **Figure 4.6-d,-e**. We did not observe a significant decrease in the activation of the particles due to the deformation of the AuCr@TiO<sub>2</sub> Janus particles during our experiments.

Particle tracking is a crucial step in the quantitative analysis of real-time-lapse microscopy image data. Since manual localizing and tracing of each “particle” is an inefficient way of interpreting data, and generally large number of independent measurements should be taken to be consistent statistically for each experiment, automated computational methods have been developed for these “systems” by many groups [96] [97] [98] [99]. Unfortunately, no “one fit for all” method is known for particle tracking method since each system may differ significantly and have different requirements for stable, robust, and reliable data analysis [100]. We used a java-based platform (FiJi) with an integrated plugin called “Trackmate” [85] to interpret the trajectories of our microparticles. We have performed 2D single microparticle trajectory analyses with a rule of thumb; each particle must be far from one another, at least 20 body lengths, to eliminate the interaction between the particles.

To justify our equipment’s capability, we first measured the Brownian (passive) motion of 1 μm average diameter SiO<sub>2</sub> microparticles in various media. The 2D random motion of a SiO<sub>2</sub> microparticle is shown in **Figure 4.7-a**. We have tracked at least 120 different particles for each media, which were Newtonian fluids, and real time-lapse vs. position data of each particle was analysed with a custom MATLAB code for mean square displacement (MSD) [101]. We have deduced the viscosity information of the media via the Stokes-Einstein relationship for the Brownian motion of the particles,  $D = (k_B T) / (3 \pi \mu_{app} D_P)$ . Where  $D$  is the diffusion coefficient of the particle,  $k_B$  is the Boltzmann constant,  $T$  is the medium absolute temperature,  $\mu_{app}$  is the apparent viscosity of the media around the particle, and  $D_P$  is the particle diameter, respectively. To get the diffusion coefficient of the particle, we have used the following relation:  $MSD = nD\Delta t$ , in which MSD is for mean squared displacement,

n is the dimension number of the analysis, D is the diffusion coefficient of the particle, and  $\Delta t$  is the observation time scale for the analysis, respectively. The mean squared displacement is defined as  $\text{MSD} = \langle |x - x_0|^2 \rangle$  where x is the position of the particle at time t and  $x_0$  is the reference position at t- $\Delta t$ . We have decided that the microparticles undergo a Brownian motion by analysing the MSD with respect to  $\Delta t$ . The MSD of the particle shown in **Figure 4.7-a** analysed with respect to  $\Delta t$  revealing the linear relationship for Brownian motion in **Figure 4.7-b**. We have calculated the apparent viscosities around SiO<sub>2</sub> microparticles and compared them with their true values as shown in **Figure 4.7-c**. We have found that we could attain the viscosity information with an error range between 5% to 15% for isotropic Newtonian fluids. There are couple of possible reasons for the relative error in our calculations. The first and probably main reason is the digitalisation of the particle's position. When we assume the number of position data is constant and the pixel size is smaller than the average displacement of the particle, the accuracy of the calculations for the viscosity increases. On the other hand, for the same calculation, when the pixel size is comparable to or greater than the particle's average displacement, the viscosity calculation accuracy decreases due to the pixel binning process and more data points are required for greater accuracy. We also analysed the MSD of x and y directions separately to reveal the isotropic characteristic of the analysed Newtonian fluids. The **Figure 4.7-d** shows the ratio of x and y direction MSD data being around 1.0, which is the indication of isotropic media.

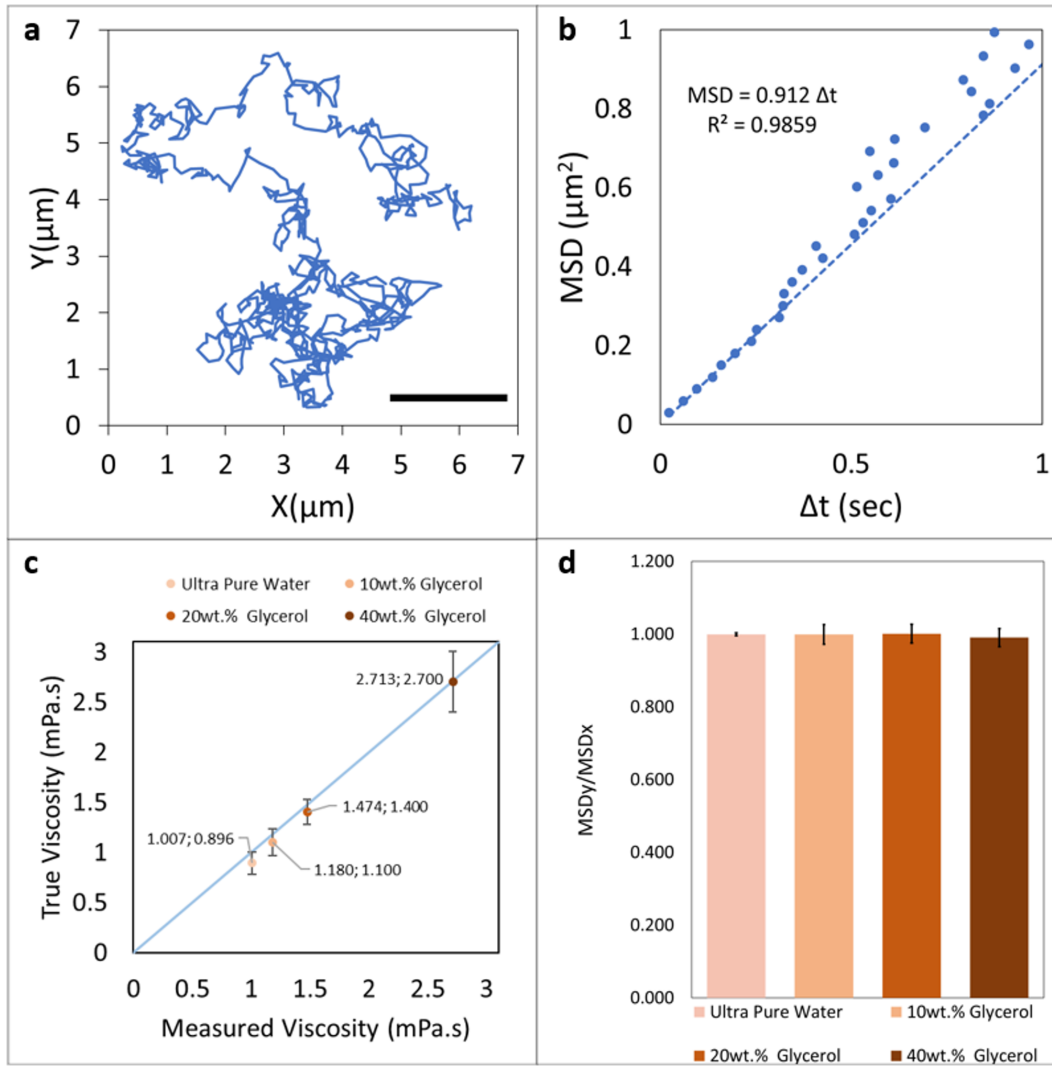


Figure 4.7: a) Brownian Motion Trajectory of a SiO<sub>2</sub> Particle. 2 μm scale bar. b) The mean square displacement (MSD) of the same particle over time. c) Viscosity measurements of different Newtonian fluids with respect to their true viscosities. d) Mean square displacement ratios of perpendicular dimensions indicating the isotropic motion.

The active propulsion of the microparticles can be explained with the **Equation 4.7** given below. On the right side, the first part of the equation holds for the Brownian motion of the particle while the second part gives information about the active propulsion [101]. In **Equation 4.7**, the  $t_R$  is the rotational diffusion constant such that  $t_R^{-1} = (k_B T) / (8\pi \mu_{app} R_P^3)$ . Where  $\Delta t$  is the observation time interval and  $V$  is the active propulsion velocity. The equation can represent 2D motion of a particle, and

it has two limiting forms. When  $\Delta t \ll t_R$ , the equation becomes  $MSD = 4D\Delta t + V^2 \Delta t^2$  and when  $\Delta t \gg t_R$ ,  $MSD = (4D + V^2 t_R) \Delta t$ . When a particle is moving in a media with known viscosity, one can make the MSD analysis in the sufficiently small  $\Delta t$  region such that the  $\Delta t \ll t_R$  condition holds for each  $\Delta t$  and hence the need of  $t_R$  information can be resolved. We have recorded the passive and active trajectories of our Au capped  $TiO_2$  Janus particles both under visible light and UV illumination with  $H_2O_2$  presence in the media we were analysing. When we compare the particle trajectories at the same time interval from **Figure 4.8-a**, for the same Au capped Janus particle, the passive motion under visible light (orange) has shorter trajectory whereas the active propulsion under UV illumination has longer trajectory (turquoise), meaning a greater distance covered in the same time interval in active propulsion.

$$MSD = 4D\Delta t + (V^2 t_R^2 / 2) ((2\Delta t / t_R) + e^{(-2\Delta t / t_R)} - 1) \quad (4.7)$$

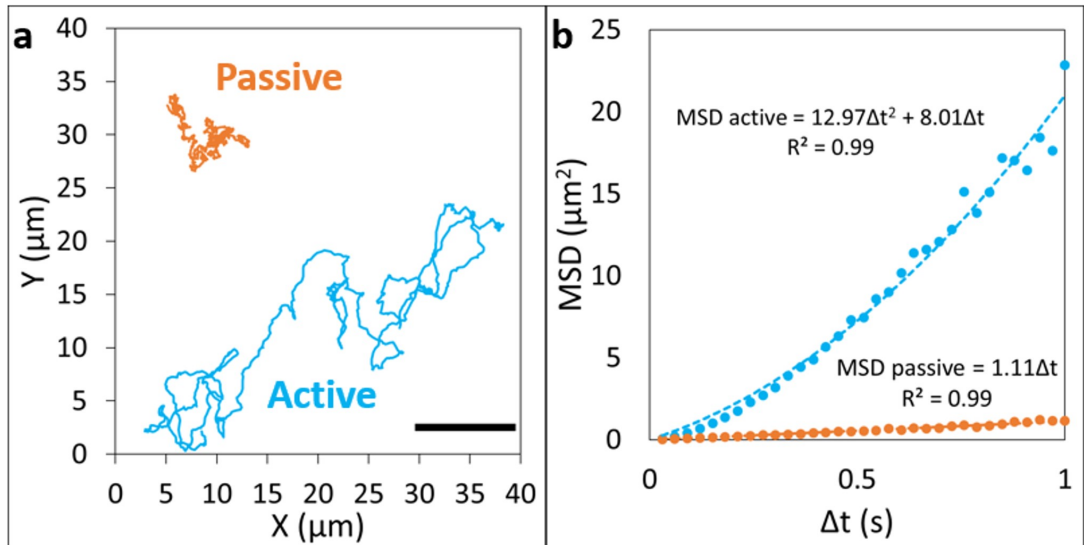


Figure 4.8: a) Particle trajectory over the same time interval, Brownian and active motion of the same  $AuCr@TiO_2$  Janus particle, scale bar is  $10 \mu m$ . b) The MSD vs  $\Delta t$  analysis of the Brownian and active motion of the same particle.

We have analysed the MSD of each particle's trajectories under visible and UV light exposure to classify the motions as active propulsion or passive motion. For example, for a  $AuCr@TiO_2$  Janus Particle with  $1 \mu m$  diameter, in  $1 \text{ mPa}\cdot\text{s}$  viscosity media

at 298.15 K, the rotational diffusion time is,  $t_R = 763$  ms. In **Figure 4.8-b**, it is shown that the MSD vs  $\Delta t$  of a particle has these conditions. We have observed that, when the  $\Delta t$  value is sufficiently smaller than  $t_R$ , the equation  $\text{MSD} = (4D + V^2 t_R) \Delta t$  fits MSD vs  $\Delta t$  data with  $R^2$  up to 0.99. From **Figure 4.8-b**, active propulsion data, we could also deduce that as the  $\Delta t \approx t_R$ , the condition  $\Delta t \ll t_R$  loses its validity and the calculation starts to lose accuracy since rotational diffusion leads to a randomisation of the direction of the propulsion and the particle goes under random walk [101]. For Brownian motion, the equation  $\text{MSD} = 4D\Delta t$  fits the data with  $R^2$  up to 0.99.

We have calculated the velocities of each active Janus particle under different  $\text{H}_2\text{O}_2$  concentrations from MSD vs  $\Delta t$  data to find the effect of fuel concentration on active propulsion. We have set the maximum  $\text{H}_2\text{O}_2$  concentration to 5wt.% since the anisotropic motion of Janus particles increases drastically after 5wt.% concentration so that the Janus particles exit out of focus of our microscopy due to 3D movement in the constructed cell. This 3D movement results in difficulty in interpretation of the particle position data and the 2D analysis may be misleading. We deduced that, from **Figure 4.9**, as the  $\text{H}_2\text{O}_2$  fuel concentration increases, the particles move with increased velocities under UV illumination. Besides that, we have also observed that some particles could exit from the focus plane and re-enter due to 3D active propulsion under UV illumination.

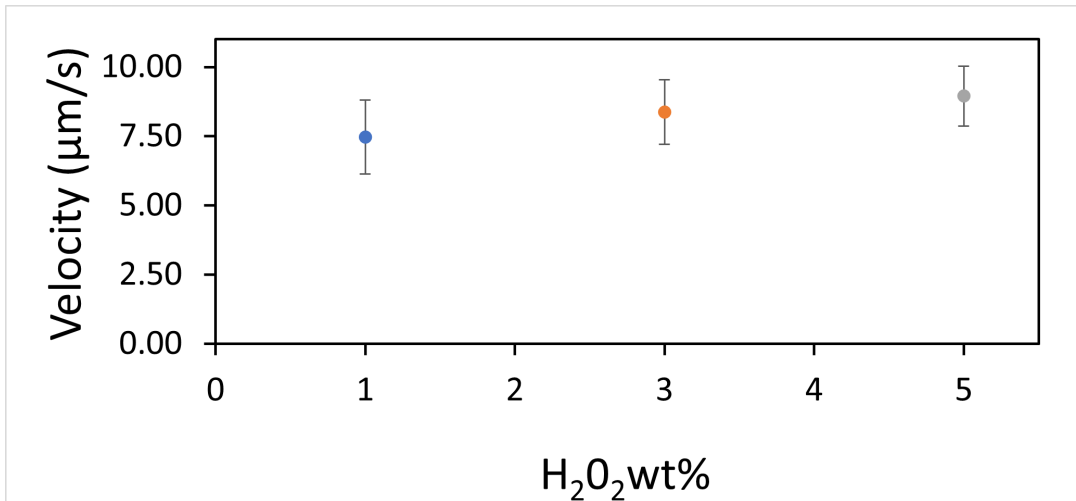


Figure 4.9: Velocities of AuCr@TiO<sub>2</sub> Janus particles under different fuel concentrations.

In our trajectory recordings, we have observed some particles exiting and entering the microscope's focal plane. In order to have such a movement, we calculated the maximum achievable velocity to overcome the drag and gravitational force, both of which acts in the negative z-direction with respect to **Figure 4.10**. The calculation details are shown in **Appendix B.1**. We can observe the microscopy images of a single AuCr@TiO<sub>2</sub> Janus Particle from **Figure 4.10-a-d**. Moreover, we deduced that as the particle exits the focus plane, the microscopy image becomes blurred, **Figure 4.10-b,-c**. We have calculated the minimum required velocity as 2.42  $\mu\text{m/s}$  for 1  $\mu\text{m}$  AuCr@TiO<sub>2</sub> Janus particles to be able to suspend in the aqueous media. The minimum velocity calculation is shown in **Appendix B.2**. When we inspect the Janus particles undergoing out-of-focus motion, we revealed that as the particles start to exit from the focus plane or as they reenter it, each particle has greater velocity to overcome the gravitational and drag force. However, when a particle moves in the z-direction only, the particle's velocities in the xy plane could be zero. This type of motion could increase our calculations' error since the particle undergoes 3D motion. Therefore, we did not include these particles in our average velocity calculations even though having great velocities up to 20  $\mu\text{m/s}$ .

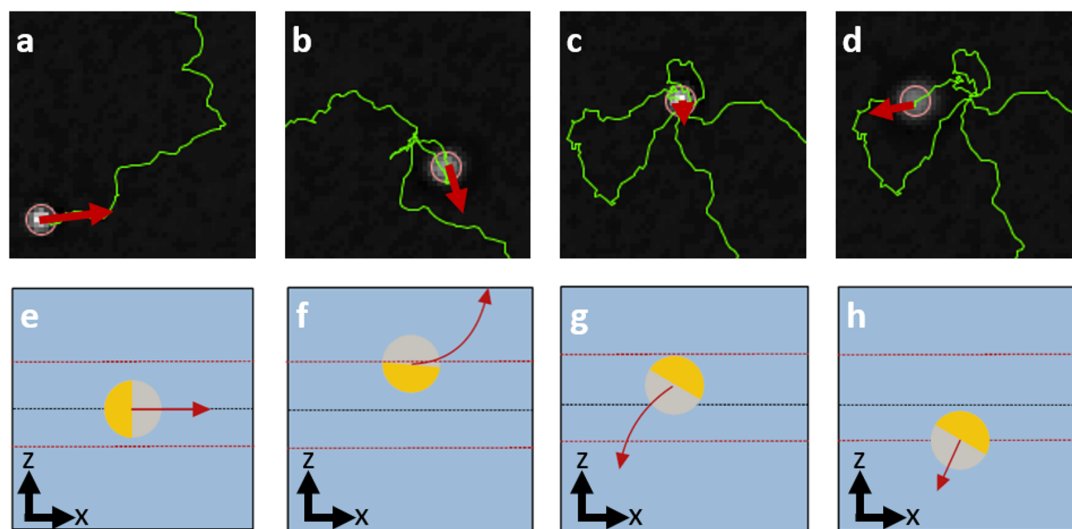


Figure 4.10: a-d) Microscopy images of a AuCr@TiO<sub>2</sub> Janus Particle having 3D motion. b,c) Exiting from and re-entering to focus plane respectively. e-f) Out of focus motion sketch of the same micrographs. Red dashed lines represent the focus plane thickness of the microscopy.

The reactions on AuCr@TiO<sub>2</sub> Janus particles are strongly coupled with the ionic concentration of the environment. In order to investigate this coupling effect, we have analyzed the activation velocities of the same batch of Janus particles at the same H<sub>2</sub>O<sub>2</sub> fuel concentration, 3 wt.%, within different ionic concentrated environments, **Figure 4.11**. We have observed that the activation and hence the active velocities of the particles were decreasing with increasing salt concentration from zero salt, ultrapure (UP) water, to 1 mM NaCl. We can also observe from **Figure 4.11** that the average velocities of the Janus particles were greater than 10  $\mu\text{m/s}$  with a wide standard deviation about approximately 4  $\mu\text{m/s}$  in a medium free of salt. The particles having greater velocity above 10  $\mu\text{m/s}$  are expected to provide sufficient energy to generate mechanical shear when they are located on LC/Aqueous interface, which is a good starting point for our designed system. We concluded that, even though the particle sedimentation would be easier with salt concentration (more information will be given in zeta potential measurements section) the system must be cleansed from any salt existence in order to increase the degree of activation as much as possible at the LC/Aqueous interface. Moreover, we observed that even with 0.1 mM NaCl salt concentration, the degree of activation would be insufficient for generating mechanical shear stress at the interface since the average velocities of these Janus particles were less than 10  $\mu\text{m/s}$ . Furthermore, we have concluded that the activation of the particles ceased around 1 mM NaCl solution since the average velocities of the particles were almost equal to the passive (Brownian) motion of the particles. In the light of these results, we have decided to use pure water media in order to activate Janus particles as much as possible in our design.

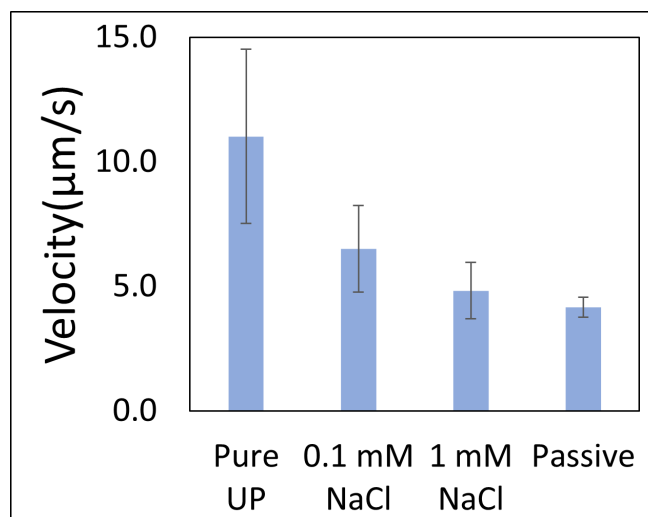


Figure 4.11: Active velocities of AuCr@TiO<sub>2</sub> JPs at different NaCl concentrations

After synthesizing TiO<sub>2</sub> core, modifying them with Au cap to have AuCr@TiO<sub>2</sub> Janus particles and characterizing the activation of these particles, we planned to sediment the Janus particles onto the LC/Aqueous interface with natural sedimentation from the aqueous phase. However, after equilibrating for 1 hour, which was sufficient enough to sediment a 1 μm diameter AuCr@TiO<sub>2</sub> Janus particle, the particles over 5CB layer continued to undergo Brownian motion similar to in water media. We thought the particles might be levitating on the liquid crystal layer due to electrostatic repulsion. In order to prove our hypothesis, we recorded the passive Janus Particle motion. We analysed these recordings to reveal the apparent viscosities in x and y-directions around each particle, **Figure 4.12**. From **Figure 4.12** we speculated that these particles might be positioned above the liquid crystal/Aqueous interface since the calculated apparent viscosities around the particles were around 1.6 mPa.s to 26.8 mPa.s for most of the particles in both directions. These viscosity values were significantly smaller than the reported 5CB viscosity values [102] in the literature in terms of order of magnitude. We suspected that due to ionic repulsion, the particles might be levitating. Therefore, we measured zeta potential of the liquid crystal and AuCr@TiO<sub>2</sub> JPs in different salt concentrations to choose the appropriate salt concentration to eliminate the ionic repulsion between JPs and 5CB liquid crystal layer.

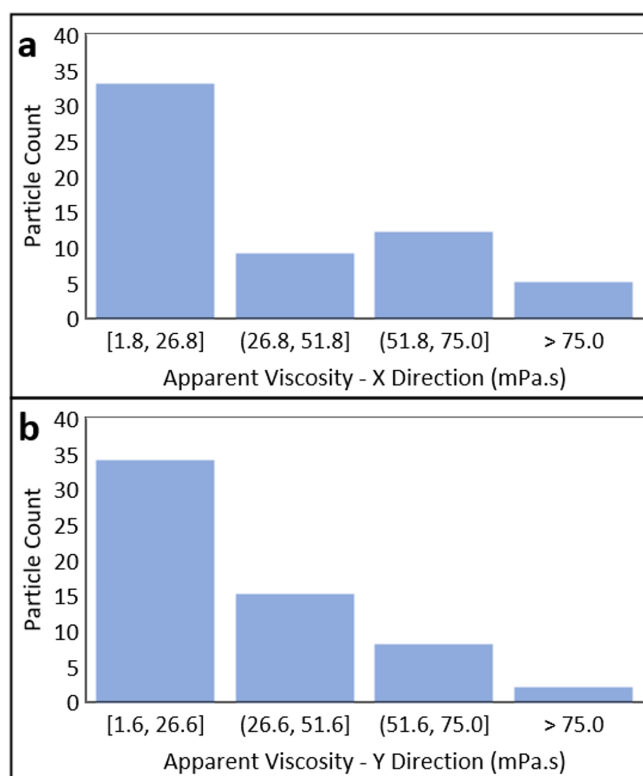


Figure 4.12: a) Apparent viscosity histogram around AuCr@TiO<sub>2</sub> JPs above LC/Aqueous interface in x-direction. b) Apparent viscosity histogram around AuCr@TiO<sub>2</sub> JPs above LC/Aqueous interface in y-direction

The zeta potentials of 5CB and AuCr@TiO<sub>2</sub> JPs are measured in 1-, 10-, 100-, and 300-mM salt concentrations, respectively. We have used NaCl for the reconstruction of ionic media. From **Figure 4.13** we observed that as the salt concentration increases the zeta potentials of 5CB and AuCr@TiO<sub>2</sub> changes from -73.1 mV to -15.1 mV and -47.4 mV to -0.109 mV respectively. Since the absolute zeta potentials for 5CB and AuCr@TiO<sub>2</sub> are the smallest at 300 mM, we have selected 300 mM NaCl concentration to sediment the Janus particles onto 5CB liquid crystal layer in our interface experiments.

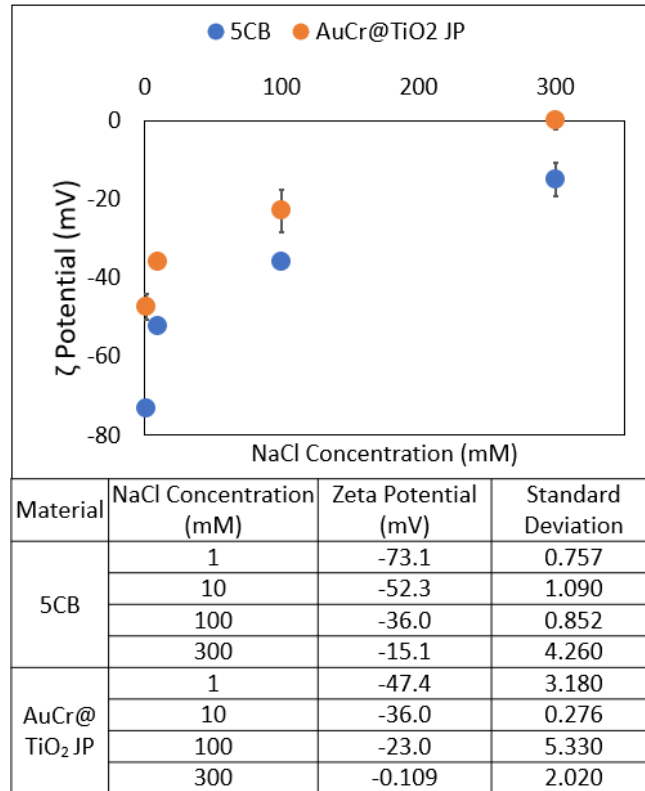


Figure 4.13: Zeta potential measurements for 5CB Liquid Crystal and AuCr@TiO<sub>2</sub> JPs in various NaCl concentrations

In order to observe the effect of NaCl on the natural sedimentation of AuCr@TiO<sub>2</sub> JPs at the LC/Aqueous interface, we have constructed the same experiment with two modifications. Firstly, the glass substrate had been coated with polyimide (PI), and it was scratched with a microfiber cloth in the x-direction. Polyimide provides the planar anchoring with 5CB liquid crystal. [103] The polyimide coated, and x-direction scratched base provides a uniform anisotropy at the LC/Aqueous interface as shown in **Figure 4.14-a**. This uniform anisotropy allows us to deduce the directed interaction between LC/Aqueous interface and AuCr@TiO<sub>2</sub> Janus particles when the particles are in contact with the liquid crystal plane, **Figure 4.14-b**. Secondly, before the activation experiment, we used 300 mM NaCl aqueous solution for natural sedimentation of the AuCr@TiO<sub>2</sub> Janus particles. As mentioned, this was done to eliminate the electrostatic repulsion effect between 5CB and AuCr@TiO<sub>2</sub> Janus particles at the interface.

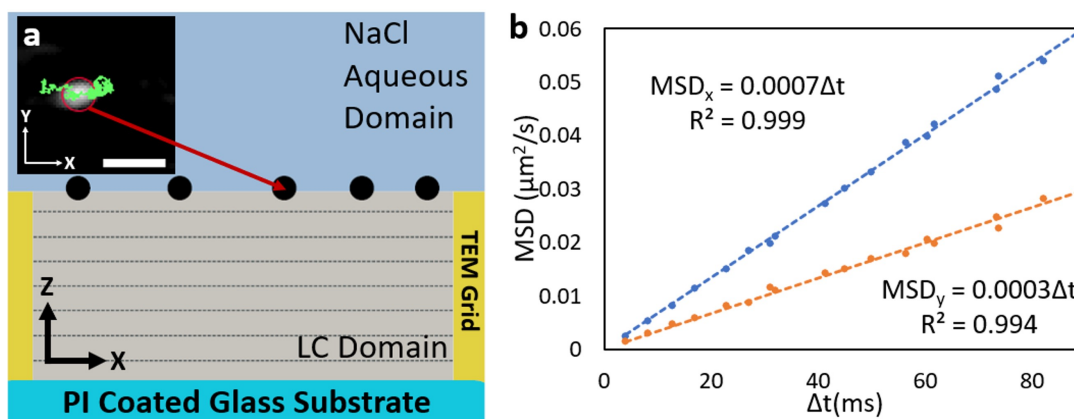


Figure 4.14: a) Schematic representation of designed system for the experiment with a passive motion trajectory of a AuCr@TiO<sub>2</sub> Janus Particle at LC/Aqueous interface, 4 μm scale bar. b) MSD analysis of the same particle in part a; indicating anisotropic interaction of the particle at the interface.

After equilibrating the system for 30 minutes, we observed that, when we recorded the passive particle motions, the particles covered less ground in the same time interval compared to the previous experiments. We analysed the passive JP trajectories to calculate apparent viscosities around the particles. We have observed that the average apparent viscosities increased compared to the previous case, **Figure 4.12**, for both x and y direction as shown in **Figure 4.15**. We also observed that due to the uniform anisotropy along the x-direction, the particles were able to move easily in the x-direction due to less resistance, **Figure 4.15-a**. On the other hand, in the y-direction, the same particles must move perpendicularly to the mesogens of 5CB that are oriented in the x-direction, and hence the calculated viscosity value increases, **Figure 4.15-b**. Therefore, we also deduced that from **Figure 4.14-b**, the anisotropic interaction of AuCr@TiO<sub>2</sub> particles at the interface also indicates that the JPs were actually in contact with 5CB. Therefore, we changed our procedure to first sediment AuCr@TiO<sub>2</sub> Janus particles with 0.3 M NaCl salt concentrated media, then cleanse the aqueous environment from NaCl salt before the activation experiment.

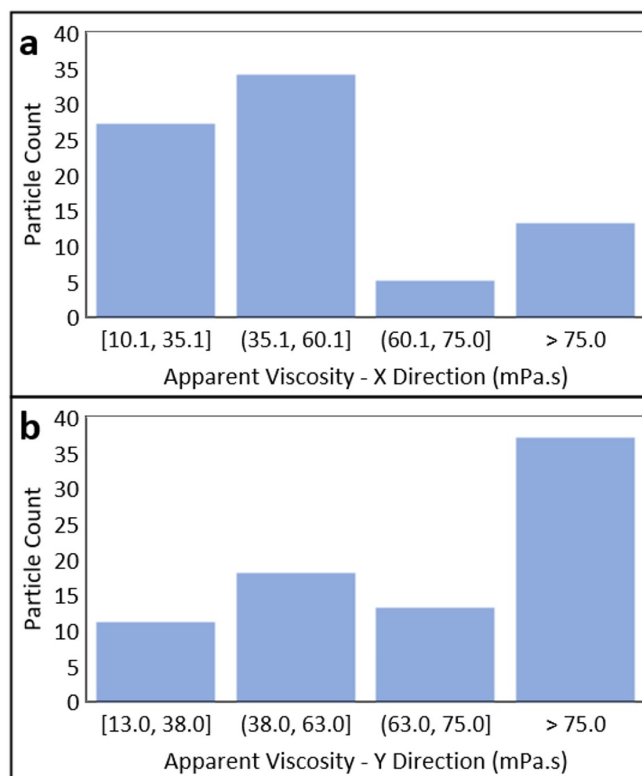


Figure 4.15: Apparent viscosity histograms around AuCr@TiO<sub>2</sub> JPs at LC/Aqueous interface in 300 mM NaCl aqueous solution. a) Along x-direction b) Along y-direction

We have constructed the same setup for activation of AuCr@TiO<sub>2</sub> JPs on LC/Aqueous interface under UV illumination. After sedimentation of AuCr@TiO<sub>2</sub> JPs, the NaCl in the aqueous solution was replaced with a salt-free aqueous solution via cross-flow micropumping for at least three system volumes before activation. The reason was that even though NaCl in the media helps the natural sedimentation, the Janus particles could not have an active motion in the presence of such salt concentration as shown in **Figure 4.11**. Furthermore, we wanted to regenerate the electric double layer between LC and the aqueous environment to its original state to see its possible effects of it. Since the 5CB was oriented along x-direction with PI coated glass substrate, we expected that the particles would have greater active motion along the x-direction. For the activation, we have set the fuel H<sub>2</sub>O<sub>2</sub> concentration to 5 wt.%.

We have observed 4 types of activation under UV illumination. Some particles were not activated since the MSD data shows a linear trendline as shown in **Figure 4.16-a**. These particles were classified as "passive". From **Figure 4.17** we observe that even though we had UV illumination on, these particles were not activated. The activation mechanism of these particles could explain the reason for that. In order to move anisotropically, these Janus particles should simultaneously have at least some of both hemispheres exposed to the aqueous environment. The passive state particles in **Figure 4.17** might have an interaction with LC such that one of the hemispheres fully embedded into LC layer and hence could not complete the activation steps for anisotropic motion. The activation condition was set to have a  $2^{nd}$  order polynomial relationship between MSD and  $\Delta t$ . Interestingly, some particles moved along y-direction as shown in **Figure 4.16-b**. We did not expect such movement since the LC layer had been oriented along the x-axis, and the LC layer must have greater viscosity along the y-axis; hence it must show greater resistance to the motion of the particles. Therefore, we thought these y-directed particles should lack interaction with the LC layer. These particles were classified as "y-directed". Some particles showed activation in both direction, **Figure 4.16-c**, and classified as "x- and y-directed". Lastly, some particles were activated along x-direction and classified as "x-directed" as shown in **Figure 4.16-d**. Regardless of the activation direction, we observed that the Janus particle velocities decreased around 1-3  $\mu\text{m/s}$ , which are almost 10 folds less compared to the previous activation results shown in **Figure 4.11** for pure water media.

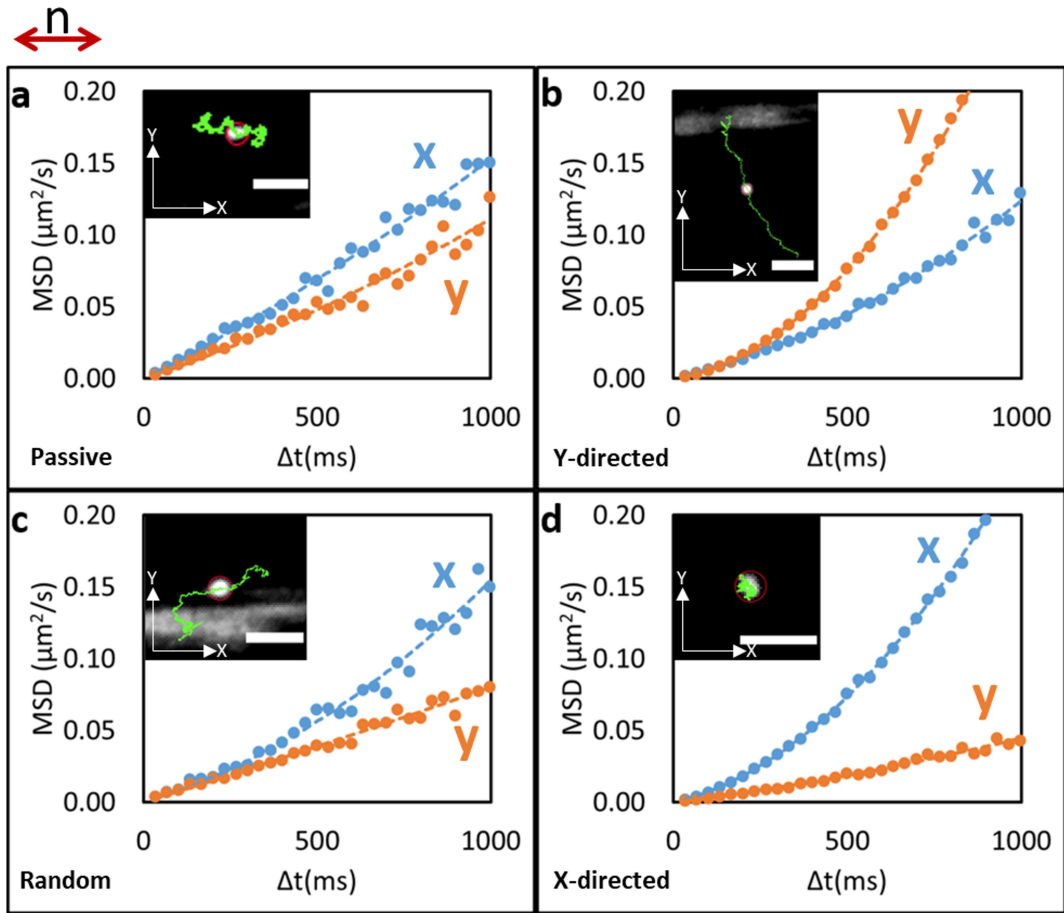


Figure 4.16: MSD data of the AuCr@TiO<sub>2</sub> Janus particles under UV illumination. a) Passive particle. b) y-directed. c) x- and y-directed. d) x-directed. The scale bars are 5  $\mu\text{m}$  for each trajectory image. Nematic director of the LC is directed along x-direction as shown with two headed red arrow.

We also observed that for the particles activated in both directions and y-direction, the average velocities are greater than the samples' averages. Besides that, these particle trajectories were covered after a local movement of the particles. These additional observations might indicate that these particles may interact more with LC/Aqueous interface at the first incident of UV light exposure. After a time interval, these particles may move along the z-direction to continue their motion more in the aqueous domain. In **Figure 4.17-b** the activation directions of the Janus particles under UV illumination and the passive motion directions under visible light, **Figure 4.17-a**, are shown.

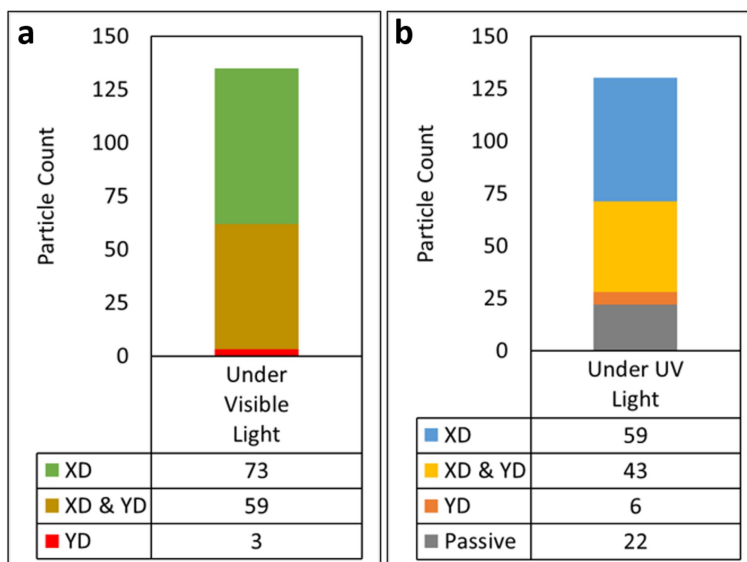


Figure 4.17: Active & passive motions of the same microparticles under a) Visible & b) UV light respectively. XD: x-directed, XD & YD : No specific direction, YD: y-directed, P: Passive.

Our first observation was that the activation of the JPs ceased drastically. First, we suspected that since the apparent viscosity of 5CB is much higher than water, the velocities of the Janus particles were decreased at the interface. However, when we analysed MSD data of the particles, **Figure 4.16**, we observed that the degree of activation of the particles was decreased. Our second hypothesis was that the regeneration of the electric double layer between 5CB and water might cause a disturbance in the activation steps of the JPs on the interface. To test hypotheses, we modelled a 1D model in COMSOL for the electric double layer thickness between 5CB and water, which will be investigated in the following sections.

We also calculated the levitation distance due to electrostatic repulsion between 5CB and our Janus particles as a function of NaCl concentration before adsorption onto 5CB. In theory, when there was no salt, the equilibrium distance between 5CB surface and Janus particle must be the greatest. Our calculation revealed that, when there is no salt, the particles must be over 5CB layer more than  $3.4 \mu\text{m}$  rather than interacting with. The calculation results are shown in **Appendix C**.

In order to calculate the thickness of the electric double layer between the LC and aqueous media, we need to find the surface charge density (SCD) of the LC while in contact with water. However, it is not an easy task since any measurement taken from near the surface will also affect the surface charge density of the LC/Aqueous interface simply because we introduce a new "surface" near the interface. Therefore, instead of directly measuring the SCD of the LC, we can measure the zeta potentials of LC at different salt-concentrated aqueous media to reveal the SCD of the LC surrounded by salt-concentrated media by **Equation 4.8**. [104]

$$SCD = \frac{2\varepsilon_r\varepsilon_0\kappa kT}{ze} \sinh\left(\frac{ze\zeta}{2kT}\right) \left[ 1 + \frac{1}{\kappa a} \frac{2}{\cosh^2(ze\zeta/4kT)} + \frac{1}{(\kappa a)^2} \frac{8 \ln \cosh(ze\zeta/4kT)}{\sinh^2(ze\zeta/2kT)} \right]^{\frac{1}{2}} \quad (4.8)$$

where  $\varepsilon_r$  and  $\varepsilon_0$  are relative and vacuum electric permittivity and  $\kappa$ ,  $k$ ,  $T$ ,  $z$ ,  $e$ ,  $a$  and  $\zeta$  stands for Debye-Hückel parameter, Boltzmann constant, absolute temperature, valance electron number of the salt, elementary electric charge, a hydrodynamic radius of the colloid and zeta potential respectively. From **Equation 4.8**, assuming that the 5CB droplets are  $0.5 \mu\text{m}$  in radius, we have calculated the SCD of 5CB at different NaCl salt concentrations. The results of the SCD calculation of 5CB are shown in **Table 4.1** below.

Table 4.1: Surface charge densities of 5CB in various aqueous NaCl solutions

NaCl Conc. (mM)	Debye Length (nm)	SCD ( $e/\text{nm}^2$ )
300	0.6	0.1424
100	1	0.0462
10	3.0	0.0349
1	9.6	0.0466
0.1	30.3	0.0108

We observed from **Table 4.1** that when the NaCl concentration increases the Debye length, which is the inverse of Debye-Hückel parameter, decreases since the system has more ions in total. On the contrary, the SCD value has increased with the

increasing salt concentration of aqueous media. These results might also be a complementary reason for the ceased activation of AuCr@TiO<sub>2</sub> JPs at the interface at high salt-concentrated media since the AuCr@TiO<sub>2</sub> JPs might not be activated near a highly charged surface.

As we have suspected that the regenerated electric double layer between 5CB and aqueous media might interrupt the concentration gradient around AuCr@TiO<sub>2</sub> Janus particles, which enables these particles to move anisotropically under UV illumination, we have simulated a similar 5CB aqueous interface electric double layer in COMSOL. Since COMSOL uses an iterative numerical approach to solve the mathematical equations for physical phenomena, we have selected the salt concentration in the environment to 0.1 and 1 mM, respectively. Since direct measurement of surface charge density (SCD) of 5CB was not possible, we have used the SCD values from zeta potential measurements. The COMSOL simulation uses the coupled physics of electrostatics and the transport of diluted species for the electrostatic interaction of ions at the interface between 5CB and water. Our simulation revealed that, from **Figure 4.18**, with the 1 mM salt concentration, the electric potential at the 5CB/aqueous interface did not cease until 0.06  $\mu\text{m}$  even without any Janus particle interaction. It also revealed that when the salt concentration was increased to only 1 mM, the electric double layer thickness increases more than 4 times, around 0.21  $\mu\text{m}$ . This parameter change also underlies the significant effect of salt concentration on the thickness of the electric double layer. Besides that, since Janus particles also possess a charge-dense region around themselves in aqueous media, the region between LC and Janus particles would have greater charge-dense space in reality. Therefore, the disturbance of the generation of the concentration gradient step on activation of Janus particles is highly possible. In addition, since the simulation was done for salt concentrated media, contrary to our original designed system, the electric double layer thickness would be much higher, which negatively impacts the active motion of AuCr@TiO<sub>2</sub> JPs. For instance, assuming a linear relationship between the salt concentration and the electric potential decrease distance, decreasing the salt concentration from 1 mM to 0 mM increases the electric potential decrease distance to around 0.8  $\mu\text{m}$  that it becomes comparable with our Janus particles' dimensions.

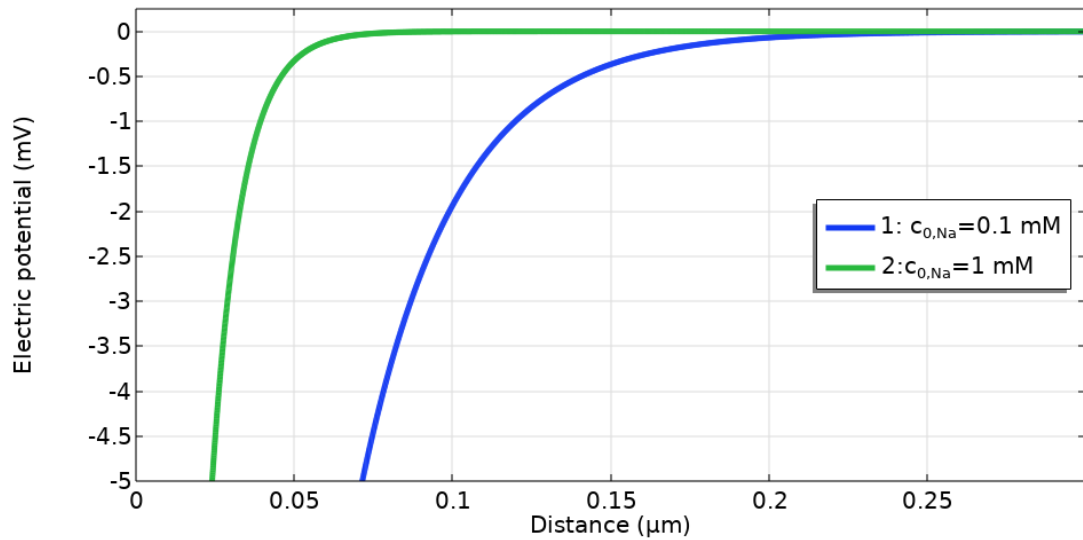


Figure 4.18: COMSOL 1D simulation results for electric potential between 5CB & Aqueous media

We thought that even considerably dilute concentrations of salt concentration, orders of magnitude of millimolar (mM), could alter the activation behaviour of our Janus particles. Therefore, we wanted to investigate further the thickness of the possible electric double layer between; LC flat surface & aqueous media and our Janus particles & aqueous media, respectively. We calculated the electric double layer until the surface charge density value had decreased to 99% of its value to include all the ions in the interface region. [105]. From **Table 4.2**, we observed that since AuCr@TiO<sub>2</sub> particles are in micrometer size region, the effect of geometry did not change the calculated EDL thickness significantly at low concentrations of NaCl, 0.1 and 1 mM respectively. However, in **Table 4.2** we observe that as the salt concentration decreases from 300 mM to 1 mM, the electric double layer thickness (EDL) increases significantly. This alternative approach to calculating the EDL thickness gave similar results to our COMSOL simulation in magnitude.

Table 4.2: Calculation of Debye-Hückel parameter, Debye length and EDL of 5CB & AuCr@TiO<sub>2</sub> in various aqueous NaCl solutions

NaCl Conc. (mM)	$\kappa$ (nm <sup>-1</sup> )	Debye Length (nm)	EDL-5CB (nm)	EDL-AuCr@TiO <sub>2</sub> (nm)
300	1.81	0.6	2.0	2.0
100	1.04	1.0	3.5	3.5
10	0.33	3	11.2	11.2
1	0.10	9.6	35.4	35.3
0.1	0.03	30.3	111.9	111.6

For AuCr@TiO<sub>2</sub> Janus particles to move actively, it is necessary to make electrons migrate from TiO<sub>2</sub> hemisphere to Au capped hemisphere. When there are concentrated ions in the space, such as salt concentrated media or the presence of LC/Aqueous interface, the migration of electrons could be interrupted by the environment; hence we saw a decrease in the activation of the AuCr@TiO<sub>2</sub> Janus particles. Therefore, we concluded that any particle that requires electron gradient on themselves to move actively would be affected by the generated EDL between the LC/Aqueous interface and these particles are not suitable for generating mechanical shear on the LC/Aqueous interface since they cannot achieve high velocities by UV activation.

## 4.2 Microcargo Release via Interfacial Microstirrers

We designed a different microcargo release system based on LC/Aqueous interface and paramagnetic iron oxide particles. In this system, as shown in **Figure 4.19**, the paramagnetic iron oxide microparticles (PIM) were sedimented and aligned on the LC(E7)/Aqueous interface with the help of magnetic flux. The sedimentation of the particles was done in 0.3 M NaCl aqueous solution to eliminate the electrostatic repulsion effects. Before each activation experiment, the NaCl in the media was cleansed with at least 6 times the sample volume to regenerate the electrical double layer at the LC/Aqueous interface. The regeneration of the electrical double layer is crucial for our release experiments since the electrical double layer force acts in favour of releasing the aqueous droplets from LC domain. The aqueous MB loaded droplets were designed as before, having a homeotropic anchoring due to 2mM CTAB concentra-

tion which entraps the aqueous droplets beneath the LC/Aqueous interface. When idle, the paramagnetic microparticles form microstirrers parallel to the magnetic flux. In order to release microcargo, these interfacial rod-shaped aggregates (microstirrers) should move at the interface while generating enough energy to induce an internal flow for the release of the droplets.

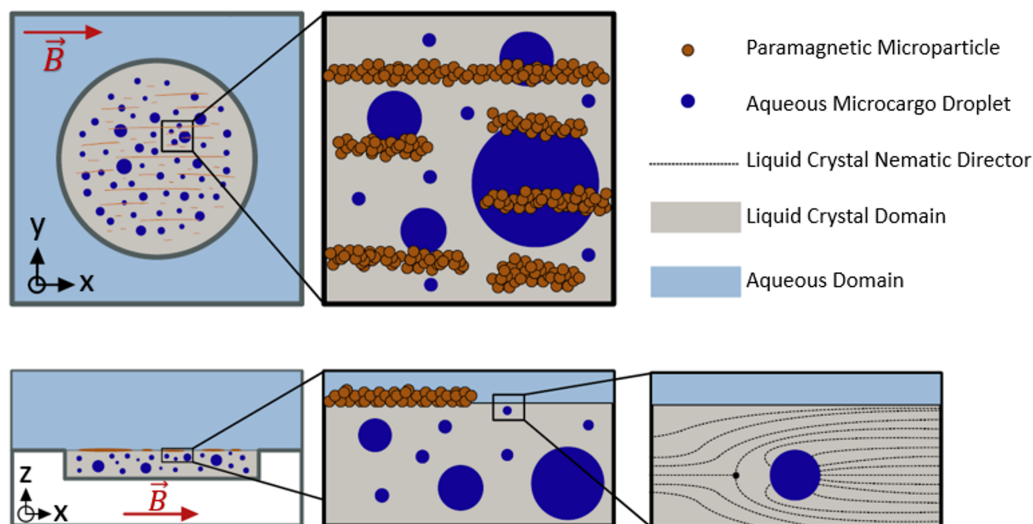


Figure 4.19: Sketch of liquid crystal based microcargo release method replacing motile bacteria with paramagnetic microparticle based microstirrers.

In **Figure 4.20-a**, the SEM images revealed that the iron oxide particles have round shapes and smooth surfaces. It was also noticeable that the particles have distinct surface regions, indicating that the crystal structure on the surface was not homogeneous after the autoclave step. We have analysed the SEM images for average diameter and found the average diameter as  $797 \pm 103$  nm. We also observed some larger iron oxide particles, **Figure 4.20-b**, that were generally merged with each other. In the average diameter calculations, these particles were omitted since their number was insignificant. We did not separate these big particles from the batch since they were also magnetic and could enhance the microcargo release rate due to their size.

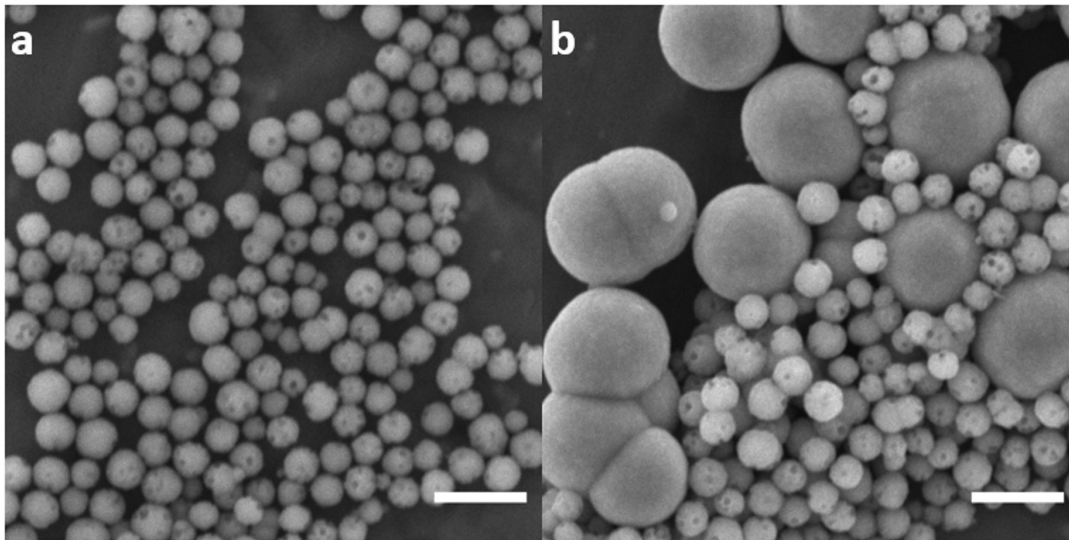


Figure 4.20: a) Average particle shape & surface morphology of iron oxide particles. b) Big particles merged each other. Scale bars are 2  $\mu\text{m}$ .

The micrographs of the interfacial microstirrers show the linear assembly of the microparticles in **Figure 4.21-a** at idle state. For each micrograph, the red arrow shows the direction of the magnetic flux. The microstirrer assemblies were able to follow the magnetic flux direction as the magnetic flux orientation was changed from **Figure 4.21-a** to **Figure 4.21-b**. The double-headed arrows in **Figure 4.21-b,-c,-d,-e** show the polarized filter directions. In these directions, the polarized micrograph should give a dark appearance. The polarized micrograph in **Figure 4.21-c** shows that the particles did not alter the nematic director orientation as they were idle since the liquid crystal layer has been directed along x-direction parallel to one of the polarized filters. However, when the magnetic flux director altered, the microstirrer assemblies could change the nematic director orientation locally, as appear in **Figure 4.21-d** with bright regions. The nematic director orientation change could also be observed in **Figure 4.21-e,-f** with polarized and retarded micrographs. The bright regions in **Figure 4.21-f** showed the local changes in nematic director orientation when the applied magnetic field direction was changed.

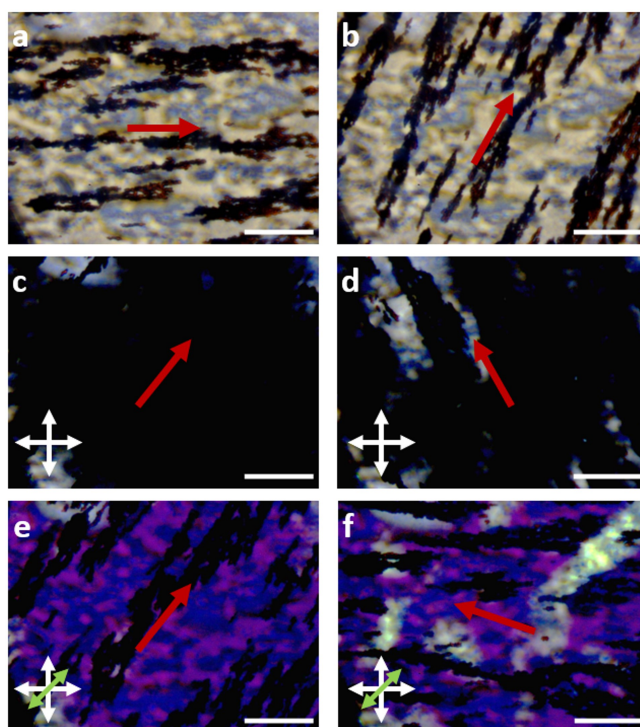


Figure 4.21: a-b) Bright field micrographs of interfacial microstirrers under applied magnetic field. c) Polarized micrograph of the same region when the interfacial microstirrers were idle. d) Polarized micrograph of the same region in part c with orientation change of magnetic field resulting in local nematic director change in the sample, appeared as bright regions. e-f) Same configurations in part c and d respectively with additional retarder lens positioned  $45^\circ$  with respect to the polarized filters. Red arrow shows the applied magnetic flux direction. The scale bars are  $50 \mu\text{m}$  for all parts.

For our microcargo release system, it is desired to have on-demand release. Therefore, the ability to be activated upon applied magnetic flux over cycles is important. For this reason, we tested our iron oxide microparticles in terms of paramagnetism with vibrating sample magnetometer (VSM). In **Figure 4.22**, the VSM measurements showed that our synthesis resulted in a type of magnetic particles that could be classified as paramagnetic since the VSM analysis also showed magnetic excitement upon the applied magnetic field. We also noticed that the particles do not show any lag in magnetism since there is no hysteresis in **Figure 4.22**. This result indicates that the particles could be excited on demand without any time lag, which is a good

property for on-demand release systems. In addition, the particles have high paramagnetism that could be further classified as superparamagnetic since the particles showed great magnetic susceptibility, between 40 and -40 emu/g, upon the applied magnetic field. [106]

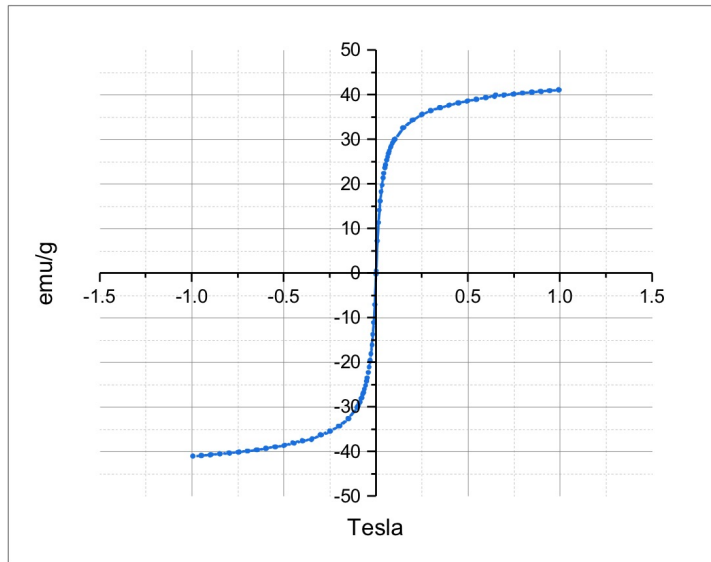


Figure 4.22: VSM analysis of superparamagnetic iron oxide microparticles. The curves show no hysteresis attests to no lag of the magnetic excitement.

After the characterisation of the paramagnetic iron oxide microparticles (PIM) we have constructed the same system shown in **Figure 4.19**. First, we dispersed the PIMs in 0.3 M NaCl solution to sediment the particles. Different from the previous method, we have used forced sedimentation with the applied magnetic field below our system. The applied magnetic field was parallel to the LC/Aqueous interface to generate rod-shaped assemblies that could be spun like microstirrers upon shifting the magnetic field orientation, **Figure 4.23**. When the magnetic stirrer was idle, denoted as time  $<0$  in **Figure 4.23**, the particles were aligned but did not apply mechanical shear to the liquid crystal layer as shown in **Figure 4.21-a**. After time  $\geq 0$ , when the release was demanded, the magnetic stirrer started to spin at a predetermined RPM value. As time increases, the aqueous droplets loaded with MB were released to the aqueous domain via the mechanical shear generated by the interfacial magnetic microstirrers, **Figure 4.23**. For our system, the initial aqueous droplet size ranges

from a few micrometers to 20  $\mu\text{m}$ .

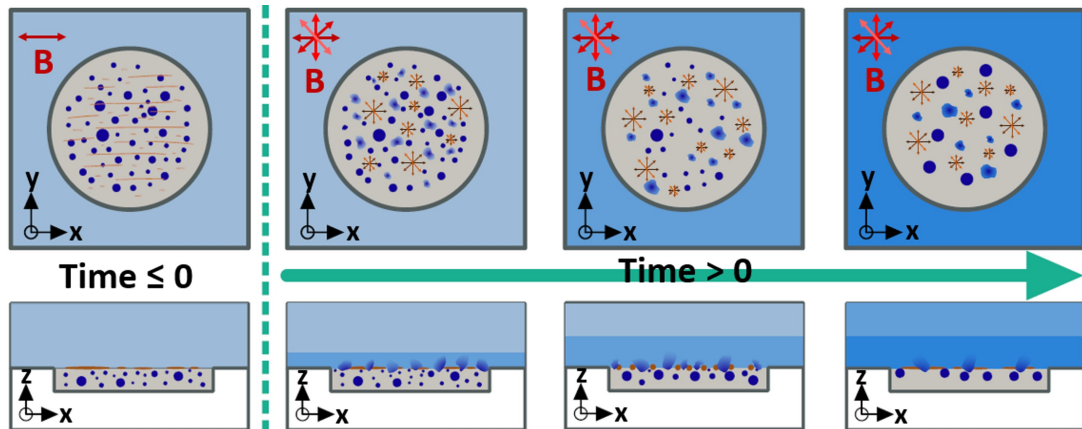


Figure 4.23: Representative sketch of working mechanism of microcargo release method based on liquid crystal and paramagnetic microstirrers

We have used a magnetic stirrer to shift the magnetic flux director on the interface. For this parameter, we have selected 3 different rotation speed values as 250, 500 and 1000 RPM, respectively. The designed experiment had two parts. Firstly, we wanted to test the on demand response of the system. Thus, we included a time interval between 60<sup>th</sup> and 120<sup>th</sup> minutes when we did not want to release any mass from liquid crystal domain to aqueous environment. Secondly, we wanted to see the effect of possible release patterns on the overall microcargo release rate. The area concentration for these experiments were set to be 20.000 particles/mm<sup>2</sup>. The PDMS well was filled with approximately 20  $\mu\text{L}$  water-in-liquid crystal emulsion which had 2.5v% water droplets containing 18  $\mu\text{g}/\mu\text{L}$  MB and 2 mM CTAB, **Figure 4.23**. On top of the liquid crystal layer, there was aqueous domain clear of methylene blue initially. As we made the particles to release methylene blue containing droplets which were available at the liquid crystal/aqueous interface, the aqueous domain turned to blue slowly, **Figure 4.23** and we measured the UV-Vis peak at 664 nm for the presence of the MB.

The PDMS wells contain approximately 20  $\mu\text{L}$  volume. Since the water-in-LC emulsion contains 2.5v%, 18  $\mu\text{g}/\mu\text{L}$  aqueous MB droplets, the total available MB to be released was approximately 9  $\mu\text{g}$  per sample. At the beginning of each release event, between 0<sup>th</sup> and 60<sup>th</sup> minutes, there was a rapid release as shown in **Figure 4.24** for

250, 500, and 100 RPM experiment. In the first hour of the release experiments, the samples at 250, 500 and 1000 RPM released approximately 17%, 28%, and 60% of the available microcargo, respectively. The increase in the release rate as the rotational speed increases could be explained by two reasons. Firstly, as the rotational speed increases, the microstirrers would have more rotational energy to cause greater internal flow in LC domain. Secondly, the microstirrers would be smaller as the rotational speed increases, but the area percentage they cover would increase. More details will be given following sections. There is a rapid release in each rotational speed experiments. We speculated that these rapid releases might result from the number of available droplets to be released near the interface at the beginning of the experiments. On the other hand, depending on the RPM value, even if the sedimentation times for the iron oxide microparticles were the same, the initial release rate differed from each other at the start of the experiments, **Figure 4.24**. We hypothesized that, as we increased the shifting rate of the magnetic flux director orientation, the possibility of the interfacial microstirrers releasing the microcargo carrying droplets to the aqueous domain increases. Each spin on the interface would apply mechanical shear on their path, large enough to change the nematic order of the liquid crystal locally as shown in **Figure 4.21-e,-f**.

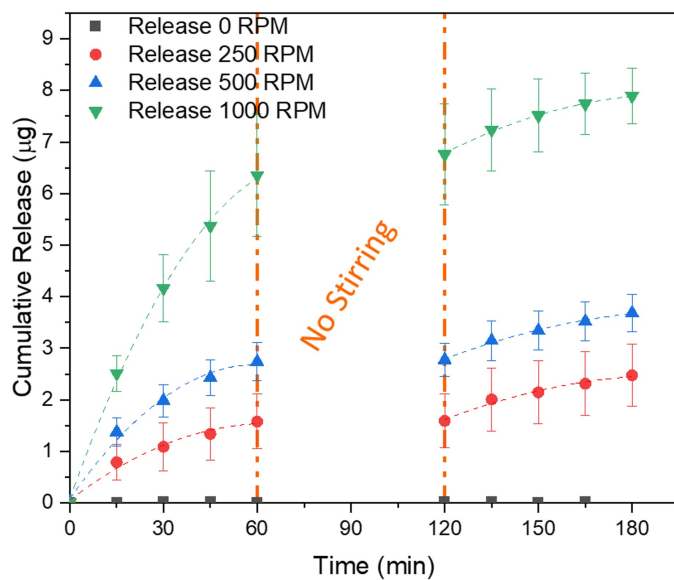


Figure 4.24: MB release via interfacial microstirrers on LC/Aqueous interface at different RPMs.

After 1 hour of release, between 60<sup>th</sup> and 120<sup>th</sup> minutes, the magnetic stirrer beneath the samples was turned off. This way, the magnetic flux director did not shift for one hour. As a result, since there was no shear due to paramagnetic microstirrer movement on the surface, the system released no mass regardless of the RPM value, **Figure 4.24**. After this interval, when we started the magnetic stirrers, the samples again started to release MB. However, we observed that the release ceased. When we assume linear release rate, the release rates decreased from roughly 100 ng/min, 42 ng/min, and 25 ng/min to 25 ng/min, 17 ng/min, and 12 ng/min for 1000, 500 and 250 RPM, respectively. We speculated that there might be three main reasons for the decrease in release rate. Firstly, as we continued to release mass to the aqueous domain, the number of water droplets available beneath the interface decreased. Therefore, there should be a time interval for the lower level water droplets to get near the LC/Aqueous interface to be released. Secondly, as time increases, the MB-loaded water droplets might tend to form bigger droplets in LC or they might form of smaller droplet clusters via topological defects. These clusters could not cross the available release regions due to their sizes. Lastly, as time passes, the particles on the interface might form a swarm of microstirrers that spin on the interface due to the application strategy of magnetic flux. As a result, since the whole interface was not fully covered, the available release locations differ at any instant, which results in a slower release rate compared to the start of the experiment. Moreover, we also observed that our control over the release might decrease as we increase the RPM value since the samples for higher RPM value have more standard deviation, **Figure 4.24**. Lastly, to prove the need for shifting magnetic flux on the system for microcargo release, we have constructed the same setup; however we did not turn on the magnetic stirrers. As a result, the system did not release any mass, as shown in **Figure 4.24** with grey squares, which was the indication of the requirement of shifting of magnetic flux in order to generate mechanical shear on the interface resulting in microcargo release.

Another parameter that affects the release rate of the microcargo is the area concentration of the magnetic particles at the interface. To observe the impact of this effect, we have constructed the same experiment replacing the water-in-liquid crystal emulsion with olive oil to have a better view of the interface. At 250 RPM, we could observe the interfacial microstirrer movements on olive oil clearly. From **Figure 4.25 -a,-b,-c**,

when the particle number concentration was 10,000 Particles/mm<sup>2</sup>, the microstirrers were bigger, and there were fewer aggregates on the oil/aqueous interface. However, when the particle number concentration was increased to 40,000 Particles/mm<sup>2</sup>, there were more aggregates at the same time intervals with smaller microstirrers, **Figure 4.25 -d,-e,-f**. Moreover, since the particles were force sedimentated, the required time for the microstirrer assemblies to form increased as the particle area concentration increased. We also noticed that the magnetic stirrer's position beneath the sample greatly impacts the distribution of the magnetic microstirrers on the oil/Aqueous interface. These observations may also indicate the decrease in the release rate discussed below.

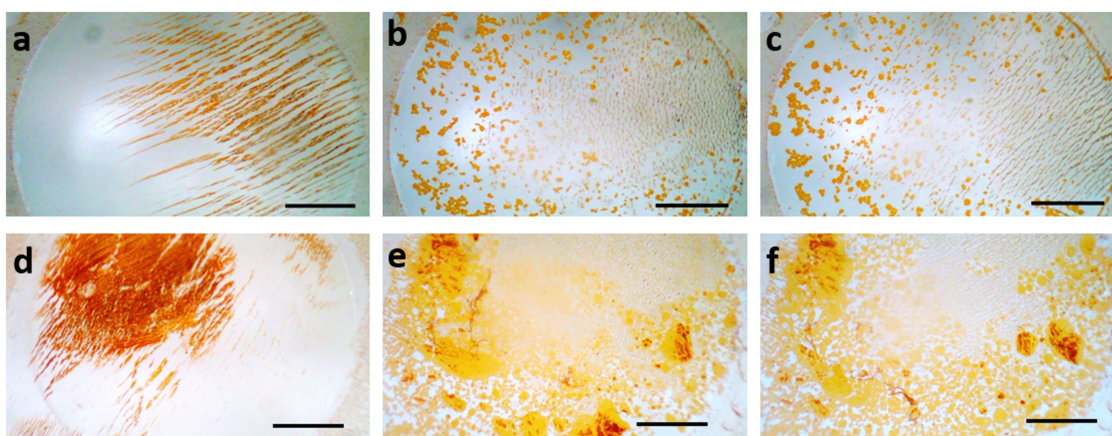


Figure 4.25: Magnetic particles at 250 RPM on the olive oil/Aqueous interface forming interfacial microstirrers at t=0, t= 9 and t= 18 min. a,b,c) 10,000 Particle/mm<sup>2</sup>. d,e,f) 40,000 Particle/mm<sup>2</sup>. The scale bars are 1 mm for each image.

To find the optimal area concentration of paramagnetic particles to form interfacial microstirrers on the LC/Aqueous interface, we repeated the microcargo release experiments at 250 RPM for a 3-hour continuous release. We have selected area number concentrations 10,000, 20,000, and 40,000 particles/mm<sup>2</sup>. From **Figure 4.26**, we have seen that as particle number concentration was 10,000 Particles/mm<sup>2</sup>, the system release rate was limited by the number of available release regions since there was a slight decrease on the rate of release over time. However, when we increased the particle concentration to 20,000 Particles/mm<sup>2</sup>, there was a greater decrease in the initial release rate. We thought that in the 20,000 Particles/mm<sup>2</sup> setup, the rate-limiting part was not the available release regions but available water droplets beneath the inter-

face. Over time, most of these microcargo-loaded water droplets were released to the aqueous media and new water droplets at lower levels need time to reach the interface. Interestingly, when we increased the particle concentration from 20,000 particles/cm<sup>2</sup> to 40,000 particles/cm<sup>2</sup>, the release rate decreased roughly 3 folds from 100 ng/min to 33 ng/min, as shown in **Figure 4.26**. We thought that the area concentration of the particles might be so high that there was crowding on the interface, which did not let the water droplets escape to the aqueous domain. For example, assuming 1  $\mu\text{m}$  diameter for each particle, a 50  $\mu\text{m}$  microstirrer consists of 25 consecutive particles. This microstirrer could cover approximately 1963  $\mu\text{m}^2$  as it spins. Thus, to cover a 1 mm<sup>2</sup> area, only 13,000 particles are needed. In the real case, the particles could overlap, and the microstirrers are not uniformly distributed in size. Therefore, the optimal particle concentration for the maximum release rate could be higher than 13,000 Particles/mm<sup>2</sup>. This calculation also gives a similar outcome as the release results in **Figure 4.26**.

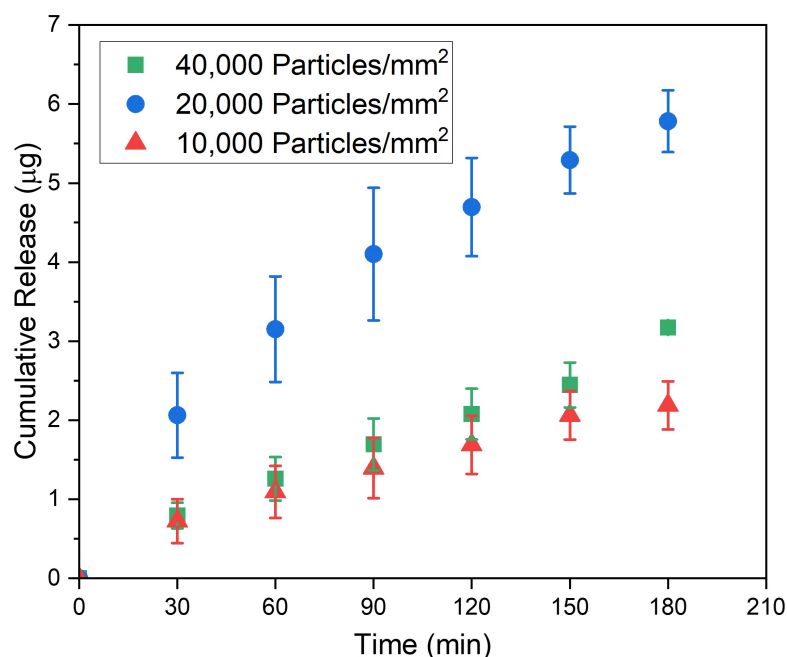


Figure 4.26: MB release via paramagnetic microstirrers on LC/Aqueous interface at different area concentrations.

When we compare the experimental results in **Figure 4.24** and **Figure 4.26**, and theoretical calculation results, **Figure 4.3**; we can say that the outcomes are parallel to each other. When there was no shear, 0 RPM, the particles do not apply shear to the

liquid crystal interface to disturb the net force balance. Thus, no mass was released from the liquid crystal domain since the droplets cannot overcome the elastic energy barrier. Therefore, we can conclude that in order to have on-demand microcargo release from LC domain we need three conditions:

- The microcargo-loaded droplets must be in relationship with the interface in an attractive fashion.
- The elastic energy barrier must be high enough to entrap the microcargo droplets in LC domain.
- The paramagnetic microparticles must be applying mechanical shear on demand onto LC/Aqueous interface, which favours the release of microcargo.

## CHAPTER 5

### CONCLUSION

We aimed to design an alternative microcargo release method derived from the bacterial movement on the surface of liquid crystals. To achieve this objective, we have carried out a literature survey about the microparticles which replace the bacteria in our systems for controlled, on-demand release. We have selected two possible candidates for active migration on LC/Aqueous interface. We first selected, AuCr@TiO<sub>2</sub> Janus particles, to replicate the anisotropic movement of bacteria. The second microparticle, paramagnetic ironoxide, was selected to form microstirrers on the LC/Aqueous interface and induce internal flow as the magnetic field was applied, which was a different approach than simply replicating the translational motion of the bacteria.

We propose an alternative method for microcargo release using interfacial magnetic microstirrers with water-in-liquid crystal emulsion. Simple making of the structured oil and aqueous microcargo emulsion with the desired amount of paramagnetic ironoxide particles can be further investigated and used in the future for on-demand, controlled release at nanograms/min level.

In our study, we proved that AuCr@TiO<sub>2</sub> Janus particles and any other microparticle that uses concentration gradient on themselves to move anisotropically are not suitable to be used in both salt concentrated media and 5CB/Aqueous interface. We also proved that the microparticles that we have worked with would not sediment on the 5CB while in contact with pure water because of electrostatic repulsion and need a sedimentation step. Therefore, we have found a way to adsorb different kinds of microparticles on 5CB contact with aqueous media. We have proved that EDL thickness is comparable with our Janus particle sizes and hence may disturb the required electron migration step for anisotropic motion of AuCr@TiO<sub>2</sub> Janus particles. We have

designed an alternative microcargo release system with paramagnetic iron oxide microparticles on structured oil/water emulsion. We showed that the release rate of our design system can be tuned by changing the magnetic flux rotation speed or changing the area concentration of microparticles.

## REFERENCES

- [1] D. Guimarães, A. Cavaco-Paulo, and E. Nogueira, “Design of liposomes as drug delivery system for therapeutic applications,” *International journal of pharmaceutics*, vol. 601, p. 120571, 2021.
- [2] Y.-K. Kim, X. Wang, P. Mondkar, E. Bukusoglu, and N. L. Abbott, “Self-reporting and self-regulating liquid crystals,” *Nature*, vol. 557, no. 7706, pp. 539–544, 2018.
- [3] E. Bukusoglu, M. B. Pantoja, P. C. Mushenheim, X. Wang, and N. L. Abbott, “Design of responsive and active (soft) materials using liquid crystals,” *Annual review of chemical and biomolecular engineering*, vol. 7, p. 163, 2016.
- [4] M. Lengyel, N. Kállai-Szabó, V. Antal, A. J. Laki, and I. Antal, “Microparticles, microspheres, and microcapsules for advanced drug delivery,” *Scientia Pharmaceutica*, vol. 87, no. 3, p. 20, 2019.
- [5] A. A. Dayyih, M. Alawak, A. M. Ayoub, M. U. Amin, W. A. Dayyih, K. Engelhardt, L. Duse, E. Preis, J. Brüßler, and U. Bakowsky, “Thermosensitive liposomes encapsulating hypericin: Characterization and photodynamic efficiency,” *International Journal of Pharmaceutics*, vol. 609, p. 121195, 2021.
- [6] A. Yavlovich, A. Singh, R. Blumenthal, and A. Puri, “A novel class of photo-triggerable liposomes containing dppc: Dc8, 9pc as vehicles for delivery of doxorubicin to cells,” *Biochimica et Biophysica Acta (BBA)-Biomembranes*, vol. 1808, no. 1, pp. 117–126, 2011.
- [7] Y. Yoshizaki, E. Yuba, T. Komatsu, K. Udaka, A. Harada, and K. Kono, “Improvement of peptide-based tumor immunotherapy using ph-sensitive fusogenic polymer-modified liposomes,” *Molecules*, vol. 21, no. 10, p. 1284, 2016.
- [8] K. Y. Vlasova, A. Piroyan, I. M. Le-Deygen, H. M. Vishwasrao, J. D. Ramsey, N. L. Klyachko, Y. I. Golovin, P. G. Rudakovskaya, I. I. Kireev, A. V. Kabanov,

- et al.*, “Magnetic liposome design for drug release systems responsive to super-low frequency alternating current magnetic field (ac mf),” *Journal of colloid and interface science*, vol. 552, pp. 689–700, 2019.
- [9] B. E.-F. de Ávila, P. Angsantikul, J. Li, M. Angel Lopez-Ramirez, D. E. Ramírez-Herrera, S. Thamphiwatana, C. Chen, J. Delezuk, R. Samakapiruk, V. Ramez, *et al.*, “Micromotor-enabled active drug delivery for in vivo treatment of stomach infection,” *Nature communications*, vol. 8, no. 1, pp. 1–9, 2017.
- [10] K. Kim, X. Xu, J. Guo, and D. Fan, “Ultrahigh-speed rotating nanoelectromechanical system devices assembled from nanoscale building blocks,” *Nature communications*, vol. 5, no. 1, pp. 1–9, 2014.
- [11] Z. Wu, B. E.-F. De Avila, A. Martín, C. Christianson, W. Gao, S. K. Thamphiwatana, A. Escarpa, Q. He, L. Zhang, and J. Wang, “Rbc micromotors carrying multiple cargos towards potential theranostic applications,” *Nanoscale*, vol. 7, no. 32, pp. 13680–13686, 2015.
- [12] M. Liu, L. Pan, H. Piao, H. Sun, X. Huang, C. Peng, and Y. Liu, “Magnetically actuated wormlike nanomotors for controlled cargo release,” *ACS Applied Materials & Interfaces*, vol. 7, no. 47, pp. 26017–26021, 2015.
- [13] J. K. Gupta and N. L. Abbott, “Principles for manipulation of the lateral organization of aqueous-soluble surface-active molecules at the liquid crystal-aqueous interface,” *Langmuir*, vol. 25, no. 4, pp. 2026–2033, 2009.
- [14] O. D. Lavrentovich, “Transport of particles in liquid crystals,” *Soft Matter*, vol. 10, no. 9, pp. 1264–1283, 2014.
- [15] I. Musevic, M. Skarabot, U. Tkalec, M. Ravnik, and S. Zumer, “Two-dimensional nematic colloidal crystals self-assembled by topological defects,” *Science*, vol. 313, no. 5789, pp. 954–958, 2006.
- [16] G. M. Koenig Jr, I.-H. Lin, and N. L. Abbott, “Chemoresponsive assemblies of microparticles at liquid crystalline interfaces,” *Proceedings of the National Academy of Sciences*, vol. 107, no. 9, pp. 3998–4003, 2010.

- [17] M. Tsuei, H. Sun, Y.-K. Kim, X. Wang, N. C. Gianneschi, and N. L. Abbott, “Interfacial polyelectrolyte–surfactant complexes regulate escape of microdroplets elastically trapped in thermotropic liquid crystals,” *Langmuir*, vol. 38, no. 1, pp. 332–342, 2021.
- [18] P. de Gennes and J. Prost, “The physics of liquid crystals new york: Oxford univ,” *Press [Google Scholar]*, 1995.
- [19] D. Chen, M. Nakata, R. Shao, M. Tuchband, M. Shuai, U. Baumeister, and W. Weiss, “og, dm walba, ma glaser, je maclennan and na clark,” *Phys. Rev. E: Stat., Nonlinear, So Matter Phys*, vol. 89, no. 1-5, p. 022506, 2014.
- [20] S. Meiboom, J. P. Sethna, P. Anderson, and W. Brinkman, “Theory of the blue phase of cholesteric liquid crystals,” *Physical Review Letters*, vol. 46, no. 18, p. 1216, 1981.
- [21] B. Jerome, “Surface effects and anchoring in liquid crystals,” *Reports on Progress in Physics*, vol. 54, no. 3, p. 391, 1991.
- [22] N. A. Lockwood, J. K. Gupta, and N. L. Abbott, “Self-assembly of amphiphiles, polymers and proteins at interfaces between thermotropic liquid crystals and aqueous phases,” *Surface Science Reports*, vol. 63, no. 6, pp. 255–293, 2008.
- [23] P. J. Collings and M. Hird, “Introduction to liquid crystals (chemistry & physics) taylor & francis publishers ltd,” 1997.
- [24] O. D. Lavrentovich, “Topological defects in dispersed words and worlds around liquid crystals, or liquid crystal drops,” *Liquid crystals*, vol. 24, no. 1, pp. 117–126, 1998.
- [25] M. Khan, A. R. Khan, J.-H. Shin, and S.-Y. Park, “A liquid-crystal-based dna biosensor for pathogen detection,” *Scientific reports*, vol. 6, no. 1, pp. 1–12, 2016.
- [26] J. M. Brake, A. D. Mezera, and N. L. Abbott, “Effect of surfactant structure on the orientation of liquid crystals at aqueous- liquid crystal interfaces,” *Langmuir*, vol. 19, no. 16, pp. 6436–6442, 2003.

- [27] R. Dong, Q. Zhang, W. Gao, A. Pei, and B. Ren, "Highly efficient light-driven tio<sub>2</sub>-au janus micromotors," *ACS nano*, vol. 10, no. 1, pp. 839–844, 2016.
- [28] J. Yang, D. Shen, Y. Wei, W. Li, F. Zhang, B. Kong, S. Zhang, W. Teng, J. Fan, W. Zhang, *et al.*, "Monodisperse core-shell structured magnetic mesoporous aluminosilicate nanospheres with large dendritic mesochannels," *Nano Research*, vol. 8, no. 8, pp. 2503–2514, 2015.
- [29] S. Bale, A. Khurana, A. S. S. Reddy, M. Singh, and C. Godugu, "Overview on therapeutic applications of microparticulate drug delivery systems," *Critical Reviews™ in Therapeutic Drug Carrier Systems*, vol. 33, no. 4, 2016.
- [30] M. Whelehan and I. W. Marison, "Microencapsulation using vibrating technology," *Journal of microencapsulation*, vol. 28, no. 8, pp. 669–688, 2011.
- [31] M. Peanparkdee, S. Iwamoto, and R. Yamauchi, "Microencapsulation: a review of applications in the food and pharmaceutical industries," *Reviews in Agricultural Science*, vol. 4, pp. 56–65, 2016.
- [32] B. Wang, L. Hu, and T. J. Siahaan, *Drug delivery: principles and applications*. John Wiley & Sons, 2016.
- [33] T. Desai and L. D. Shea, "Advances in islet encapsulation technologies," *Nature reviews Drug discovery*, vol. 16, no. 5, pp. 338–350, 2017.
- [34] Y. Yi, L. Sanchez, Y. Gao, and Y. Yu, "Janus particles for biological imaging and sensing," *Analyst*, vol. 141, no. 12, pp. 3526–3539, 2016.
- [35] Z. Gong, T. Hueckel, G.-R. Yi, and S. Sacanna, "Patchy particles made by colloidal fusion," *Nature*, vol. 550, no. 7675, pp. 234–238, 2017.
- [36] A. Ozturk, S. S. Ozturk, B. Palsson, T. Wheatley, and J. B. Dressman, "Mechanism of release from pellets coated with an ethylcellulose-based film," *Journal of controlled release*, vol. 14, no. 3, pp. 203–213, 1990.
- [37] A. D. Bangham and R. Horne, "Negative staining of phospholipids and their structural modification by surface-active agents as observed in the electron microscope," *Journal of molecular biology*, vol. 8, no. 5, pp. 660–IN10, 1964.

- [38] R. Nisini, N. Poerio, S. Mariotti, F. De Santis, and M. Fraziano, “The multirole of liposomes in therapy and prevention of infectious diseases,” *Frontiers in Immunology*, vol. 9, p. 155, 2018.
- [39] M. Kapoor, S. L. Lee, and K. M. Tyner, “Liposomal drug product development and quality: current us experience and perspective,” *The AAPS journal*, vol. 19, no. 3, pp. 632–641, 2017.
- [40] C. Sebaaly, H. Greige-Gerges, S. Stainmesse, H. Fessi, and C. Charcosset, “Effect of composition, hydrogenation of phospholipids and lyophilization on the characteristics of eugenol-loaded liposomes prepared by ethanol injection method,” *Food bioscience*, vol. 15, pp. 1–10, 2016.
- [41] S. Emami, S. Azadmard-Damirchi, S. H. Peighambaroust, H. Valizadeh, and J. Hesari, “Liposomes as carrier vehicles for functional compounds in food sector,” *Journal of Experimental Nanoscience*, vol. 11, no. 9, pp. 737–759, 2016.
- [42] M. Pinot, S. Vanni, S. Pagnotta, S. Lacas-Gervais, L.-A. Payet, T. Ferreira, R. Gautier, B. Goud, B. Antonny, and H. Barelly, “Polyunsaturated phospholipids facilitate membrane deformation and fission by endocytic proteins,” *Science*, vol. 345, no. 6197, pp. 693–697, 2014.
- [43] S. G. Antimisiaris, P. Kallinteri, and D. G. Fatouros, *Liposomes and Drug Delivery*. Wiley, 2007.
- [44] F. Frezard, “Liposomes: from biophysics to the design of peptide vaccines,” *Brazilian Journal of Medical and Biological Research*, vol. 32, pp. 181–189, 1999.
- [45] C. T. Inglut, A. J. Sorrin, T. Kuruppu, S. Vig, J. Cicalo, H. Ahmad, and H.-C. Huang, “Immunological and toxicological considerations for the design of liposomes,” *Nanomaterials*, vol. 10, no. 2, p. 190, 2020.
- [46] S.-C. Lee, K.-E. Lee, J.-J. Kim, and S.-H. Lim, “The effect of cholesterol in the liposome bilayer on the stabilization of incorporated retinol,” *Journal of liposome research*, vol. 15, no. 3-4, pp. 157–166, 2005.

- [47] R. M. Elmoslemany, O. Y. Abdallah, L. K. El-Khordagui, and N. M. Khalafallah, "Propylene glycol liposomes as a topical delivery system for miconazole nitrate: comparison with conventional liposomes," *AAPS PharmSciTech*, vol. 13, no. 2, pp. 723–731, 2012.
- [48] S.-C. Lee, K.-E. Lee, J.-J. Kim, and S.-H. Lim, "The effect of cholesterol in the liposome bilayer on the stabilization of incorporated retinol," *Journal of liposome research*, vol. 15, no. 3-4, pp. 157–166, 2005.
- [49] Y. Lee and D. Thompson, "Stimuli-responsive liposomes for drug delivery," *Wiley Interdisciplinary Reviews: Nanomedicine and Nanobiotechnology*, vol. 9, no. 5, p. e1450, 2017.
- [50] C. Caddeo, R. Pons, C. Carbone, X. Fernández-Busquets, M. C. Cardia, A. M. Maccioni, A. M. Fadda, and M. Manconi, "Physico-chemical characterization of succinyl chitosan-stabilized liposomes for the oral co-delivery of quercetin and resveratrol," *Carbohydrate polymers*, vol. 157, pp. 1853–1861, 2017.
- [51] P. Zamani, A. A. Momtazi-Borojeni, M. E. Nik, R. K. Oskuee, and A. Sahebkar, "Nanoliposomes as the adjuvant delivery systems in cancer immunotherapy," *Journal of cellular physiology*, vol. 233, no. 7, pp. 5189–5199, 2018.
- [52] A. Hussain, S. Singh, D. Sharma, T. J. Webster, K. Shafaat, and A. Faruk, "Elastic liposomes as novel carriers: recent advances in drug delivery," *International journal of nanomedicine*, vol. 12, p. 5087, 2017.
- [53] J. H. Collier and P. B. Messersmith, "Phospholipid strategies in biomineralization and biomaterials research," *Annual Review of Materials Research*, vol. 31, no. 1, pp. 237–263, 2001.
- [54] B. S. Pattni, V. V. Chupin, and V. P. Torchilin, "New developments in liposomal drug delivery," *Chemical reviews*, vol. 115, no. 19, pp. 10938–10966, 2015.
- [55] L. A. Meure, N. R. Foster, and F. Dehghani, "Conventional and dense gas techniques for the production of liposomes: a review," *Aaps Pharmscitech*, vol. 9, no. 3, pp. 798–809, 2008.

- [56] P. R. Karn, W. Cho, and S.-J. Hwang, "Liposomal drug products and recent advances in the synthesis of supercritical fluid-mediated liposomes," *Nanomedicine*, vol. 8, no. 9, pp. 1529–1548, 2013.
- [57] A. Bangham, J. De Gier, and G. Greville, "Osmotic properties and water permeability of phospholipid liquid crystals," *Chemistry and physics of lipids*, vol. 1, no. 3, pp. 225–246, 1967.
- [58] A. Akbarzadeh, R. Rezaei-Sadabady, S. Davaran, S. W. Joo, N. Zarghami, Y. Hanifehpour, M. Samiei, M. Kouhi, and K. Nejati-Koshki, "Liposome: classification, preparation, and applications," *Nanoscale research letters*, vol. 8, no. 1, pp. 1–9, 2013.
- [59] O. R. Justo and A. M. Moraes, "Economical feasibility evaluation of an ethanol injection liposome production plant," *Chemical Engineering & Technology: Industrial Chemistry-Plant Equipment-Process Engineering-Biotechnology*, vol. 33, no. 1, pp. 15–20, 2010.
- [60] A. Wagner, K. Vorauer-Uhl, and H. Katinger, "Liposomes produced in a pilot scale: production, purification and efficiency aspects," *European journal of pharmaceuticals and biopharmaceutics*, vol. 54, no. 2, pp. 213–219, 2002.
- [61] C. Charcosset, A. El-Harati, and H. Fessi, "Preparation of solid lipid nanoparticles using a membrane contactor," *Journal of controlled release*, vol. 108, no. 1, pp. 112–120, 2005.
- [62] M. L. Manca, M. Manconi, A. M. Falchi, I. Castangia, D. Valenti, S. Lampis, and A. M. Fadda, "Close-packed vesicles for diclofenac skin delivery and fibroblast targeting," *Colloids and Surfaces B: Biointerfaces*, vol. 111, pp. 609–617, 2013.
- [63] B. William, P. Noemie, E. Brigitte, and P. Geraldine, "Supercritical fluid methods: An alternative to conventional methods to prepare liposomes," *Chemical Engineering Journal*, vol. 383, p. 123106, 2020.
- [64] Z. Huang, X. Li, T. Zhang, Y. Song, Z. She, J. Li, and Y. Deng, "Progress involving new techniques for liposome preparation," *Asian journal of pharmaceutical sciences*, vol. 9, no. 4, pp. 176–182, 2014.

- [65] M. K. Riaz, M. A. Riaz, X. Zhang, C. Lin, K. H. Wong, X. Chen, G. Zhang, A. Lu, and Z. Yang, "Surface functionalization and targeting strategies of liposomes in solid tumor therapy: A review," *International journal of molecular sciences*, vol. 19, no. 1, p. 195, 2018.
- [66] N. Plenagl, L. Duse, B. S. Seitz, N. Goergen, S. R. Pinnapireddy, J. Jedelska, J. Brüßler, and U. Bakowsky, "Photodynamic therapy–hypericin tetraether liposome conjugates and their antitumor and antiangiogenic activity," *Drug delivery*, vol. 26, no. 1, pp. 23–33, 2019.
- [67] G. Mahmoud, J. Jedelská, B. Strehlow, S. Omar, M. Schneider, and U. Bakowsky, "Photo-responsive tetraether lipids based vesicles for porphyrin mediated vascular targeting and direct phototherapy," *Colloids and surfaces b: biointerfaces*, vol. 159, pp. 720–728, 2017.
- [68] M. Luo, Y. Feng, T. Wang, and J. Guan, "Micro-/nanorobots at work in active drug delivery," *Advanced Functional Materials*, vol. 28, no. 25, p. 1706100, 2018.
- [69] W.-K. Fong, T. Hanley, and B. J. Boyd, "Stimuli responsive liquid crystals provide 'on-demand' drug delivery in vitro and in vivo," *Journal of Controlled Release*, vol. 135, no. 3, pp. 218–226, 2009.
- [70] R. Huang, R. Lan, C. Shen, Z. Zhang, Z. Wang, J. Bao, Z. Wang, L. Zhang, W. Hu, Z. Yu, *et al.*, "Remotely controlling drug release by light-responsive cholesteric liquid crystal microcapsules triggered by molecular motors," *ACS Applied Materials & Interfaces*, vol. 13, no. 49, pp. 59221–59230, 2021.
- [71] R. Negrini and R. Mezzenga, "ph-responsive lyotropic liquid crystals for controlled drug delivery," *Langmuir*, vol. 27, no. 9, pp. 5296–5303, 2011.
- [72] M. Ola, R. Bhaskar, and G. R. Patil, "Liquid crystalline drug delivery system for sustained release loaded with an antitubercular drug," *Journal of Drug Delivery and Therapeutics*, vol. 8, no. 4, pp. 93–101, 2018.
- [73] L. Zhang, J. Li, D. Tian, L. Sun, X. Wang, and M. Tian, "Theranostic combinatorial drug-loaded coated cubosomes for enhanced targeting and efficacy against cancer cells," *Cell death & disease*, vol. 11, no. 1, pp. 1–12, 2020.

- [74] J. M. Brake, M. K. Daschner, Y.-Y. Luk, and N. L. Abbott, "Biomolecular interactions at phospholipid-decorated surfaces of liquid crystals," *Science*, vol. 302, no. 5653, pp. 2094–2097, 2003.
- [75] C. S. Park, K. Iwabata, U. Sridhar, M. Tsuei, K. Singh, Y.-K. Kim, S. Thayumanavan, and N. L. Abbott, "A new strategy for reporting specific protein binding events at aqueous–liquid crystal interfaces in the presence of non-specific proteins," *ACS applied materials & interfaces*, vol. 12, no. 7, pp. 7869–7878, 2019.
- [76] L. Zhou, Q. Hu, Q. Kang, M. Fang, and L. Yu, "Construction of a liquid crystal-based sensing platform for sensitive and selective detection of l-phenylalanine based on alkaline phosphatase," *Langmuir*, vol. 35, no. 2, pp. 461–467, 2018.
- [77] S. Wang, G. Zhang, Q. Chen, J. Zhou, and Z. Wu, "Sensing of cocaine using polarized optical microscopy by exploiting the conformational changes of an aptamer at the water/liquid crystal interface," *Microchimica Acta*, vol. 186, no. 11, pp. 1–7, 2019.
- [78] P. Poulin and D. Weitz, "Inverted and multiple nematic emulsions," *Physical Review E*, vol. 57, no. 1, p. 626, 1998.
- [79] S. Prathap Chandran, F. Mondiot, O. Mondain-Monval, and J. Loudet, "Photonic control of surface anchoring on solid colloids dispersed in liquid crystals," *Langmuir*, vol. 27, no. 24, pp. 15185–15198, 2011.
- [80] H. Tang, K. Prasad, R. Sanjines, P. Schmid, and F. Levy, "Electrical and optical properties of tio<sub>2</sub> anatase thin films," *Journal of applied physics*, vol. 75, no. 4, pp. 2042–2047, 1994.
- [81] M. Murdoch, G. Waterhouse, M. Nadeem, J. Metson, M. Keane, R. Howe, J. Llorca, and H. Idriss, "The effect of gold loading and particle size on photocatalytic hydrogen production from ethanol over au/tio<sub>2</sub> nanoparticles," *Nature chemistry*, vol. 3, no. 6, pp. 489–492, 2011.
- [82] G. R. Bamwenda, S. Tsubota, T. Nakamura, and M. Haruta, "Photoassisted hydrogen production from a water-ethanol solution: a comparison of activi-

- ties of au tio<sub>2</sub> and pt tio<sub>2</sub>,” *Journal of Photochemistry and Photobiology A: Chemistry*, vol. 89, no. 2, pp. 177–189, 1995.
- [83] J. Schindelin, I. Arganda-Carreras, E. Frise, V. Kaynig, M. Longair, T. Pietzsch, S. Preibisch, C. Rueden, S. Saalfeld, B. Schmid, *et al.*, “Fiji: an open-source platform for biological-image analysis,” *Nature methods*, vol. 9, no. 7, pp. 676–682, 2012.
- [84] I. F. Sbalzarini and P. Koumoutsakos, “Feature point tracking and trajectory analysis for video imaging in cell biology,” *Journal of structural biology*, vol. 151, no. 2, pp. 182–195, 2005.
- [85] J.-Y. Tinevez, N. Perry, J. Schindelin, G. M. Hoopes, G. D. Reynolds, E. Laplantine, S. Y. Bednarek, S. L. Shorte, and K. W. Eliceiri, “Trackmate: An open and extensible platform for single-particle tracking,” *Methods*, vol. 115, pp. 80–90, 2017.
- [86] V.-P. Dinh, H. M. Le, V.-D. Nguyen, V.-A. Dao, N. Q. Hung, L. A. Tuyen, S. Lee, J. Yi, T. D. Nguyen, L. Tan, *et al.*, “Insight into the adsorption mechanisms of methylene blue and chromium (iii) from aqueous solution onto pomelo fruit peel,” *RSC advances*, vol. 9, no. 44, pp. 25847–25860, 2019.
- [87] M. Rauf, J. P. Graham, S. B. Bukallah, and M. A. Al-Saedi, “Solvatochromic behavior on the absorption and fluorescence spectra of rose bengal dye in various solvents,” *Spectrochimica Acta Part A: Molecular and Biomolecular Spectroscopy*, vol. 72, no. 1, pp. 133–137, 2009.
- [88] J.-W. Kim, H. Kim, M. Lee, and J. J. Magda, “Interfacial tension of a nematic liquid crystal/water interface with homeotropic surface alignment,” *Langmuir*, vol. 20, no. 19, pp. 8110–8113, 2004.
- [89] S. Chernyshuk and B. Lev, “Theory of elastic interaction of colloidal particles in nematic liquid crystals near one wall and in the nematic cell,” *Physical Review E*, vol. 84, no. 1, p. 011707, 2011.
- [90] E. Raynes, R. Tough, and K. Davies, “Voltage dependence of the capacitance of a twisted nematic liquid crystal layer,” *Molecular Crystals and Liquid Crystals*, vol. 56, no. 2, pp. 63–68, 1979.

- [91] Y.-K. Kim, S. V. Shiyanovskii, and O. D. Lavrentovich, “Morphogenesis of defects and tactoids during isotropic–nematic phase transition in self-assembled lyotropic chromonic liquid crystals,” *Journal of Physics: Condensed Matter*, vol. 25, no. 40, p. 404202, 2013.
- [92] B. Mustin and B. Stoeber, “Single layer deposition of polystyrene particles onto planar polydimethylsiloxane substrates,” *Langmuir*, vol. 32, no. 1, pp. 88–101, 2016.
- [93] K. Porkodi and S. D. Arokiamary, “Synthesis and spectroscopic characterization of nanostructured anatase titania: A photocatalyst,” *Materials Characterization*, vol. 58, no. 6, pp. 495–503, 2007.
- [94] D. Reyes-Coronado, G. Rodríguez-Gattorno, M. Espinosa-Pesqueira, C. Cab, R. De Coss, and G. Oskam, “Phase-pure tio<sub>2</sub> nanoparticles: anatase, brookite and rutile,” *Nanotechnology*, vol. 19, no. 14, p. 145605, 2008.
- [95] M. Riley, “Correlates of smallest sizes for microorganisms - ncbi bookshelf.”
- [96] I. F. Sbalzarini and P. Koumoutsakos, “Feature point tracking and trajectory analysis for video imaging in cell biology,” *Journal of structural biology*, vol. 151, no. 2, pp. 182–195, 2005.
- [97] P. Ruusuvaori, T. Äijö, S. Chowdhury, C. Garmendia-Torres, J. Selinummi, M. Birbaumer, A. M. Dudley, L. Pelkmans, and O. Yli-Harja, “Evaluation of methods for detection of fluorescence labeled subcellular objects in microscope images,” *BMC bioinformatics*, vol. 11, no. 1, pp. 1–17, 2010.
- [98] W. J. Godinez, M. Lampe, R. Eils, B. Müller, and K. Rohr, “Tracking multiple particles in fluorescence microscopy images via probabilistic data association,” in *2011 IEEE International Symposium on Biomedical Imaging: From Nano to Macro*, pp. 1925–1928, IEEE, 2011.
- [99] K. Celler, G. P. van Wezel, and J. Willemsse, “Single particle tracking of dynamically localizing tata complexes in streptomyces coelicolor,” *Biochemical and biophysical research communications*, vol. 438, no. 1, pp. 38–42, 2013.
- [100] N. Chenouard, I. Smal, F. De Chaumont, M. Maška, I. F. Sbalzarini, Y. Gong, J. Cardinale, C. Carthel, S. Coraluppi, M. Winter, *et al.*, “Objective comparison

- of particle tracking methods,” *Nature methods*, vol. 11, no. 3, pp. 281–289, 2014.
- [101] J. R. Howse, R. A. Jones, A. J. Ryan, T. Gough, R. Vafabakhsh, and R. Golestanian, “Self-motile colloidal particles: from directed propulsion to random walk,” *Physical review letters*, vol. 99, no. 4, p. 048102, 2007.
- [102] R. Orr and R. A. Pethrick, “Viscosity coefficients of nematic liquid crystals: I. oscillating plate viscometer measurements and rotational viscosity measurements: K15,” *Liquid Crystals*, vol. 38, no. 9, pp. 1169–1181, 2011.
- [103] T. Matsuzaki, Y. Shibata, R. Takeda, T. Ishinabe, and H. Fujikake, “Single crystalline growth of a soluble organic semiconductor in a parallel aligned liquid crystal solvent using rubbing-treated polyimide films,” *Japanese Journal of Applied Physics*, vol. 56, no. 1, p. 011601, 2016.
- [104] K. Makino and H. Ohshima, “Electrophoretic mobility of a colloidal particle with constant surface charge density,” *Langmuir*, vol. 26, no. 23, pp. 18016–18019, 2010.
- [105] H. Saboorian-Jooybari and Z. Chen, “Calculation of re-defined electrical double layer thickness in symmetrical electrolyte solutions,” *Results in Physics*, vol. 15, p. 102501, 2019.
- [106] R. Rahmani, M. Gharanfoli, M. Gholamin, M. Darroudi, J. Chamani, K. Sadri, and A. Hashemzadeh, “Plant-mediated synthesis of superparamagnetic iron oxide nanoparticles (spions) using aloe vera and flaxseed extracts and evaluation of their cellular toxicities,” *Ceramics International*, vol. 46, no. 3, pp. 3051–3058, 2020.

## APPENDIX A

### NET FORCE ACTING ON MICRODROPLETS IN LC DOMAIN, 1 MM SALT CONCENTRATION

When the aqueous phase has 1 mM NaCl salt concentration, since the electric double layer at the LC/Aqueous interface is hindered, the  $F_{EDL}$  is also decreased. Therefore, the aqueous droplets in the LC phase were located further away from LC/Aqueous interface as compared to 0.01 mM NaCl concentration case, **Figure A.1**. Please notice that the water-in-LC emulsion cannot keep droplets whose radius is less or equal to  $0.1 \mu\text{m}$  within itself since  $F_{Net} > 0$  for these droplets below the LC/Aqueous interface.

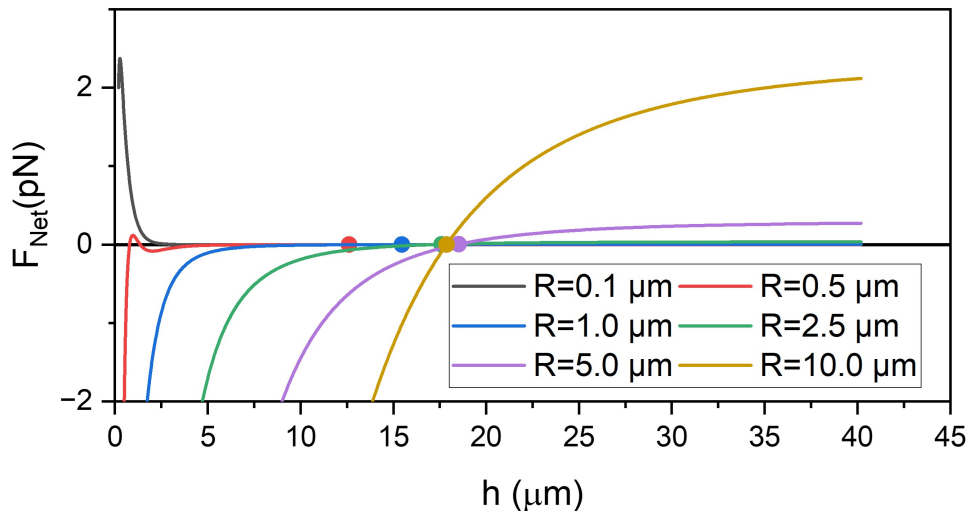


Figure A.1: Net force acting on different sizes of microdroplets at various distances. NaCl salt concentration is set to 1 mM. R represents the radius of water droplet carrying microcargo while h represent the distance to the interface.



## APPENDIX B

### CALCULATIONS FOR THE OUT OF FOCUS BEHAVIOUR OF THE JANUS PARTICLES

#### B.1 Kinetic energy calculation for out of focus behavior of Janus particles

We have used the instantaneous kinetic energies in x- and y-direction to calculate the theoretical velocity in z-direction. We assume that the particles do not lose energy at the instant as they move in the z-direction after moving in xy-plane. the kinetic energies in x- and y- directions were calculated with the instantaneous velocities retrieved from image processing data. The maximum achievable velocity in z-direction can be found as, **Equation B.1**

$$E_{kx} + E_{ky} = E_{kz} \quad (\text{B.1})$$

$E_{kx}$  and  $E_{ky}$  can be found as,

$$E_{ki} = \frac{1}{2}m_{JP}v_i \quad (\text{B.2})$$

Where  $m_{JP}$  is the mass of the Janus particle and  $v_i$  is the velocity of the x or y direction.

#### B.2 Minimum velocity to suspend a 1 $\mu\text{m}$ Janus particle in aqueous media

In order to find the minimum velocity to suspend the microparticles, we have calculated the gravitational, buoyancy and drag force, respectively. When net force balance

is zero, the particles would suspend in the aqueous media. The gravitational force,  $F_g$ , acting on the Janus particle can be calculated as **Equation B.3**,

$$F_g = \rho_{JP} \frac{4}{3} \pi R_p^3 g \quad (\text{B.3})$$

Where  $\rho_{JP}$ ,  $R_p$  and  $g$  are the density, radius of the Janus particle and gravitational acceleration, respectively. For this calculation,  $\rho_{JP}$  and  $R_p$  are taken as  $3840.5 \text{ kg/m}^3$  and  $0.5 \cdot 10^{-6} \text{ m}$ , respectively. The buoyancy force,  $F_B$ , acting on the particle can be found as, **Equation B.4**,

$$F_B = \frac{4}{3} \pi R_p^3 \rho_{water} g \quad (\text{B.4})$$

Where  $\rho_{water}$  is taken as  $997 \text{ kg/m}^3$ . Lastly, the drag force,  $F_D$  can be calculated as , **Equation B.5**,

$$F_D = 6\pi\mu_{water}Rv_D \quad (\text{B.5})$$

Where  $\mu_{water}$  is taken as  $0.8891 \cdot 10^3 \text{ Pa.s}$ . The drag velocity,  $v_D$  can be found from the following force balance shown in **Equation B.6**,

$$F_D + F_B - F_g = F_{net} = 0 \quad (\text{B.6})$$

## APPENDIX C

### ELECTROSTATIC REPULSIVE DISTANCE BETWEEN LC & AQUEOUS MEDIA

In **Figure C.1**, our calculation revealed that, when there is no salt, the particles must be over 5CB layer more than  $3.4 \mu\text{m}$  rather than interacting with. Also in **Figure C.1**, as the salt concentration reduces from near 0 to 300 mM, the levitation distance goes to a few nanometers. This also explains that when there was salt in the aqueous media, the particles could sediment naturally.

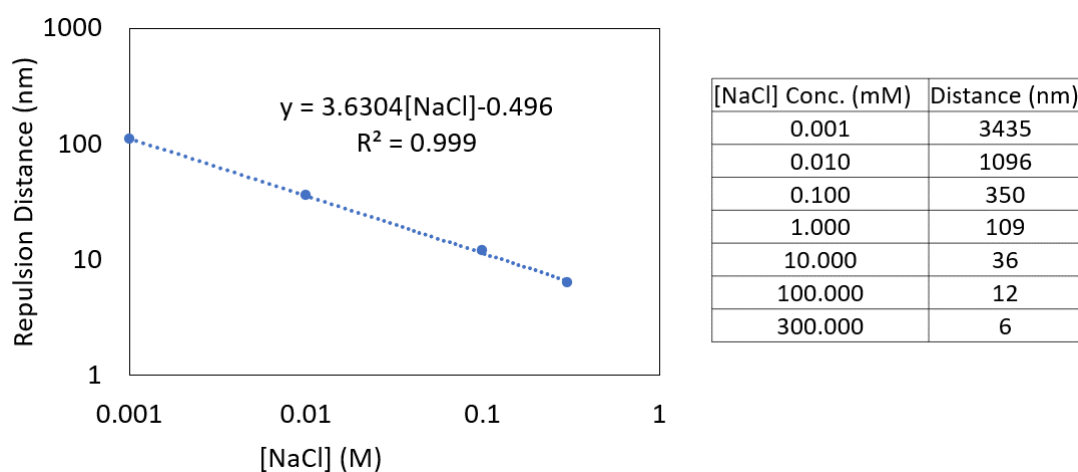


Figure C.1: Equilibrium distance between 5CB flat surface & AuCr@TiO<sub>2</sub> JPs as a function of NaCl concentration



## APPENDIX D

### REAL-TIME PARTICLE TRACKING WITH FIJI AND INTEGRATED PLUGINS FOR PARTICLE TRAJECTORY

There is no "one-fit-for-all" microparticle trajectory method since each system has different equipment and requirements for their purposes. Therefore, we also have developed our method for microparticle tracking in order to reveal the information that was sought. In our method, the samples containing the particles were constructed as closed systems. That is important since any external disturbance may lead errors in the calculation of MSD. The recording settings of the particles would be dependent on the surrounding media. When the viscosity of the media increases, one should take higher resolution recordings since the displacement of the particles decreases. The lower resolution recording may amplify the errors in the displacement data due to "pixel binning". If the higher resolution recording was not possible, to decrease the errors in the displacement, one should take longer recordings of the particles with higher frame rate. Both of the settings would end up greater file sizes which require more computational power. Therefore, one should find the optimum settings between resolution, frame rate and recording time for the MSD analysis. The recordings of the particles can be imported to the FiJi. In the FiJi, one should know the conversion factor of the pixel to system dimensions before particle analysis, e.g.  $1 \mu\text{m} = 2.35 \text{ px}$ . In the particle plugins, there are many settings for the optimisation of the particle trajectory analysis. One should check the guidelines for "MOSAIC" and "TrackMate" for detailed information [84], [85].

In the example below, a particle tracking was done of an active AuCr@TiO<sub>2</sub> Janus particle. The FPS of the recording and the resolution were set to 33.3 FPS and 1280x960 pixels. The conversion factor of this recording was  $1 \mu\text{m} = 2.35 \text{ px}$ . Firstly

the recording was imported by FiJi. It is recommended to use virtual stack to save memory. Before the tracking, the scale of the image sequence should be given to FiJi. For this sample, "distance in pixels", "known distance", "pixel aspect ratio", "unit of length" were set to 2.35, 1 , 1, and "um" (stands for  $\mu\text{m}$ ), respectively, **Figure D.1**. After giving scale, the particles should be made "bright" as the particle trajectory algorithm takes bright spots as the particle locations. Therefore, the image sequence was inverted to have bright particle spots. The black and contrast settings were adjusted with respect to the recording. As a rule of thumb, making the background as much as possible and increasing the contrast between the particle and the background is a good starting point.

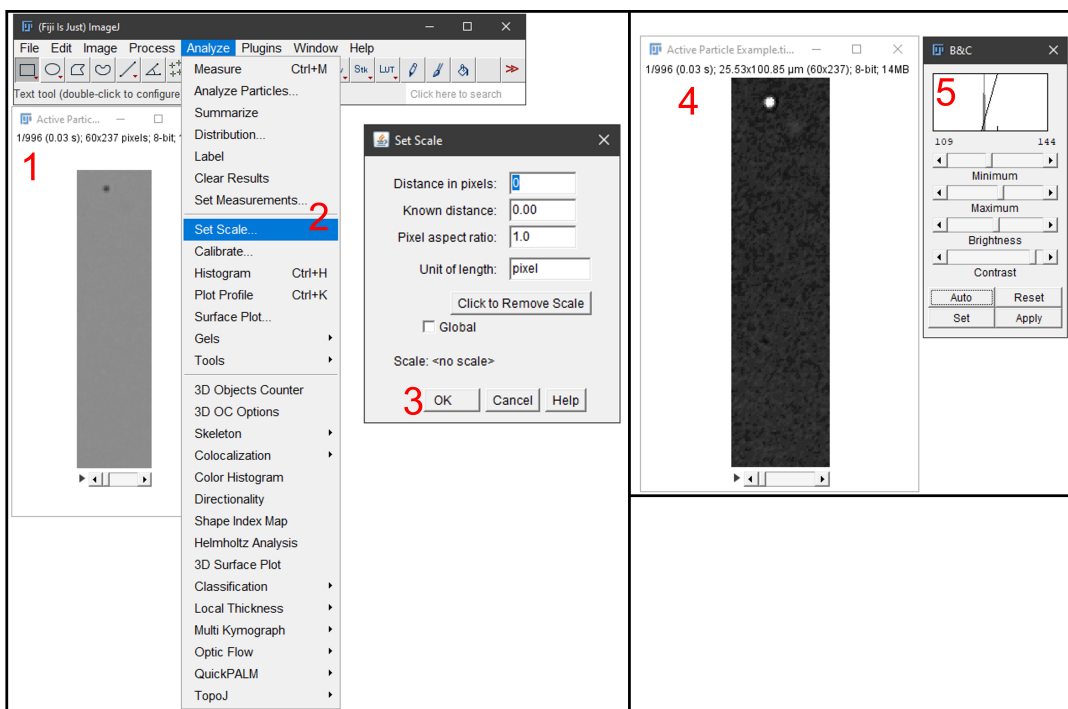


Figure D.1: FiJi program, scale settings and signal corrections

Later, the plugin called "TrackMate" was opened while the image was open as shown in **Figure D.2**. After checking the dimensions, the particle tracking algorithm could be selected.

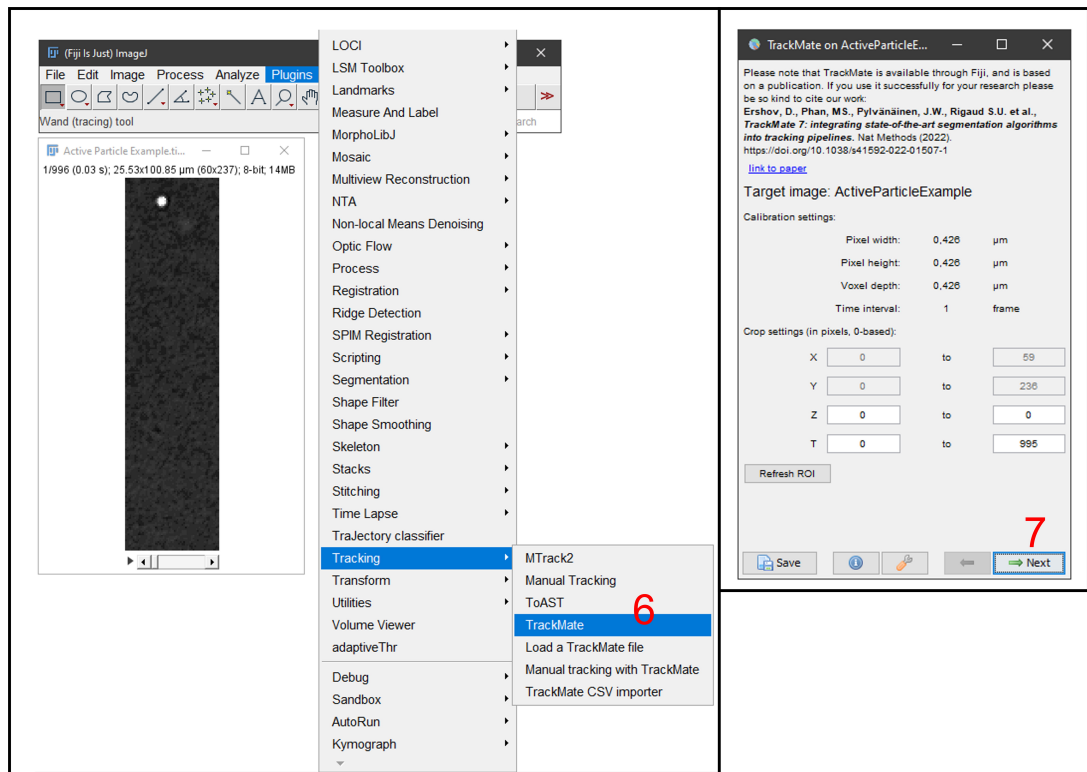


Figure D.2: FiJI TrackMate plugin

For this example "LoG" detector was selected. Later on, the estimated particle diameter was given to the detector with a quality threshold. The threshold determines the minimum level for particle identification signal value. This step is special to the recording settings of the sample, a trial and error method was performed to find the best fitting diameter. The set diameter for the image sequence could be previewed with "Preview" button. For this example, the settings for the LoG detector were "3"  $\mu\text{m}$  estimated object diameter and "10" quality threshold, respectively. After the calculation the number of spots in the image sequence could be attained, **Figure D.3**.

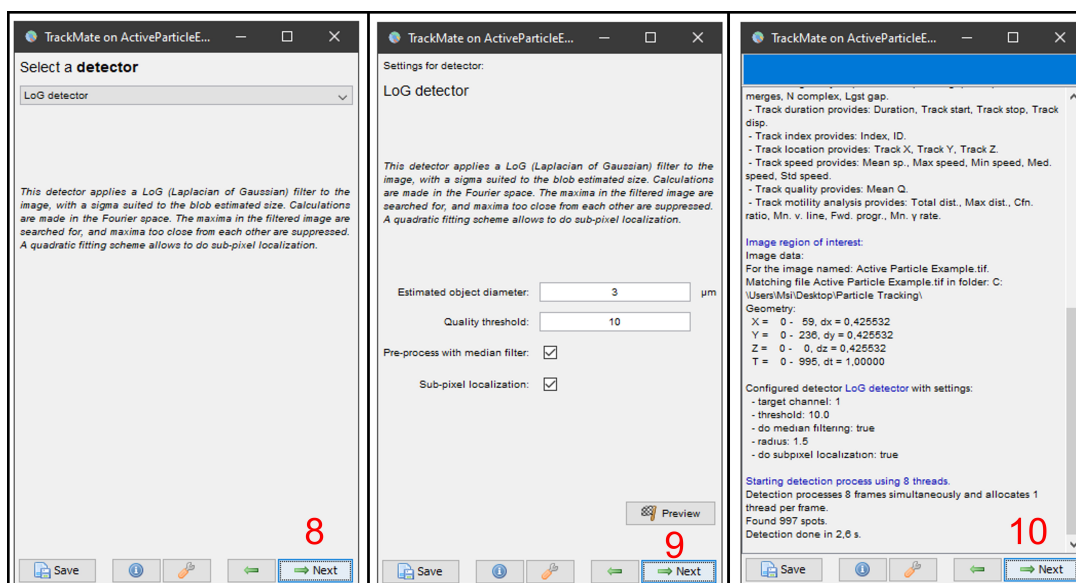


Figure D.3: TrackMate spot finding

After spot finding, filtering could be done to the spots. From **Figure D.4** initially the algorithm had found 997 spots for the image sequence. However, the sequence should have 996 spots since the image sequence has one spot (particle) in each frame. Therefore, necessary filtering was done before continue. Then, the tracker was set for the image sequence. for this example "simple LAP tracker" was selected, **Figure D.4**.

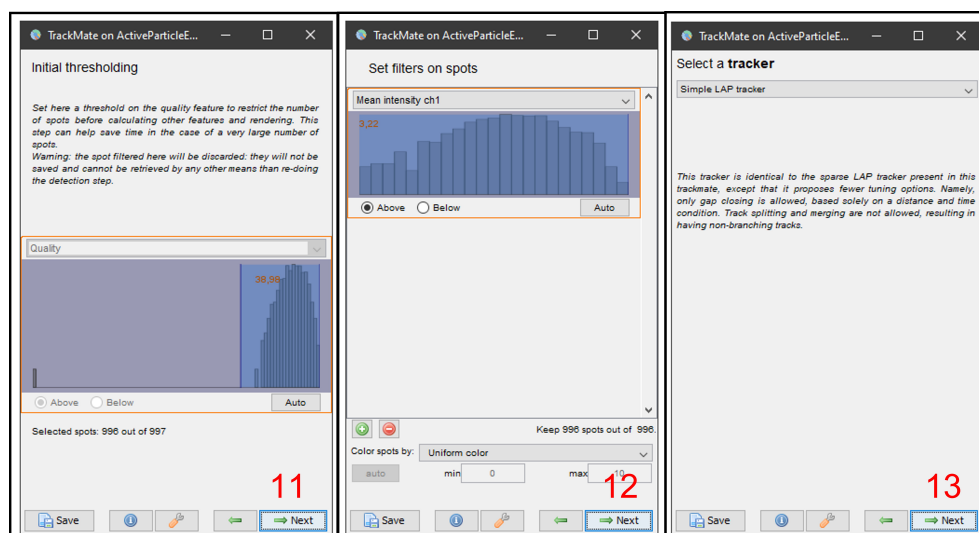


Figure D.4: Initial thresholding and spot filtering.

The maximum linking distance between two images, the gap-closing maximum distance for the "poorly observed" particles and the gap-closing maximum distance for the particles reappearing in the image sequence were set. For this example, the settings were 10.0  $\mu\text{m}$ , 10.0  $\mu\text{m}$  and 20 frames, respectively, **Figure D.5**. The number of tracks could be attained after this step. For this example since the image sequence had one particle trajectory, the tracker have found only one trajectory in the sequence.

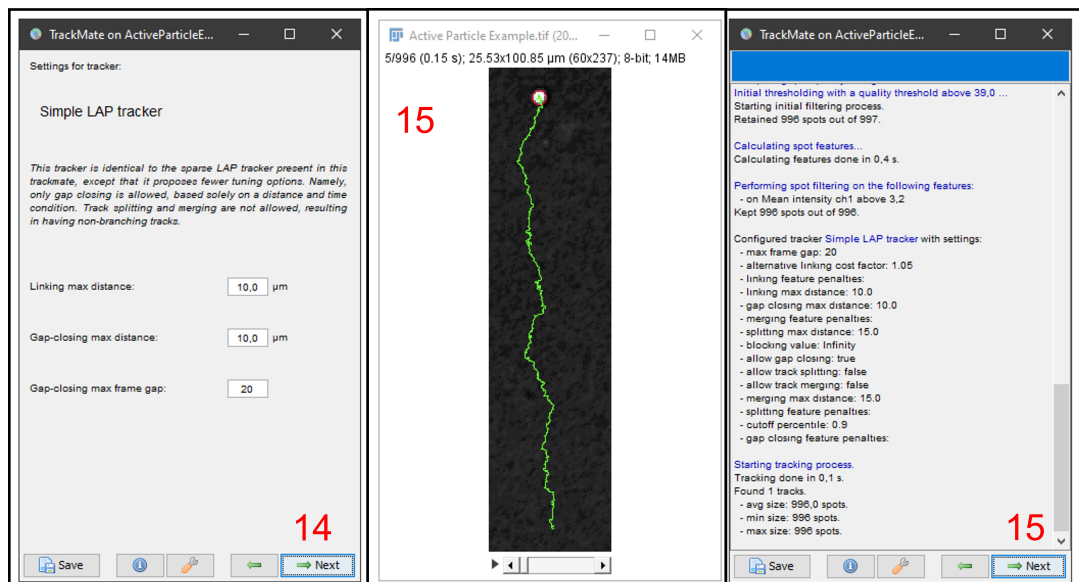


Figure D.5: TrackMate trajectory builder

After this step there would be an extra step when the image sequence resulted in multiple trajectories. Depending on the record, filter the trajectories until only one trajectory remains. Then, trim the trajectory data at the end of the analysis, **Figure D.6**. After trimming of the data, go to settings with wrench icon and get the position data of the particle from "spots" menu.

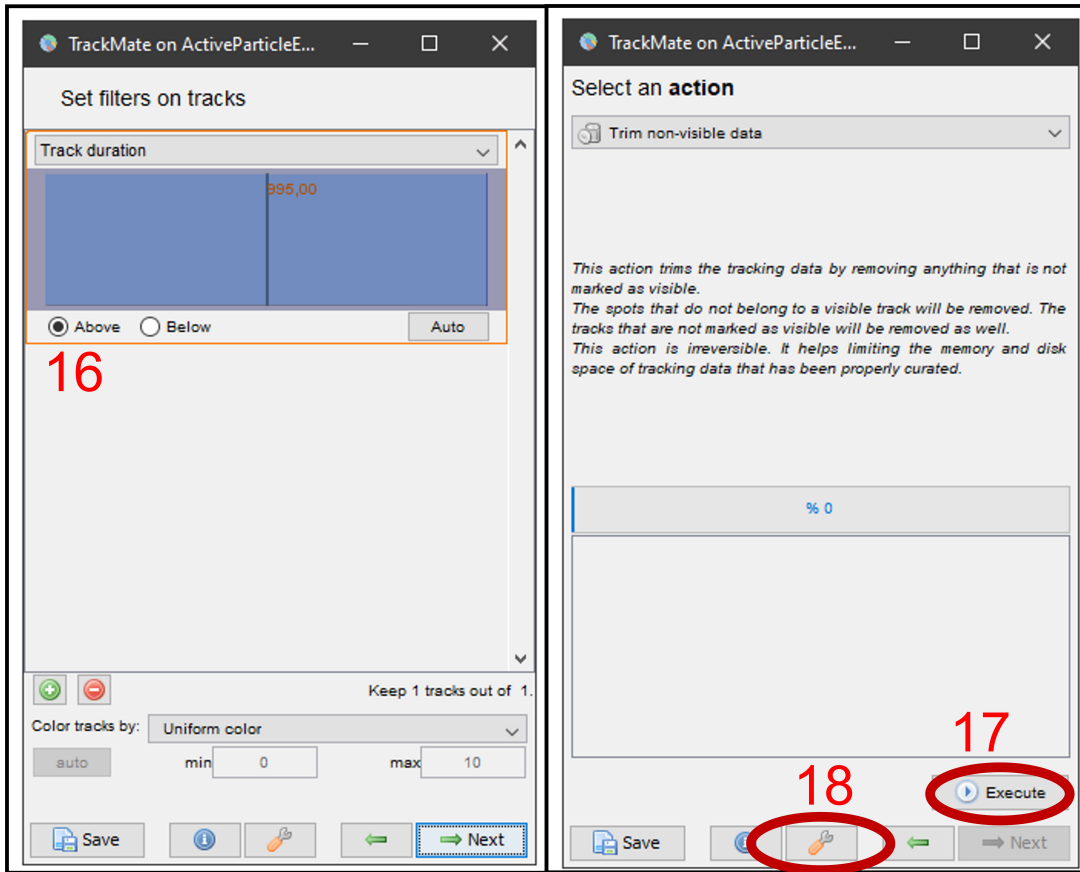


Figure D.6: TrackMate trajectory filtering and data trimming

Lastly, export the data to a .csv file to save the position data of the trajectory as shown in **Figure D.7**. Please notice there are additional columns in the .csv file other than position data with respect to frame number.

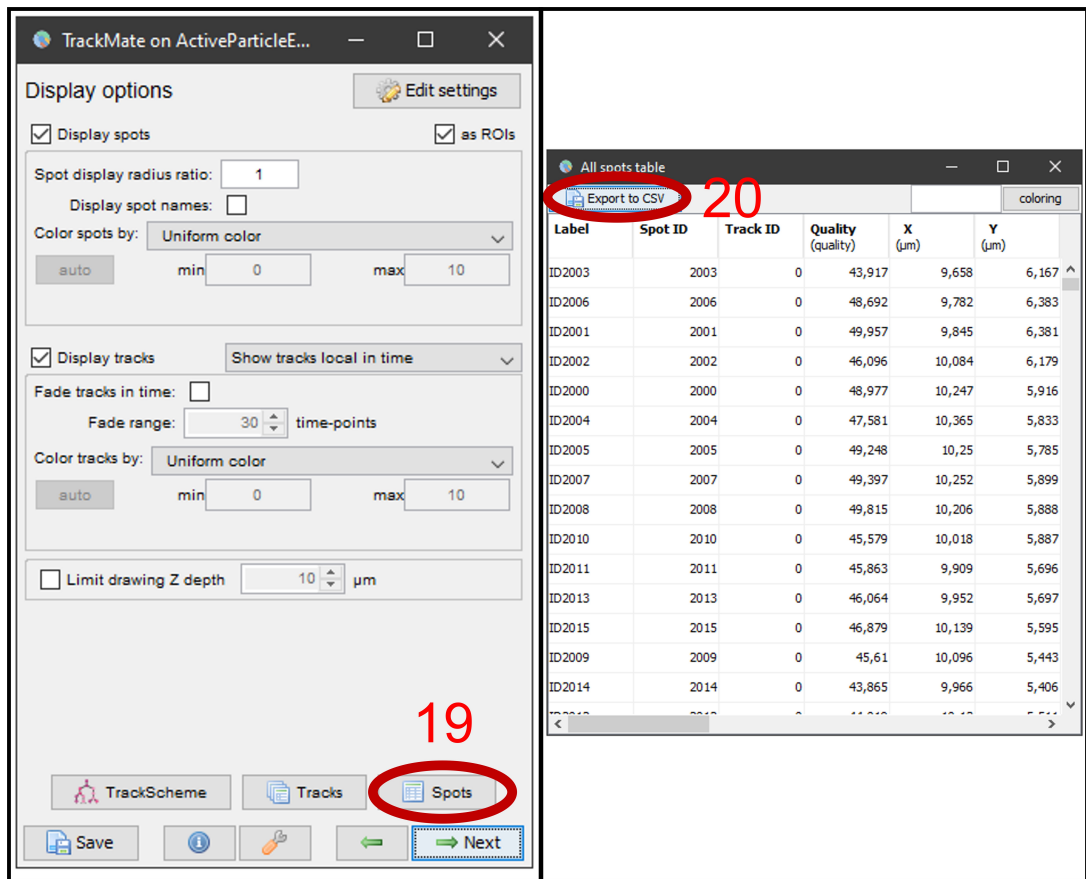


Figure D.7: TrackMate trajectory spot data save



## APPENDIX E

### MATLAB CODES FOR MSD ANALYSES

The following custom MATLAB codes were generated to analyse the MSD of the microparticles while using the position data. The position data was given to the MATLAB code in spreadsheet format such as Microsoft Excel .xlsx or .csv. The following codes for designed to use in "TrackMate" plugin in Fiji. Please be careful before use since the syntax of the codes may be altered due to printing purposes of this thesis.

The passive microparticle MSD analysis MATLAB code is given below:

```
clear all
clc

M = readmatrix( YourFileName.csv );  This MATLAB code was generated to use
                                     "Trackmate". Please check the Fiji
                                     plugin before use.
M(:, [1,2,3,4,7,8,10,11,12,13,14,15,16,17,18,19,20])= []
data = M;
Inputs for the calculator are:
    x position, y position, frame number
    x represents position x, y represents position y, t represents the time
    in terms of frame    (unit is 1/fps)
x = data(:,1);
y = data(:,2);
t = data(:,3);
n = length(x);    of data points in the dataset

T = 25;    it is the end point where MSD calculations will be held,
           number of delta t points
fps = 29.0 ;  Frame rate of the corresponding particle
```

```

if T == 0    Let T value be as minimum as possible
    T = n 1 ;
end

l = T ;    L , the dimension value to generate the matrixes for the calculations

msdx  = zeros(1,l);    In this stage, we generate the zero matrixes of 1xL
                        dimension for:
msdy  = zeros(1,l);    mean squared displacement
                        of x and y and standart deviation of x and y

msd   = zeros(1,l);
stdx  = zeros(1,l);    delta t values as "tau"
stdy  = zeros(1,l);
tau   = zeros(1,l);
disx  = zeros(1,l);
disy  = zeros(1,l);
dis   = zeros(1,l);

MSD   Displacement Calculations
for i = 1:l:l    Regular counter operation from "one" to "L" increments of "one"
    count      = 0;
    j          = 1;
    tau(i)     = i;
    while j+i = n
        while j + i = n    t(j + i) - t(j)    1.1    tau(i)
                            for the data points the allowed "gap"
                            is set to 1 frame.
                            Therefore "1.1" constant is used for tau.
            j = j + 1;
        end
        if j + i = n
            msdx(i)      = msdx(i) + (x(j) - x(j + i)) 2;

                                At this step the code basically
                                sums the squared displacements.

            msdy(i)      = msdy(i) + (y(j) - y(j + i)) 2;
            msd(i)       = msd(i) + (x(j) - x(j + i)) 2 + (y(j) - y(j + i)) 2;
            disx(i)      = disx(i) + abs(x(j) - x(j+i));
            disy(i)      = disy(i) + abs(y(j) - y(j+i));
            dis(i)       = sqrt(disx(i) 2 + disy(i) 2);
            count        = count + 1;
        end
    end
end

```

```

        j      = j + i;
    end
end
if count ~= 0
    msdx(i) = msdx(i)/count;           At this step, the code finds
                                       the mean
                                       of the squared displacements.

    msdy(i) = msdy(i)/count;
    msd(i) = msd(i)/count;
    disx(i) = disx(i);
    disy(i) = disy(i);
    dis(i) = dis(i);

end

end

Standart Deviation calculations for MSD
for i = 1:1:l      Regular counter operation from "one" to "L"
                  increments of "one"

    count = 0;
    j      = 1;
    tau(i) = i;
    while j+i = n
        while j + i = n      t(j + i) - t(j)  1.1  tau(i)
                               for the data points the
                               allowed "gap" is set to
                               1 frame.

            j = j + 1;       Therefore "1.1" constant is
                               used for tau.

        end
        if j + i = n
            stdx(i) = stdx(i) + ((x(j) - x(j + i))^2 / msdx(i))^2;
            stdy(i) = stdy(i) + ((y(j) - y(j + i))^2 / msdy(i))^2;
            count = count + 1;
            j      = j + i;
        end
    end
end
if count ~= 0
    stdx(i) = sqrt(stdx(i)/(count - 1));
    stdy(i) = sqrt(stdy(i)/(count - 1));
end
end

```

```

end

time = tau/fps;
msdx = msdx(1);
msdy = msdy(1);
smsdx = sum(tau(:).msdx(:))/sum(tau(:).tau(:));
smsdy = sum(tau(:).msdy(:))/sum(tau(:).tau(:));
stdx = stdx(1);
stdy = stdy(1);
Vel = fps dis(1)/n;
Velx = fps disx(1)/n;
Vely = fps disy(1)/n;
distx = disx(1) ;
disty = disy(1) ;

tmsd = transpose(msd);
tmsdx = transpose(msdx);
tmsdy = transpose(msdy);
ttime= transpose(time);

[FOx] = fit(ttime, tmsdx, 2 D x , StartPoint , [0], Robust , Bisquare );
valuesx = coeffvalues(FOx);
Dx = valuesx(1);
Vx = valuesx(2);
Vx = 0;

[FOy] = fit(ttime, tmsdy, 2 D x , StartPoint , [0], Robust , Bisquare );
valuesy = coeffvalues(FOy);
Dy = valuesy(1);
Vy = valuesy(2);
Vy = 0;

[FO,gof] = fit(ttime, tmsd, 4 D x , StartPoint , [0], Robust , Bisquare );
values = coeffvalues(FO);
D = values(1);
V = values(2);
V = 0;
GoF = struct2cell(gof);

```

```

figure
plot(ttime, tmsdx, ob, ttime, tmsdy, og);
legend();
hold on
plot(FO, k, ttime, tmsd, or);
xlabel( tau(s) );
xlim([0 T/fps]);
ylabel( Mean Squared Displacement ( $\mu\text{m}^2$ ) );
hold on
plot(FO, k, predobs);
legend( MSDx, MSDy, MSD, Curve Fit for MSD );

Results = [Vel, Velx, Vely, distx, disty, D, V, Dx, Vx, Dy, Vy, GoF(2)]

figure;

plot(time, disx, .b, time, disy, .g, time, dis, .r);
xlabel( tau(s) );
ylabel( Velocity ( $\mu\text{m/s}$ ) );
legend( velx, vely, vel );

```

**The active microparticle MSD analysis MATLAB code is given below:**

```

clear all
clc

Inputs for the calculator are:
x position, y position, frame number
x represents position x, y represents position y, t represents the time
in terms of frame (unit is 1/fps)
M = readmatrix( YourFileName.csv );
M(:, [1,2,3,4,7,8,10,11,12,13,14,15,16,17,18,19,20])= []
data = M;
x = data(:,1);
y = data(:,2);
t = data(:,3);
n = length(x);      of data points in the dataset

```

```

T = 25;    it is the end point where MSD calculations will be held, number of
           delta t points
fps = 50.0 ;    Frame rate of the corresponding particle
if T == 0    Let T value be as minimum as possible
    T = n 1 ;
end

l = T ;    L , the dimension value to generate the matrixes for the calculations

msdx  = zeros(1,l);    In this stage, we generate the zero matrixes of 1xL
                       dimension for:
msdy  = zeros(1,l);    mean squared displacement of x and y and standart
                       deviation of x and y
msd   = zeros(1,l);
stdx  = zeros(1,l);    delta t values as "tau"
stdy  = zeros(1,l);
tau   = zeros(1,l);
disx  = zeros(1,l);
disy  = zeros(1,l);
dis   = zeros(1,l);

MSD    Displacement Calculations
for i = 1:1:l    Regular counter operation from "one" to "L" increments of "one"
    count    = 0;
    j        = 1;
    tau(i)   = i;
    while j+i = n
        while j + i = n    t(j + i)    t(j)    1.1    tau(i)
                           for the data points the allowed "gap"
                           is set to 1 frame.
            j = j + 1;    Therefore "1.1" constant is used for tau.
        end
    if j + i = n
        msdx(i)    = msdx(i) + (x(j)    x(j + i)) 2;
                       At this step the code basically
                       sums the squared displacements.
        msdy(i)    = msdy(i) + (y(j)    y(j + i)) 2;
        msd(i)     = msd(i) + (x(j)    x(j + i)) 2 + (y(j)    y(j + i)) 2;
        disx(i)    = disx(i) + abs(x(j)    x(j+i));
        disy(i)    = disy(i) + abs(y(j)    y(j+i));
    end
end

```

```

        dis(i)      = sqrt(disx(i) 2 + disy(i) 2);
        count      = count + 1;
        j          = j + i;
    end
end
if count ~= 0
    msdx(i) = msdx(i)/count;    At this step, the code finds
                                the mean
                                of the squared displacements.

    msdy(i) = msdy(i)/count;
    msd(i)  = msd(i)/count;
    disx(i) = disx(i);
    disy(i) = disy(i);
    dis(i)  = dis(i);

end
end
Standart Deviation calculations for MSD
for i = 1:1:l    Regular counter operation from "one" to "L"
                increments of "one"

    count = 0;
    j      = 1;
    tau(i) = i;
    while j+i = n
        while j + i = n    t(j + i)    t(j)    1.1    tau(i)
                            for the data points the
                            allowed "gap" is set to
                            1 frame.

                            j = j + 1;    Therefore "1.1" constant is
                            used for tau.

        end
        if j + i = n
            stdx(i) = stdx(i) + ((x(j)    x(j + i)) 2    msdx(i)) 2;
            stdy(i) = stdy(i) + ((y(j)    y(j + i)) 2    msdy(i)) 2;
            count   = count + 1;
            j       = j + i;
        end
    end
end
if count ~= 0
    stdx(i) = sqrt(stdx(i)/(count    1));

```

```

        stdy(i) = sqrt(stdy(i)/(count - 1));
    end
end

time = tau/fps;
msdx = msdx(1);
msdy = msdy(1);
smsdx = sum(tau(:).msdx(:))/sum(tau(:).tau(:));
smsdy = sum(tau(:).msdy(:))/sum(tau(:).tau(:));
stdx = stdx(1);
stdy = stdy(1);
Vel = fps dis(1)/n;
Velx = fps disx(1)/n;
Vely = fps disy(1)/n;
distx = disx(1) ;
disty = disy(1) ;

tmsd = transpose(msd);
tmsdx = transpose(msdx);
tmsdy = transpose(msdy);
ttime= transpose(time);

[FOx] = fit(ttime, tmsdx, 2 D x+V 2 x 2 , StartPoint,...
           [0.0001,1], Lower, [0,0], Robust , Bisquare );
valuesx = coeffvalues(FOx);
Dx = valuesx(1);
Vx = valuesx(2);
Vx = 0;

[FOy] = fit(ttime, tmsdy, 2 D x+V 2 x 2 , StartPoint,...
           [0.0001,1], Lower, [0,0], Robust , Bisquare );
valuesy = coeffvalues(FOy);
Dy = valuesy(1);
Vy = valuesy(2);
Vy = 0;

[FO,gof] = fit(ttime, tmsd, 4 D x+V 2 x 2 , StartPoint,...
              [0.0001,1], Lower, [0,0], Robust , Bisquare );

values = coeffvalues(FO);

```

```

D = values(1);
V = values(2);
V = 0;
GoF = struct2cell(gof);

figure
plot(ttime, tmsdx, ob, ttime, tmsdy, og);

legend();
hold on
plot(FO, k, ttime, tmsd, or);
xlabel( tau(s) );
xlim([0 T/fps]);
ylabel( Mean Squared Displacement ( $\mu\text{m}^2$ ) );
hold on
plot(FO, k, predobs);
legend( MSDx, MSDy, MSD, Curve Fit for MSD );

Results = [Vel, Velx, Vely, distx, disty, D, V, Dx, Vx, Dy, Vy, GoF(2)]

figure;

plot(time, disx, .b, time, disy, .g, time, dis, .r);
xlabel( tau(s) );
ylabel( Velocity ( $\mu\text{m/s}$ ) );
legend( velx, vely, vel );

```